UNCLASSIFIED
SECURITY CLASSIFICATION OF THIS PAGE

(4)

## DOCUMENTATION PAGE

Form Approved
OMB No. 0704-0188

# AD-A203 365

1b. RESTRICTIVE MARKINGS DTIC FILE COPY

3. DISTRIBUTION/AVAILABILITY OF REPORT
Approved for public release;
distribution unlimited

4. PERFORMING ORGANIZATION REPORT NUMBER(S)

5. MONITORING ORGANIZATION REPORT NUMBER(S)
Department of the Navy
Naval Electronic Systems Command

6a. NAME OF PERFORMING ORGANIZATION
Research Laboratory of Electronics
Massachusetts Institute of Technology

6b. OFFICE SYMBOL (If applicable)

7a. NAME OF MONITORING ORGANIZATION
Washington, DC 20363

6c. ADDRESS (City, State, and ZIP Code)
77 Massachusetts Avenue
Cambridge, MA 02139

7b. ADDRESS (City, State, and ZIP Code)

8a. NAME OF FUNDING/SPONSORING ORGANIZATION
Advanced Res. Projects Agency

8b. OFFICE SYMBOL (If applicable)

9. PROCUREMENT INSTRUMENT IDENTIFICATION NUMBER
MDA 903-85-C-0215

8c. ADDRESS (City, State, and ZIP Code)

10. SOURCE OF FUNDING NUMBERS

| PROGRAM ELEMENT NO. | PROJECT NO. | TASK NO. | WORK UNIT ACCESSION NO. |
|---|---|---|---|
| | 1001/1053 | | |

11. TITLE (Include Security Classification)
Focused Ion Beam Fabrication of Graded Channel FET's in GaAs and Si.

12. PERSONAL AUTHOR(S)
J. Melngailis

| 13a. TYPE OF REPORT | 13b. TIME COVERED | 14. DATE OF REPORT (Year, Month, Day) | 15. PAGE COUNT |
|---|---|---|---|
| Final Report | FROM 7/1/85 TO 9/30/88 | November 21, 1988 | 38 pp. plus append |

16. SUPPLEMENTARY NOTATION

| 17. COSATI CODES | | | 18. SUBJECT TERMS (Continue on reverse if necessary and identify by block number) |
|---|---|---|---|
| FIELD | GROUP | SUB-GROUP | |
| | | | |
| | | | |

19. ABSTRACT (Continue on reverse if necessary and identify by block number)

Work by J. Melngailis and his collaborators is summarized here.

DTIC
ELECTE
JAN 3 1989
S D
H

20. DISTRIBUTION/AVAILABILITY OF ABSTRACT
☒ UNCLASSIFIED/UNLIMITED ☐ SAME AS RPT. ☐ DTIC USERS

21. ABSTRACT SECURITY CLASSIFICATION
UNCLASSIFIED

| 22a. NAME OF RESPONSIBLE INDIVIDUAL | 22b. TELEPHONE (Include Area Code) | 22c. OFFICE SYMBOL |
|---|---|---|
| Barbara Passero RLE Contract Reports | (617) 253-2566 | |

DD Form 1473, JUN 86 Previous editions are obsolete.

SECURITY CLASSIFICATION OF THIS PAGE
UNCLASSIFIED

November 21, 1988

# "Focused Ion Beam Fabrication of Graded Channel FET's in GaAs and Si"

Final Report

1 July 1985 to 30 Sept. 1988

by John Melngailis

DARPA DOD Contract

MDA 903-85-C-0215

89 1 03 141

Table of Contents




...odes
.../or
Dist | Special
A-1

# Focused Ion Beam Fabrication of Graded Channel Field Effect Transistors in GaAs and Si

## A. Abstract

The aim of our focused ion beam research program at M.I.T. is to exploit the unique capabilities of this novel technology in fabricating devices which have a lateral gradient of doping. (This program of research will be continued so that this final report will not be exhaustive.) Using internal institute funds, M.I.T. purchased a focused ion beam system capable of producing beams of the common dopants of Si and GaAs (i.e., B, As, Si and Be) at energies up to 300 keV. In order to carry out the proposed implantations the system needed to be upgraded in several ways. Pattern writing software was developed, as well as software for translating patterns written in MAGIC, a layout system in use at M.I.T., into the FIB format. To achieve the minimum beam diameter the ion column had to be realigned mechanically and electrical noise needed to be reduced in the circuits which deflect the beam. With the upgraded system we have written patterns in PMMA with 50 nm line width, and achieved metal lift-off of 50 nm width lines.

Implants have been carried out in GaAs MESFET's where a gradient of doping was produced in the channel region under the gate. The electrical characteristics of the MESFET's were asymmetrical when source and drain were reversed. The lateral gradient in GaAs was exploited to produce a novel device, a tunable Gunn diode. This diode could be tuned to oscillate at frequencies between 6 and 23 GHz. B and As have been implanted into Si with a focused ion beam and depth profile of the dopant ions was measured with SIMs. Evidence of channelling was observed. Computer models for the distribution of dopants in Si have been produced. In addition, the behavior of the Gunn diodes and Si MOSFETs has been simulated on the computer.

B. Introduction

Although the possibility of focusing beams of ions for microfabrication was recognized and demonstrated in the early 1970's[1], the invention of the liquid metal ion source[2] in 1978 made this new technique practical. The high brightness of this source resulted in a current density in the focal spot at the sample near $1 A/cm^2$ [3] which was a $10^4$ to $10^5$ fold increase over conventional ion sources.

The first sources of ions emitted only Ga, and the Ga source still plays a key technological role. For example, photomask repair by focused ion beams has become a successful commercial technique. Unwanted chrome is milled off, and missing chrome is added by ion induced deposition from a local gas ambient of, for example, chrome carbonyl gas. In addition, this dual deposition/removal mode of operation can also be exploited for integrated circuit restructuring or repair, and will be essential for x-ray lithography mask repair.

However, for implantation into semiconductors other species, such as B and As for Si substrates, and Si and Be for GaAs substrates, are needed. For this, alloy sources[4][5] have been developed and ion columns with mass separation capability have been built.[5] There are close to 35 such machines, capable of direct implantation, in research laboratories world wide, about 80% of them in Japan.

Table I summarizes the two types of machines, their typical ranges of operation, and the typical applications.

Table I. Focused ion beam systems of two types, with typical specifications and main uses

| | without mass separation | with mass separation |
|---|---|---|
| Accelerating voltages | 5 - 70kV | 5 - 200 kv |
| Current density | 1 - 10A/cm$^2$ | 0.1 - 1A/cm$^2$ |
| Min. beam diameter | 0.04$\mu$m | 0.05 $\mu$m |
| Ion species available | Ga, In, Au (elemental sources) | Au/Si/Be Pd/B/As/P (alloy sources) |
| Main uses | - micromachining<br>- ion induced deposition and etching<br>- high resolution SIMS<br>- scanning ion microscopy<br>- mask repair<br>- circuit repair | - implantation<br>- lithography |

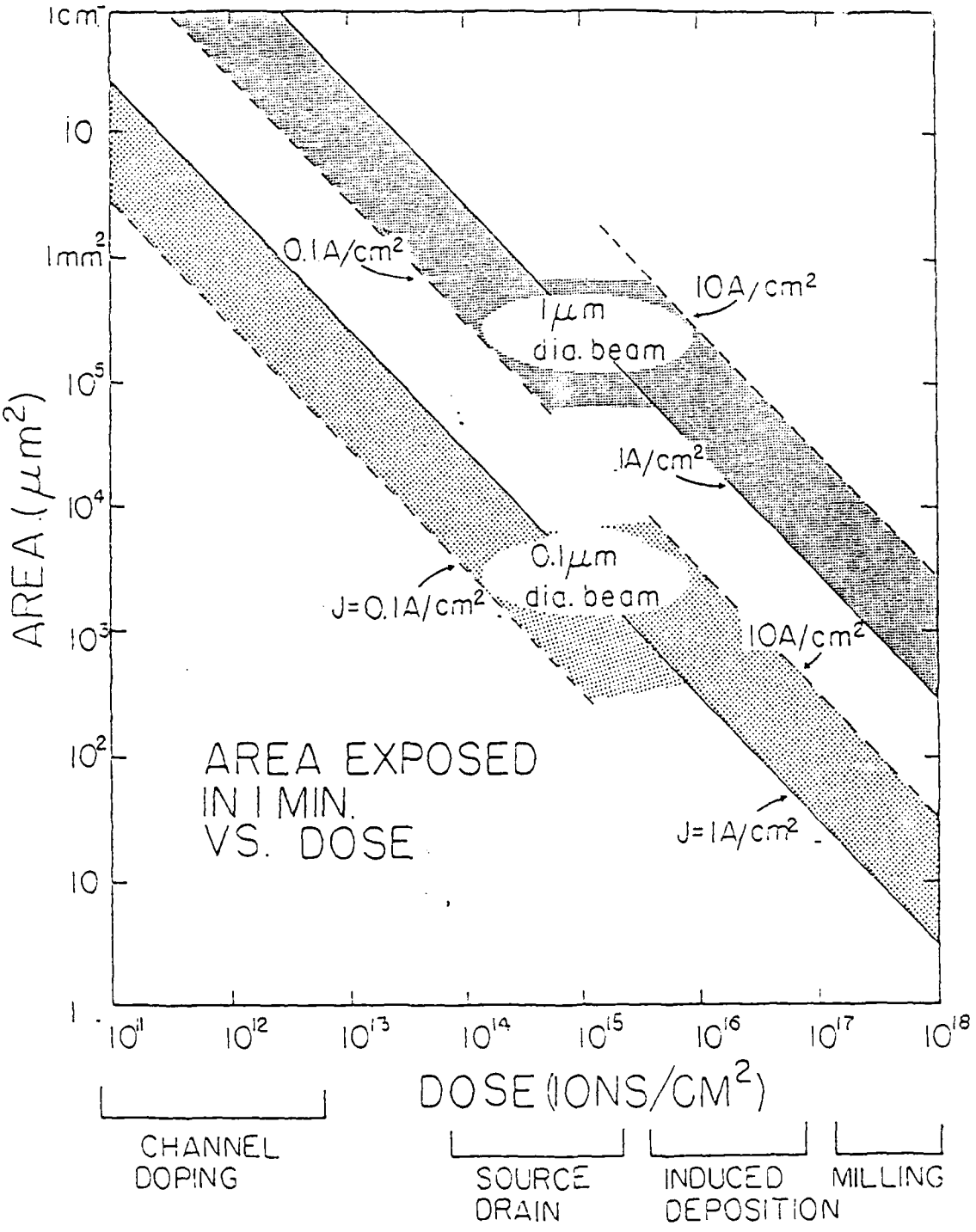


Fig. 1 A guide to the sample area which can be addressed in one minute in a given focused ion beam application. The plots are for three current densities and two beam diameters. Most of the sources usable for implantation achieve current densities near 0.1 A/cm$^2$ on the sample, while the systems usable for milling have elemental ion sources with current densities of 4 A/cm$^2$ reported and 10 A/cm$^2$ projected.

Since this report is concerned with focused ion beam implantation, we will discuss that in more detail. Ion implantation is almost universally used to fabricate semiconductor devices both in Si and GaAs. Patterned doping is achieved by covering part of the surface with resist or some other film and implanting the bare area. Thus each implantation requires resist to be spun, exposed to radiation through a mask, developed, and finally implanted. The entire wafer is given the same dose. The novel feature for focused ion beams is that the implantation can be carried out in a fine pattern, below 0.1 $\mu$m resolution, without the use of mask and resist. This leads to simplification of the process, but most importantly, adds new flexibility in two ways:

1. The dose can be varied as a function of position within a given device, such as a transistor and

2. The dose can be varied from device to device for producing special circuits[6] or for optimizing the dose level during prototyping.

The disadvantages of focused ion beams is that the implantation is serial, point-by-point, (this is also the basis of the advantages) and, therefore, slow. Fig. 1 shows the area which can be implanted in one minute vs. dose for two beam diameters. Clearly if high resolution is not needed (e.g. if we only want to vary the dose from device to device), then the beam diameter can be increased, and the area which can be implanted can be increased. To lowest order the current density stays constant, as the diameter is increased. Thus as seen in the figure channel implants with larger beams are feasible over entire chips and perhaps over entire wafers. In many cases, for example in

CMOS devices, the area of the channel implants is less than about 5% of the entire chip area. Thus a 4" wafer may have only 3 $cm^2$ of total channel area to implant. In GaAs chips such as MMIC's the area occupied by active transistors is often much smaller still, so that implantation with a focused ion beam is expected to be a labor-saving and yield-increasing step.

This report, however, is concerned with the first of the two modes of operation, namely, implantation of doping gradients, i.e. novel structures which cannot be built by conventional means.

A more complete review of the focused ion beam field was written by the author last year[7] and is included as Appendix I.

C. Results

Our work during the duration of this contract has concentrated in four areas: machine development, implantation into Si, implantation and novel devices in GaAs, and modeling. In many cases the tasks were linked, for example, the machine operation had to be improved to perform a specific implant, or modeling helped to understand the operation of the devices fabricated. We will nevertheless discuss each area in turn.

## 1. Machine Development

### a) History

At the time this contract was started, we had a purchase order in effect for a complete focused ion beam implantation/lithography system to be built by IBT of Beverly, MA. The machine, called "The Microfocus", was based on an ion column design generated at Hughes Research Laboratories and was the only machine of that type offered for sale in the U.S.A. At that time, it had demonstrated rudimentary, and for some of our experiments already usable operation. A beam diameter of about 0.3 $\mu$m could be produced at energies above 100 keV. Imaging, scanning, and manual pattern generation were available. At this point the company decided to develop a focused ion beam for mask repair on a high priority basis, and to devote only a limited number workers to our machine. By the end of 1986 it became clear that the capital resources to complete our machine were exhausted so that IBT and M.I.T. negotiated to take the Microfocus as is, at a reduced price, and to devote the remaining money, which had been set aside for the purchase of the machine, for its development.

Thus the Microfocus was moved to M.I.T. in March, 1987 and was up and successfully operating by June, 1987. Our own development was aimed at fine tuning the operation of the column, developing software and procedures for alignment and for beam deflection calibration, and developing software for pattern generating and pattern translation. Much of this work was funded by the M.I.T. machine-purchase budget.

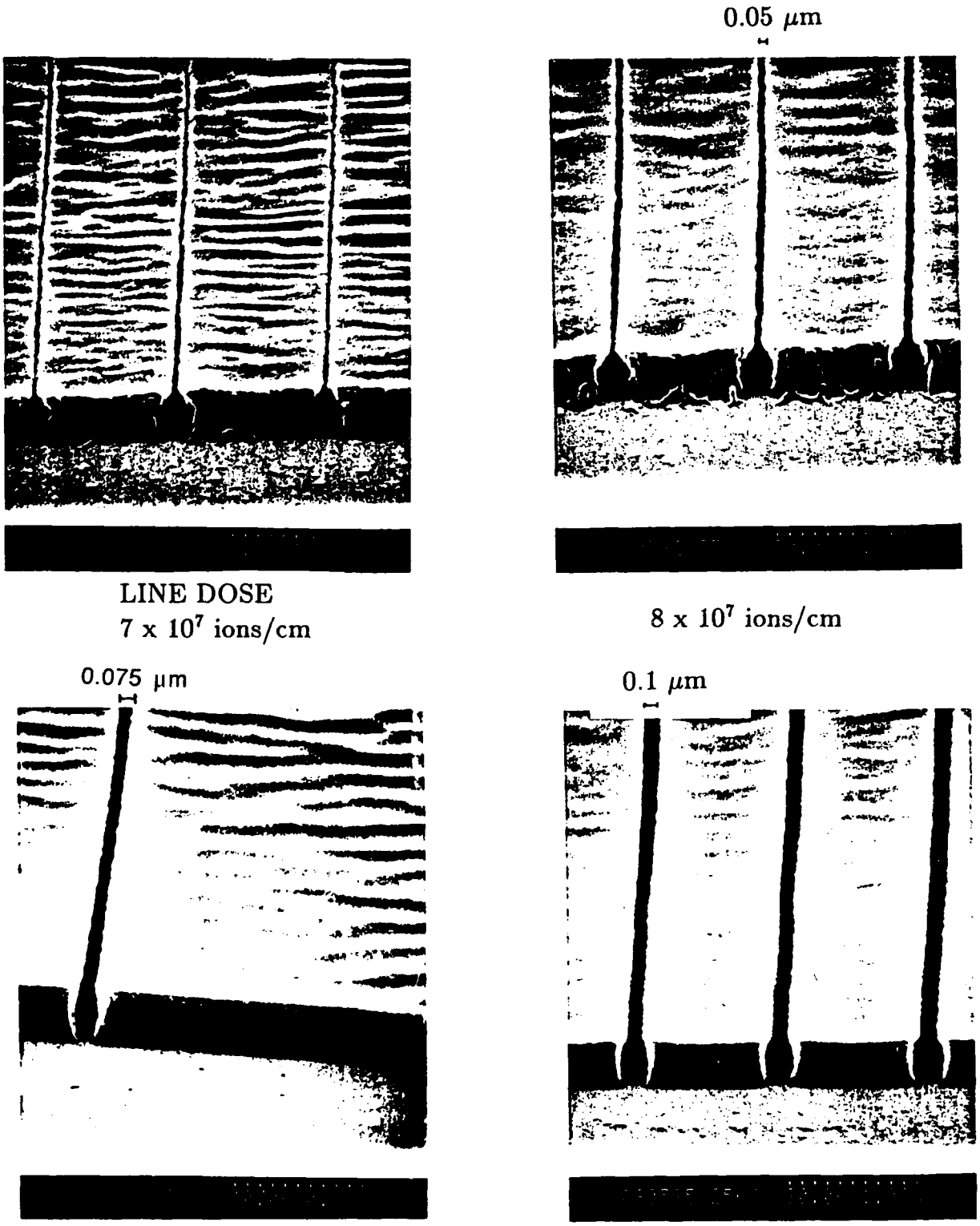


Fig. 2 Focused ion beam exposure of PMMA 0.3 μm thick. 200 keV $Be^{++}$ ions are used. The line width is shown for 4 different line doses. Above 0.05 μm line width, continuous features can be written. A pad, in foreground of all photos, is also exposed to get a better perspective view. The wrinkling of the PMMA (waviness in the flat areas) is due to the electron beam exposure in the scanning electron microscope.


Fig. 3 A pair of gold lines plated up in focused ion beam exposed PMMA. The lines are 0.06 $\mu$m wide and 0.2 $\mu$m high with a 0.06 $\mu$m clear space between them. They were fabricated by exposing PMMA 0.3 $\mu$m thick (as in Fig. 2) which was spun on a thin gold plating base, developing, plating up the gold and then dissolving the PMMA. This is probably the best measure of the quality of the PMMA sidewalls.

Some of the tasks were intimately linked to the implantation work being performed under this contract.

b) Column Performance:

After the initial move of the system from Beverly to M.I.T. the column was not disassembled. It was known to have a small mechanical misalignment in the upper stages so that the beam needed to have electrostatic steering potentials applied to the octopoles to permit it to be threaded through the apertures. This slightly degrades performance. Nevertheless we were able to get near 0.1 $\mu$m beam diameters (as demonstrated by exposure of PMMA) and were able to carry out a number of implantation experiments.

In Dec. 1987 we decided to disassemble the column, fly with the upper part to Hughes Research Laboratories, and perform the realignment. (Two identical columns are in operation at Hughes, and they have abundant experience in column alignment.) The column alignment was successful, but it took several iterations to reassemble all of the parts at M.I.T. Finally we have demonstrated beam diameters of 0.05 $\mu$m and below with $Be^{++}$ ions as shown by the PMMA exposures in Fig. 2. The resist profiles are straight or slightly undercut, and thus suitable for lift-off or plating to form x-ray masks, Fig. 3. The features we have been able to fabricate are the finest ever reported by focused ion beams, and because of the absence of proximity effect may be superior to features fabricated by e-beam lithography.

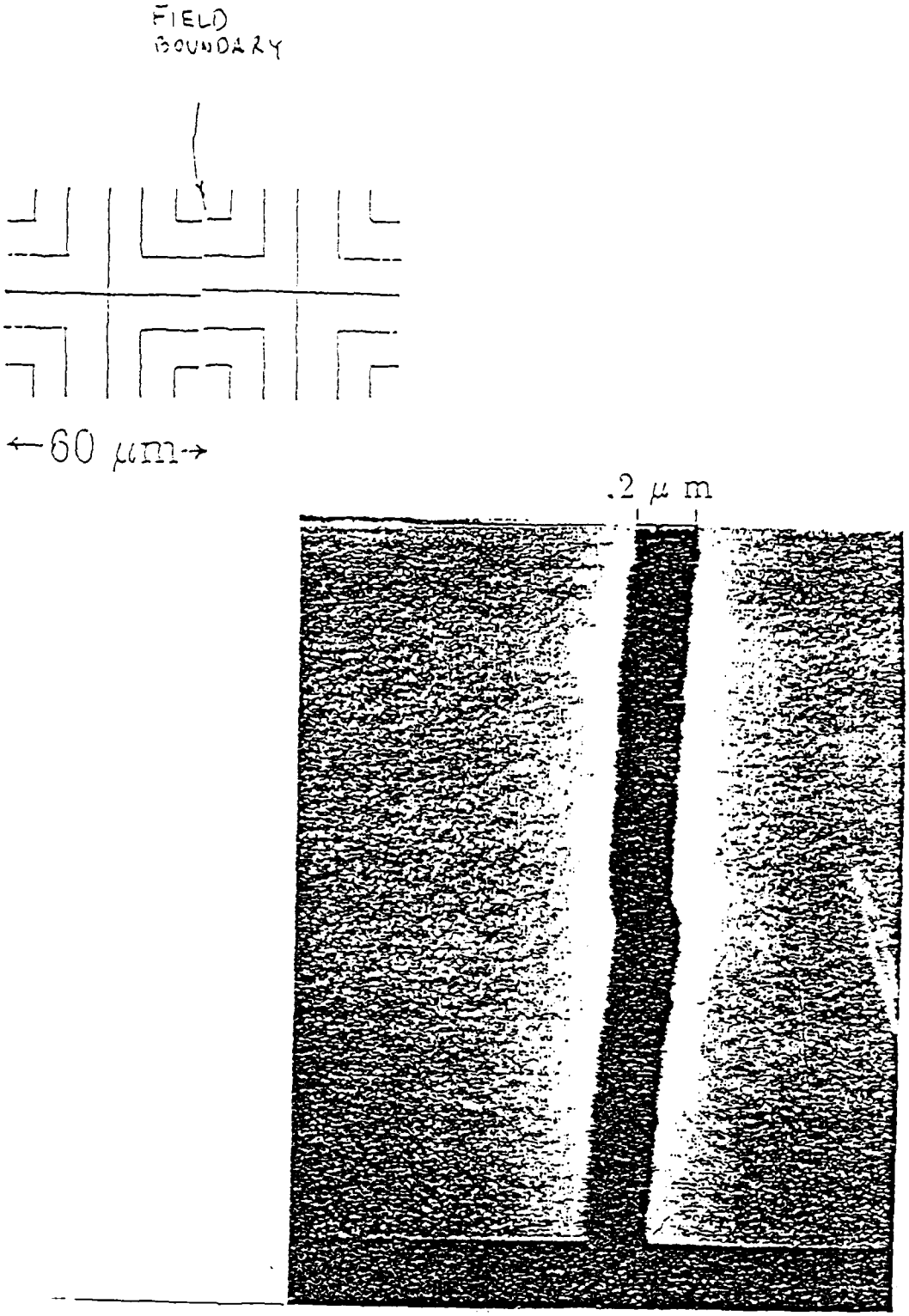


Fig. 4 Results of field abutment testing performed by exposing the pattern shown in the upper left in a repeated fashion. The stage is moved after each exposure. Its position is read by the laser interferometer to ±0.01 mm, and the deflection field is displaced to correct for the difference between the achieved and the desired stage location. The abutment error shows up as a discontinuity or shift in the lines as they cross the field boundary. The maximum abutment error is seen on the right to be 0.07 mm.

c) Alignment and Field Stitching

For research purposes manual alignment is quite adequate. The imaging (scanning ion microscope) mode is used to locate a feature on the wafer in the center of the screen. The table position which achieves this is then recorded, and the same is done for other alignment marks. The positions of desired implants is then easily calculated. Since the beam scanning signal, which is used for normal imaging, is not the same as the beam scanning signal used for beam writing, a small error can be generated. We have eliminated this error by writing software which scans the beam with the beam writing raster signal during imaging for alignment. The maximum "field" that the focused ion beam can address at full voltage is 128 $\mu$m x 128 $\mu$m. To write larger areas the stage has to be moved, and features which cross the boundaries have to be "stitched." Field stitching has been verified to be accurate to 0.06 $\mu$m. Lines of 0.2 $\mu$m width were written in PMMA so that they crossed the field boundaries. The parts of the lines which were in adjacent fields were offset by at most 0.06 $\mu$m, as shown in Fig. 4.

d) Pattern Translation Software

In many of our applications we wish to focused-ion-beam address features which have been generated by conventional lithography. For this the data which generated the lithography mask needs to be available for the focused ion beam. The pattern layout system used in the Microsystems Technologies Laboratory at M.I.T. is called MAGIC. We have written a program which converts the MAGIC format file to the focused ion beam

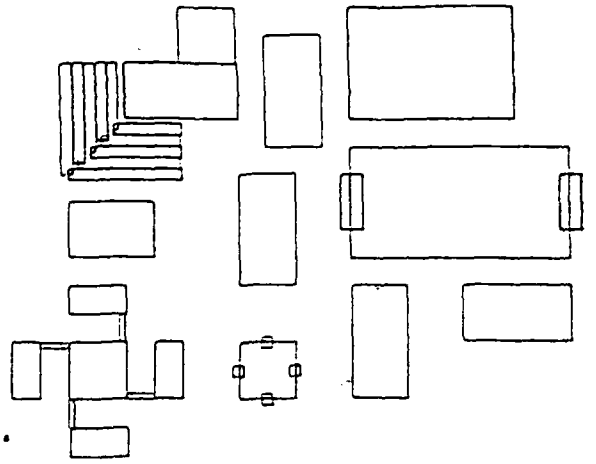

CAD System
(a)

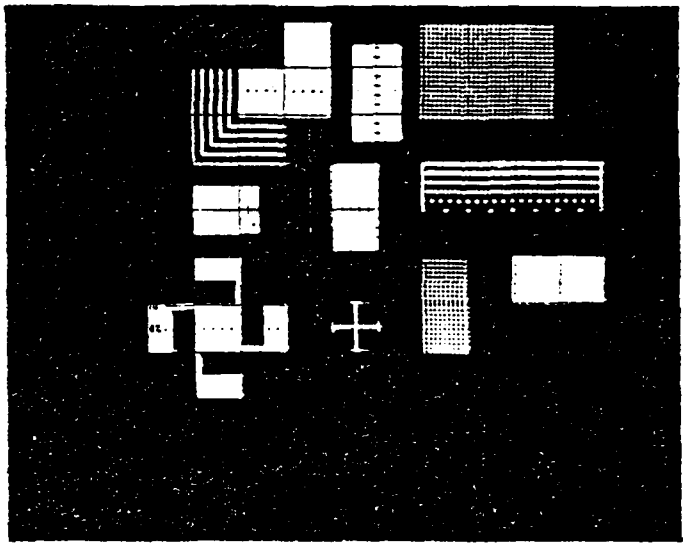

Oscilloscope on
FIB System
(b)

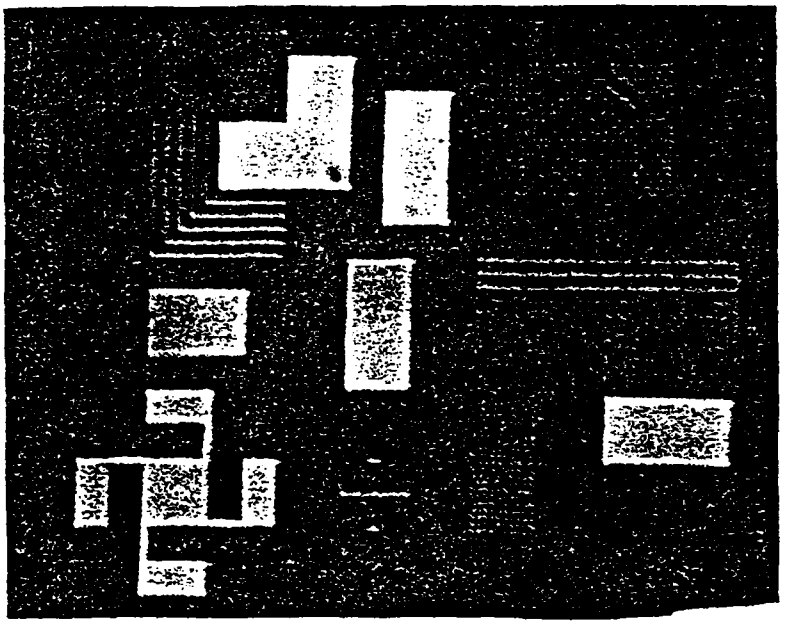

Written in PMMA
by
FIB System
(c)

Fig. 5 Pattern transfer from the CAD system, written in MAGIC (top), to the oscilloscope on the focused ion beam system (middle), where it is verified prior to writing, and finally (bottom) pattern written in PMMA. The ion dose, pixel spacing, and other features such as dose gradients are specified by "labels" on the edges of rectangles (not visible in the pictures).

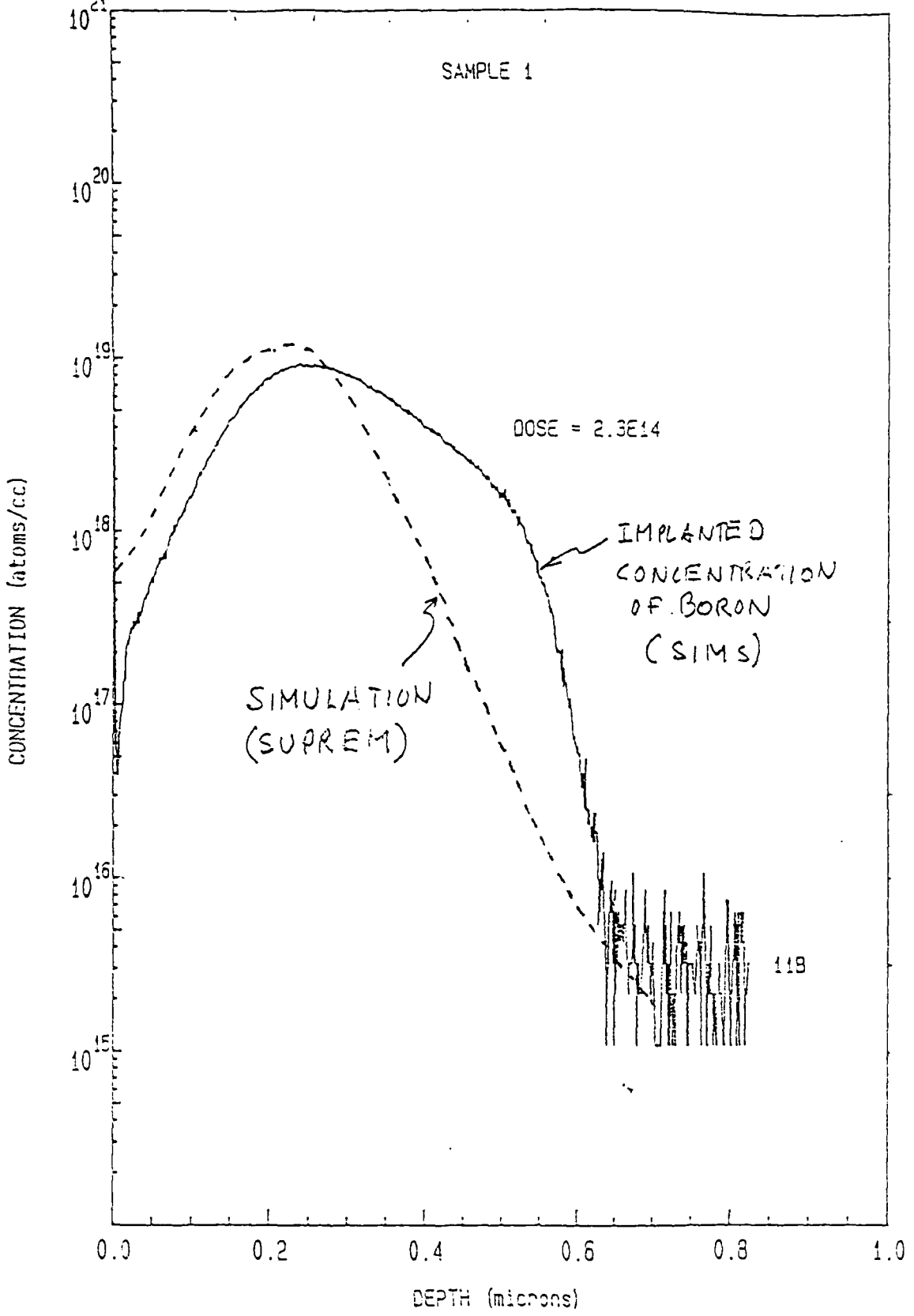


Fig. 6a) Concentration of dopants focused-ion-beam implanted into (100) Si at normal incidence as a function of depth. Measured by scanning ion mass spectrometry (SIMS). Simulated concentration for implantation into amorphous Si (or off the crystallographic axis) is shown for comparison. Due to channelling the implanted concentration is seen to be higher at the larger depth.

Boron implanted at 60 keV.

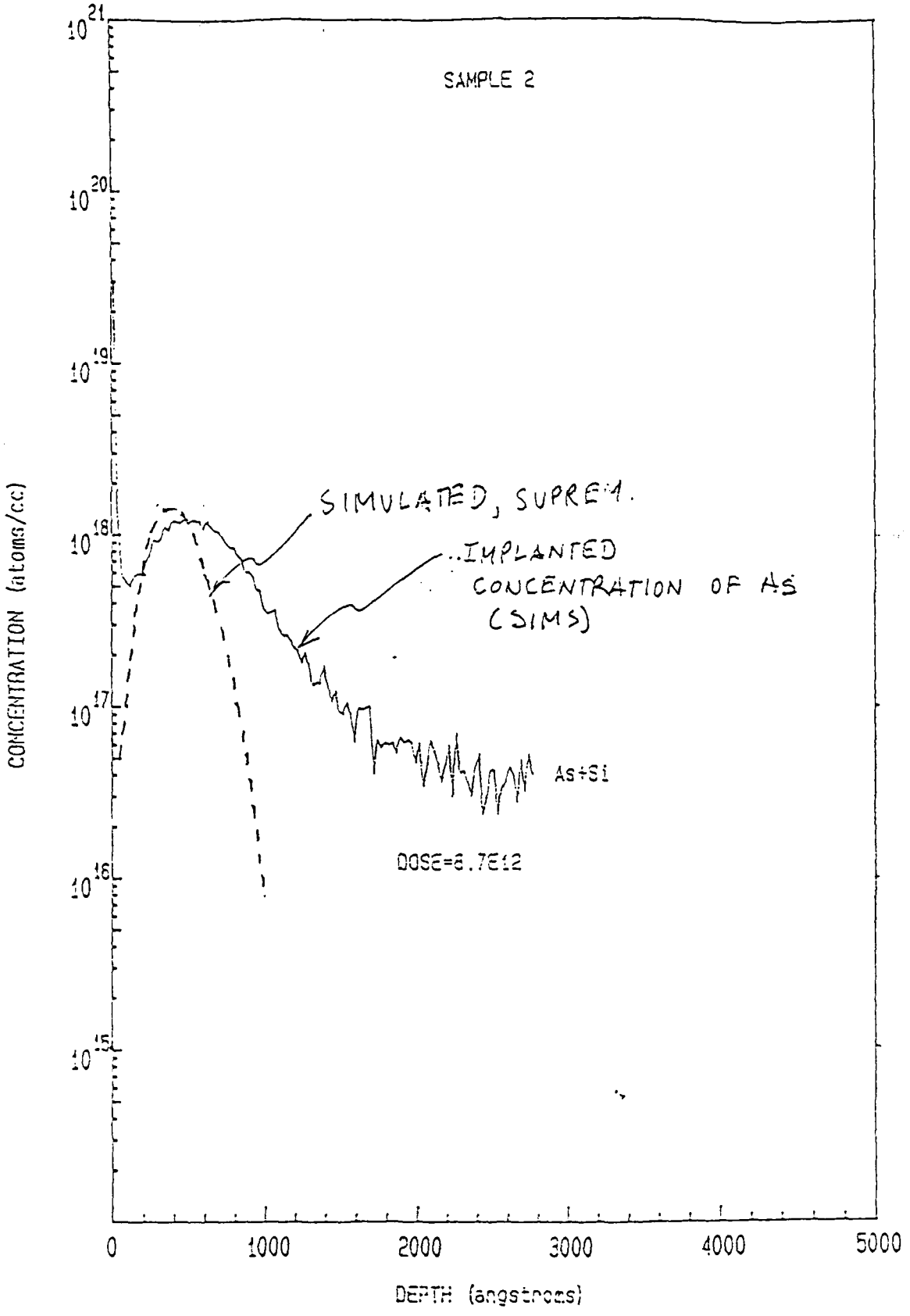


Fig. 6b) Same as Fig. 6(a) but with As implanted at 60 keV.

format. The ion dose to be given to each feature is specified by "labels" which can be attached to the edges of rectangles which make up a pattern. Fig. 5 shows an example of a simple pattern in magic as traced out in the CAD layout room, then as seen on the oscilloscope of the focused ion beam system, and finally as written in PMMA by the focused ion beam. Note that in the focused ion beam format each rectangle has been assigned a different dose, and also a different pixel spacing (dots in Fig. 5b). This capability enables us to write complex patterns which are registered to lithographically produced features without the need to enter each feature by hand.

Overall our focused ion beam column can write 0.05 $\mu$m features, and align them to existing features over many fields with 0.1 $\mu$m placement accuracy.

## 2. Focused Ion Beam Implants into Silicon

We have carried out test implants of As and B into Si wafers with (100) orientation. Since tilting the beam axis relative to the sample normal is difficult, and since use of off-axis samples is undesirable, channelling will be an issue. The extent of channelling was measured by analyzing the distribution profile of the dopants by scanning ion mass spectrometry (SIMS). The results are shown in Fig. 6.

We have operated several alloy sources of Pd/As/B obtained from Hughes Research. Even though those sources operate stably at Hughes, we have had problems of rapid drift and degeneration. On a recent visit to

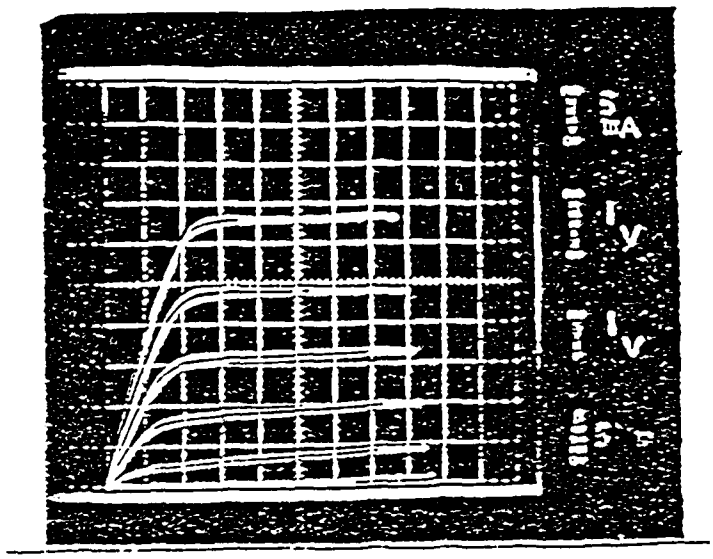


(a)

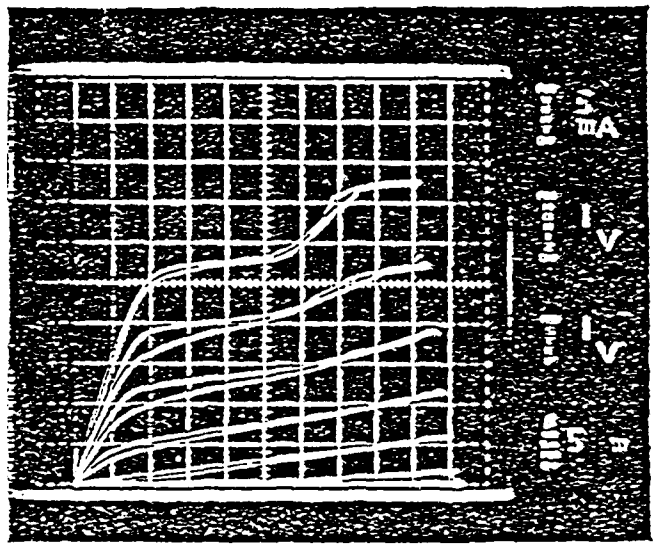


(b)

Fig. 7 Characteristics of laterally graded MESFET on GaAs. The background channel doping dose is $4.6 \times 10^{12}$ Si ions/cm$^2$. The gradient corresponds to a 15% increase in doping across the 1 $\mu$m gate length from source to drain.

a) Source grounded, drain voltage positive.

b) Drain grounded, source positive.

Vertical scale 5 mH/cm, horizontal 1 V/cm, top trace corresponds to 0V gate bias, next trace -1V etc. to -6V gate bias when device is turned off.

Hughes we observed the operation of these sources first hand, obtained new sources, and new insights. Apparently, these sources need to be pulsed periodically at very high current (500 $\mu$A), in order to restore stable operation. With this background, we are in a good position to carry out implants into the channels of Si MOSFET's.

Two types of Si samples are ready for implantation. One has series of 25 transistors in rows featuring various gate lengths from 2 to 9 $\mu$m. The other is simply the test pattern for the standard CMOS process in the Microsystems Technology Laboratories. These implants will be done in the near future.

## 3. Implantation into GaAs

### a) MESFET'S

Different doping gradients were implanted in the channel region between source and drain for 30 MESFET'S. The general trend was that in the forward direction (source end lower doped than drain end) the devices showed flattened $I_{DS}$ vs. $V_{DS}$ characteristics in the saturation region. If the contacts are reversed, on the other hand, the curves show an extra upward hump for high gate voltages. The forward and reverse characteristics are shown in Fig. 7. Uniformly doped control devices fell in between these characteristics. As a general trend some of the graded devices, operated in the forward direction, had a transconductance 20% higher than the uniformly doped control devices.

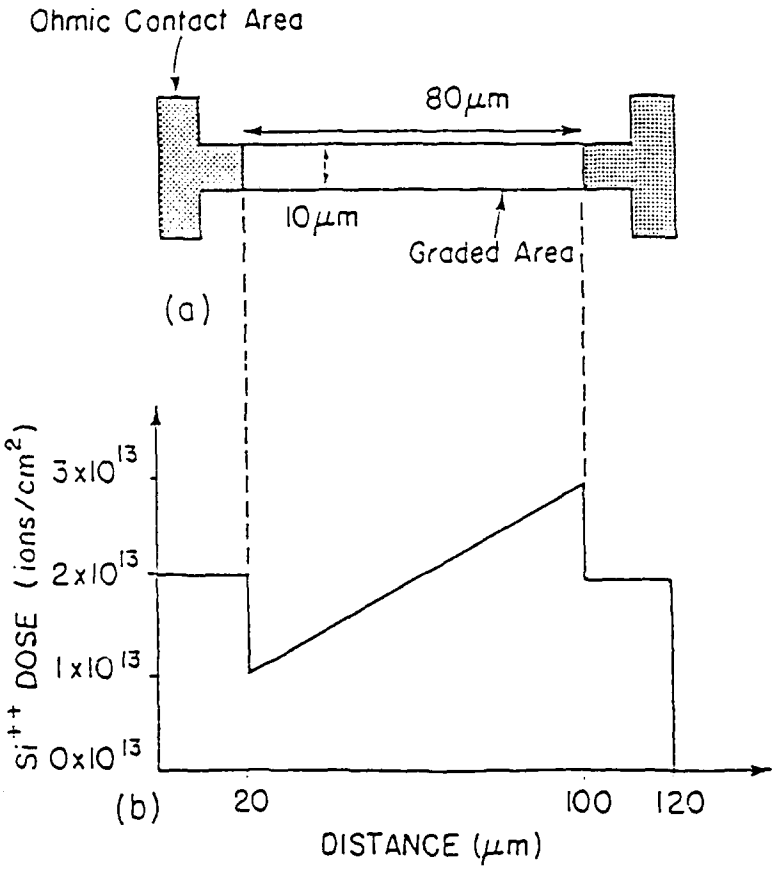


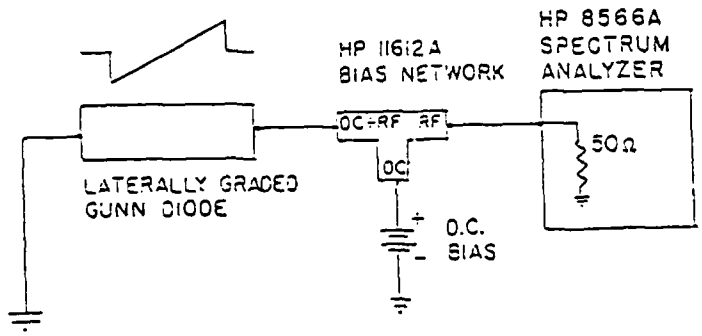


Fig. 8 Top: the layout of the Gunn diode on the surface of GaAs and the implantation dose as a function of position.
Bottom: the instrumentation and circuit used to measure the frequency of oscillation.

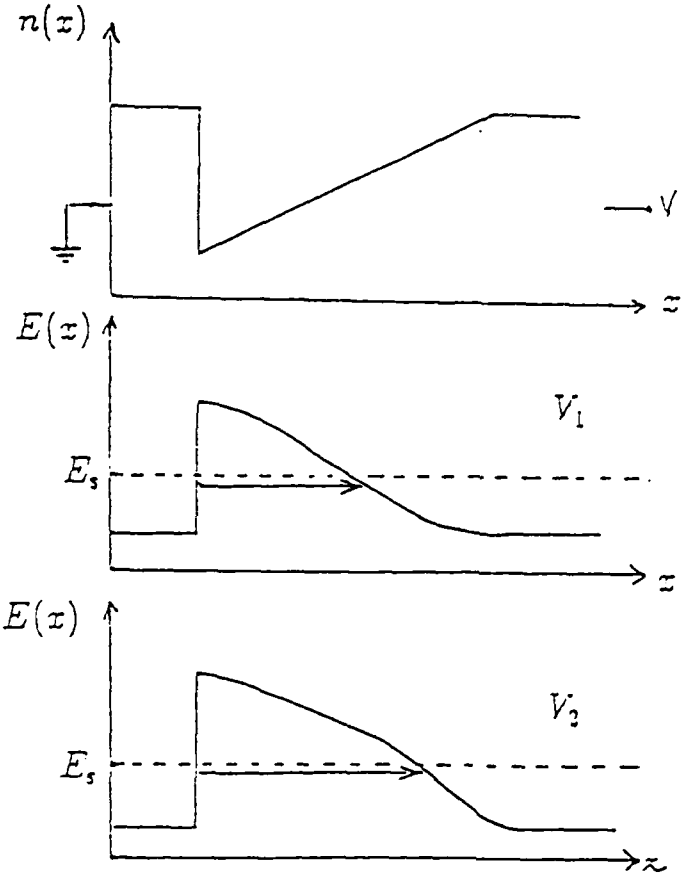


Ramp Doping Profile

Increasing $V$:

- Increases $l_{eff}$.
- Decreases $f = v/l_{eff}$.

Fig. 9 Principle of operation of the tunable Gunn diode. Top schematic of doping profile. Middle: Electric field as a function of position for a given applied bias. Note that the field is highest where the doping concentration is lowest. The Gunn domain nucleates at the point of highest yield and propagates to the left until the field falls below the domain sustaining value $E_s$ ( 2 kV/cm). Bottom: If the bias voltage is increased the field rises and the domain can propagate further. Thus the frequency is lower.

These devices had gate lengths of 1 $\mu$m and except for the implantation were fabricated by optical lithography. We expect the performance improvements to be more significant in submicron gate devices. Such devices will be fabricated in the future where both the implantation and the lithography for gate definition will be carried out by the focused ion beam. Since the same instrument is used, the alignment of the gate electrode to the region of implanted gradient is expected to be better than 0.1 $\mu$m.

b) Tunable Gunn Diodes

A new device has been conceived which uniquely exploits the ability to fabricate a gradient of doping. Gunn diodes are used as high frequency oscillators. In the configuration where the current flows between two contacts parallel to the surface the diode can be made into a simple voltage controlled oscillator by implanting a gradient of doping from one contact to the other. In this case the distance over which a Gunn domain can propagate will depend on the bias. Thus, the frequency can be tuned by changing the bias. The operation of this device is shown in Figs. 8 & 9 and is described in more detail in Appendix II. The device built can be tuned from 6 to 23 GHz by varying the bias, Fig. 9.

We have also built the Gunn oscillators as control devices with uniform profiles and with profiles which had a single step function. The uniform devices oscillated at about 1.6 GHz and the device with

Abrupt Transition

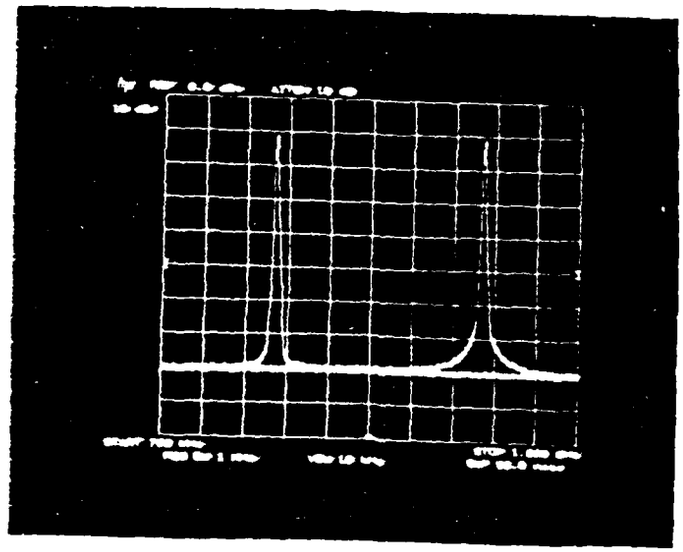

← -10 dBm

$f = 780$ MHz
$V_2 = 35.2$ V

$f = 916$ MHz
$V_1 = 35.1$ V

Fig. 10 A Gunn diode fabricated with a step function in the doping profile can oscillate at two frequencies and can shift between them with a small change in bias.

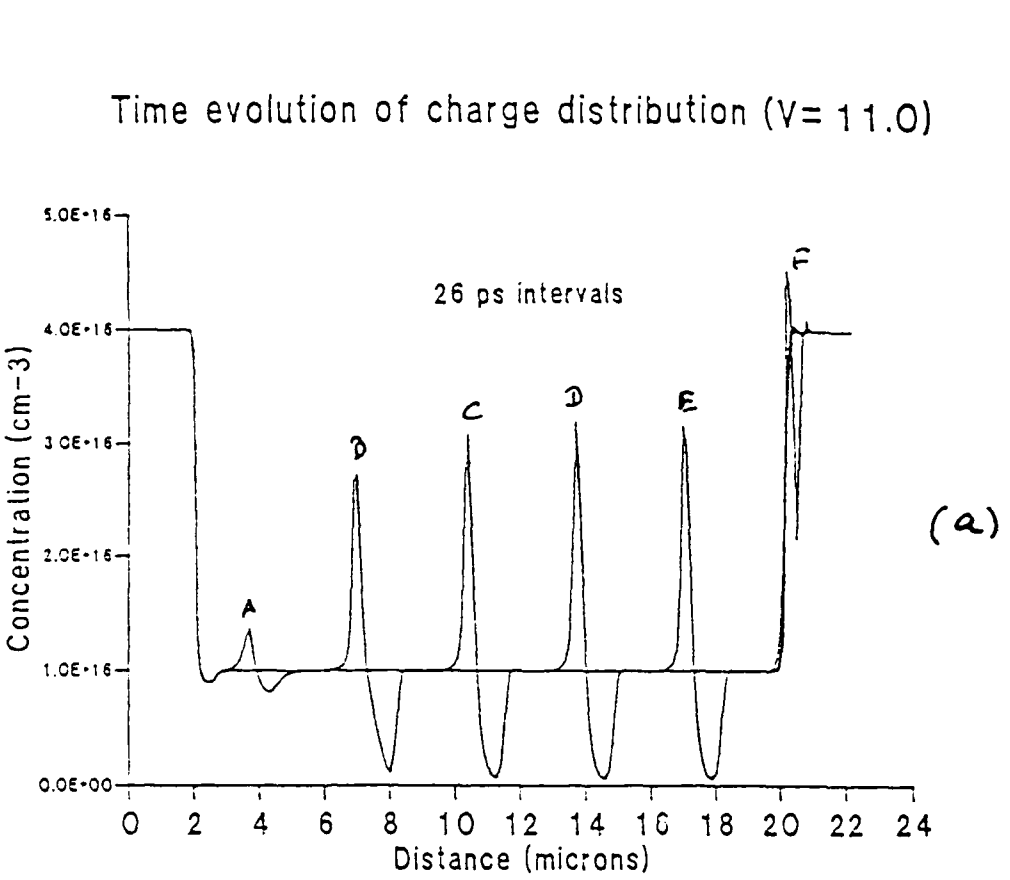


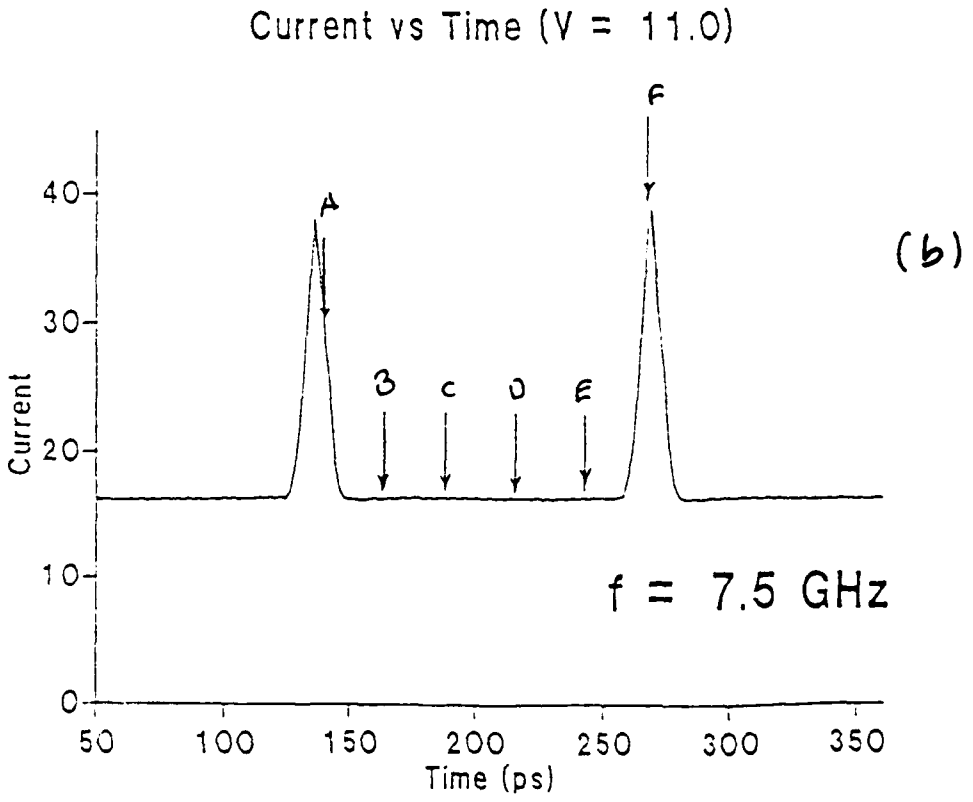


Fig. 11 a) Carrier distribution as a function of distance, high in the contact regions and uniform in between. Superimposed on it is the Gunn domain (charge dipole) at various positions as it propagates through the device.

b) The current vs. time in the same device. Arrows correspond to the times at which the "snapshots" are taken in Fig. 1(a).

(a)



(b)

Fig. 12 a) Same as Fig. 11a) but with a gradient of doping between the contracts.

b) Current vs. time as in Fig. 11b).

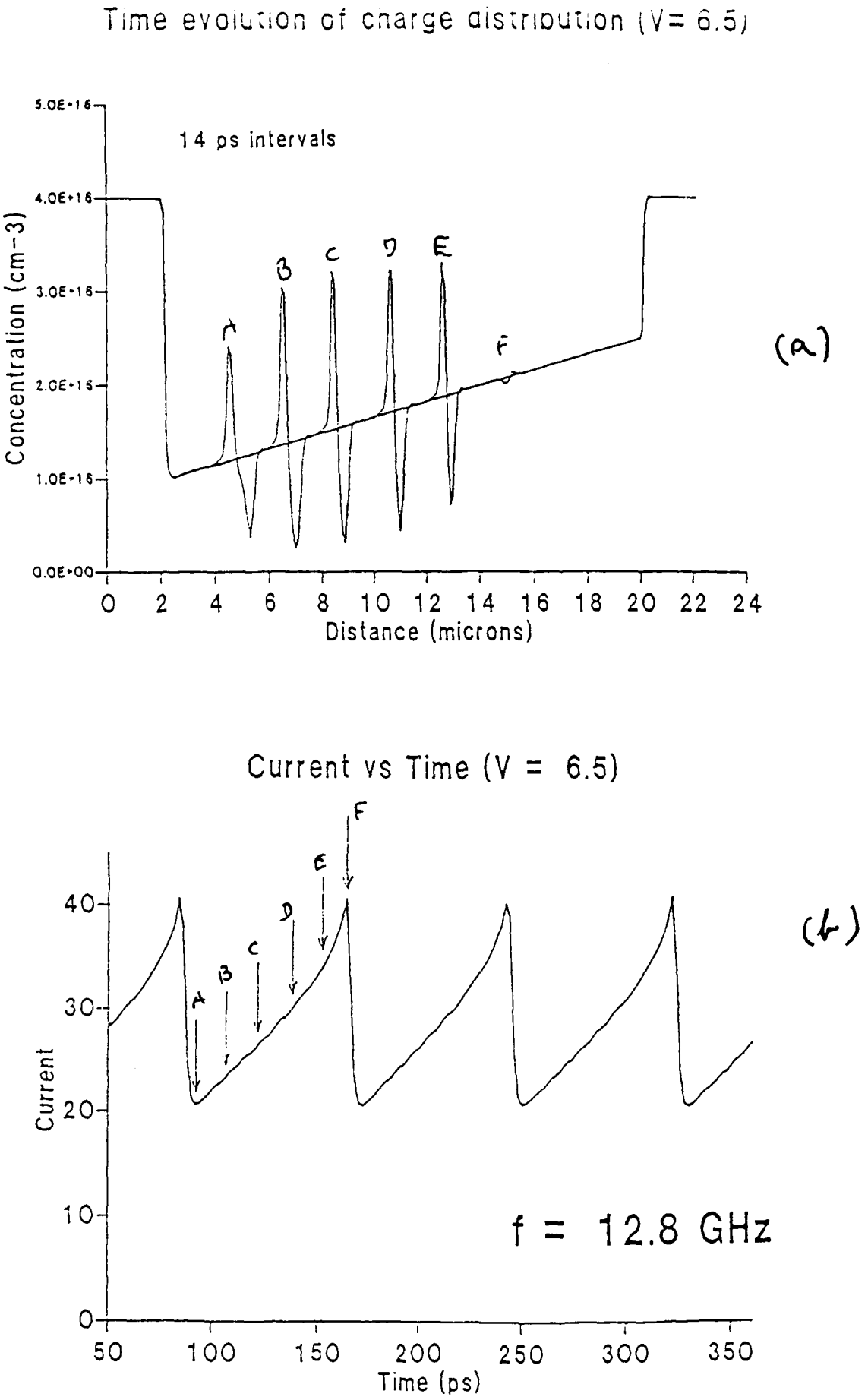


Fig. 13 a) Same as 12a) at a lower bias voltage now the domain does not propagate as far, and the frequency is higher.

b) Current vs. time.

the single step in the doping could be switched between two frequencies, 0.78 GHz and 0.92 GHz with a small change in bias voltage. The results are shown in Fig. 10. The power output in the uniform and the stepped profile device is about -10 dBm. A number of subsequent devices have been fabricated but have not operated because of a faulty annealing step. A new optical lithography mask has been generated and a program has been written to implant 100 Gunn diodes on a single wafer. This implantation is aligned to the optically generated contact pads and is done automatically. The operation of tunable Gunn diodes has been modelled and will be described in the next section.

## 4. Numerical Simulation

### a) Gunn Diodes

We have conducted numerical simulations of laterally graded Gunn diodes using a transient energy model derived from Boltzmann's transport equation in the relaxation time approximation.[8] The solution is performed in the time domain and allows us to observe domain nucleation, motion, and discharge. Figures 11 through 13 display some simulation examples. Fig. 11(a) shows the position at regular time intervals of a Gunn domain in a uniformly doped Gunn diode. The dipole domain propagates from the cathode (on the left), where it nucleates, to the anode (on the right), where it discharges. A current pulse is obtained every time a domain

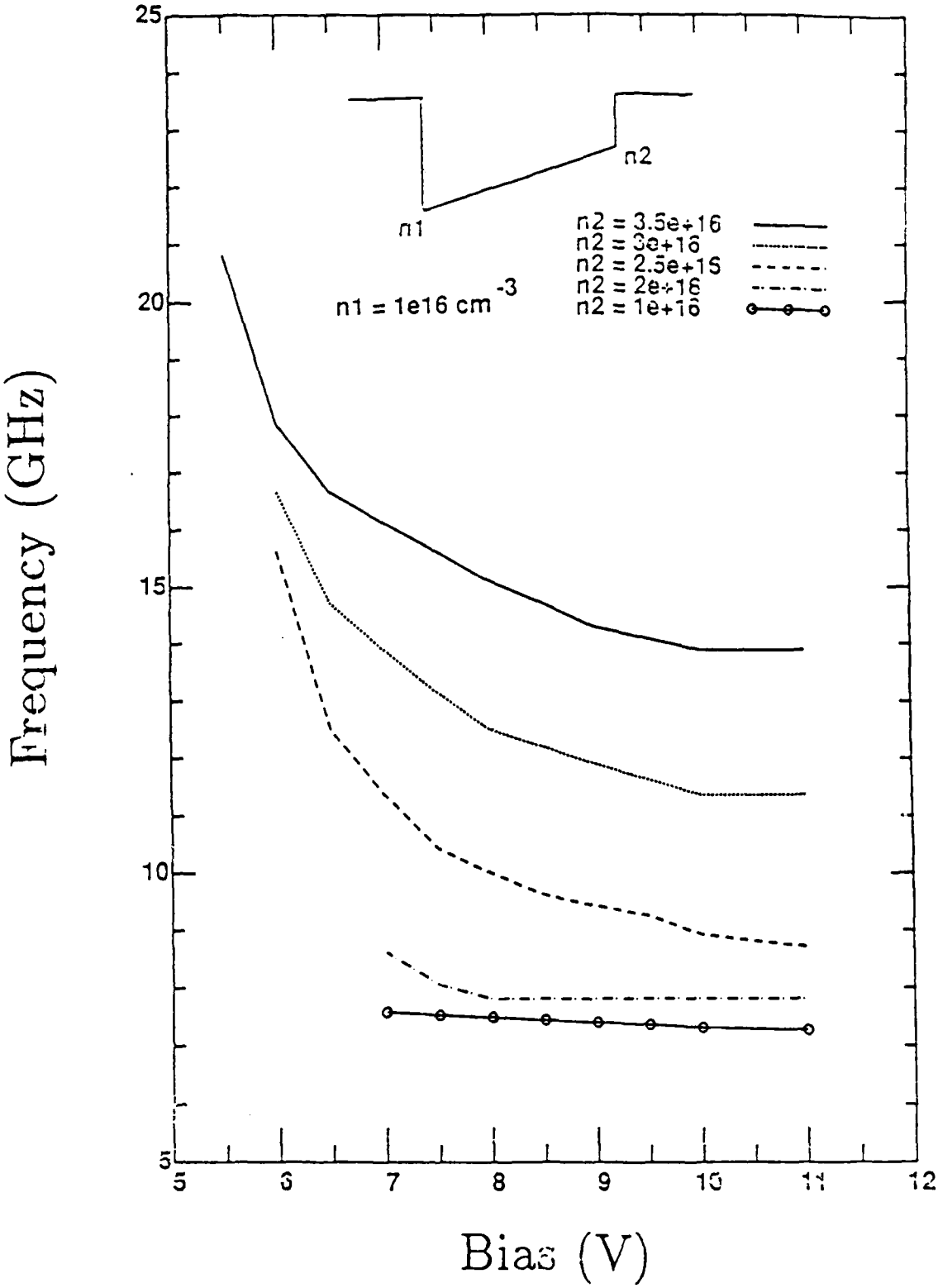


Fig. 14 The frequency vs. bias simulated for different slopes of the graded profile. Note the qualitative similarity to the experimental plot Fig. 3 of Appendix II.

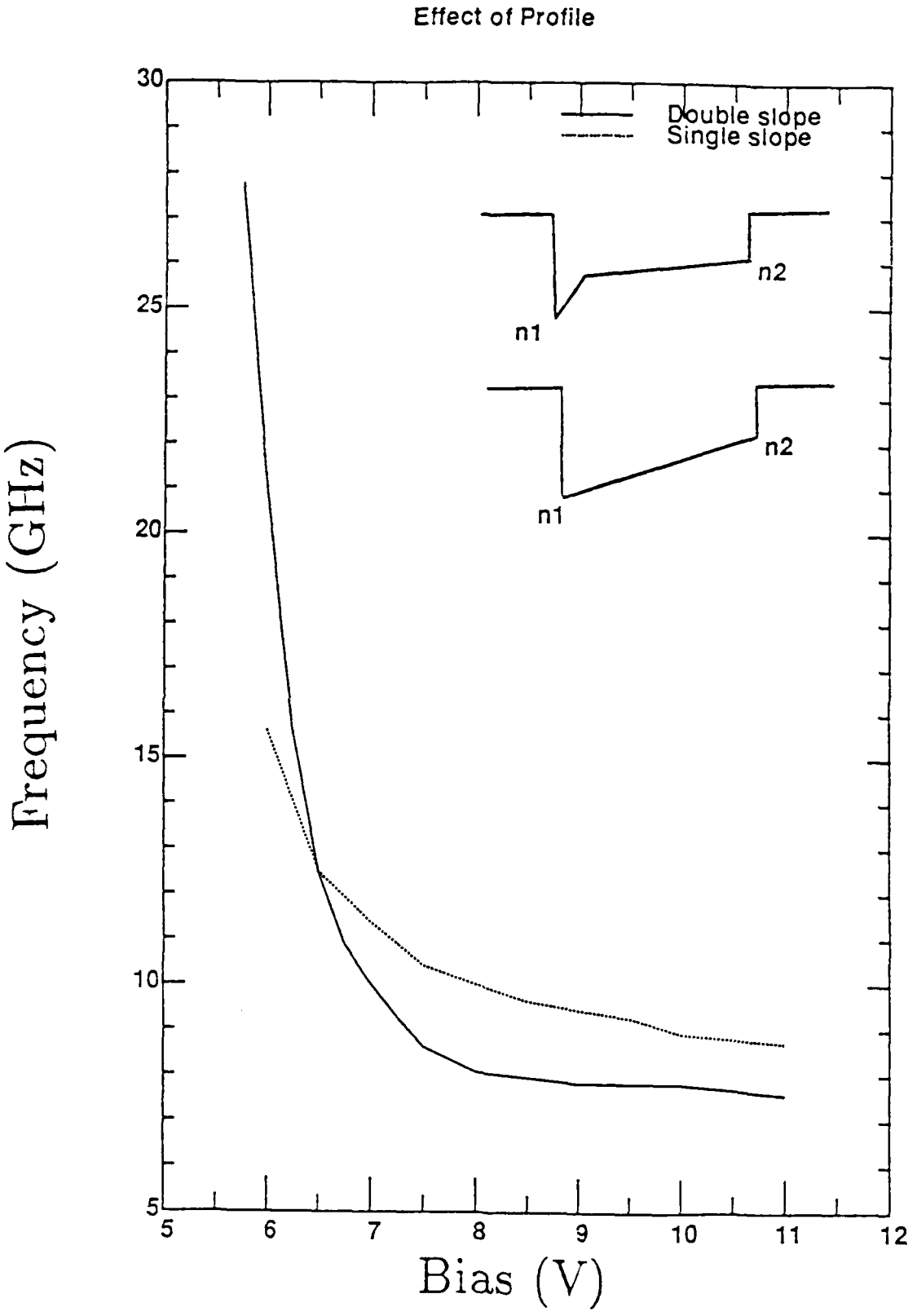


Fig. 15 Frequency vs. bias voltage for double slope and single slope gradient. Note that the double slope can considerably enhance the frequence tunability.

discharges (Fig. 11 (b)). The frequency is relatively constant as a function of bias.

In Fig. 12 (a) the constant doping profile has been replaced with a ramp. At a bias of 11 volts the domain dissipates just before reaching the anode. The current waveform is a sawtooth of frequency 8.9 GHz (Fig. 12 (b)). As the bias is decreased to 6.5 Volts, the point at which the domain dissolves is shifted towards the cathode (Fig. 13 (a)). The frequency of oscillation increases to 12.5 GHz because the domain transit length has decreased (Fig. 13 (b)). Multiple simulations can be compiled to obtain frequency versus bias curves. Fig. 14 for example, shows the effect of increasing the slope of the doping ramp: a shift towards higher frequencies is obtained. The effect of other doping profiles on the tunability characteristics can be predicted as well. For example, the notched ramp of Fig. 15 leads to greater tunability than a simple ramp. Increasing the depth of the notch at fixed bias is found to increase the frequency of oscillation (a range 40 to 80 GHz has been predicted for various notch depths). This suggests a three terminal graded Gunn diode where a Shottky gate placed near the cathode simulates the effect of a doping notch. A fixed bias would be applied across cathode and anode and the gate would be used to modulate the frequency of oscillation over a wide range. We plan to build the next tunable Gunn diodes according to these simulations, in both the two terminal and three terminal versions.

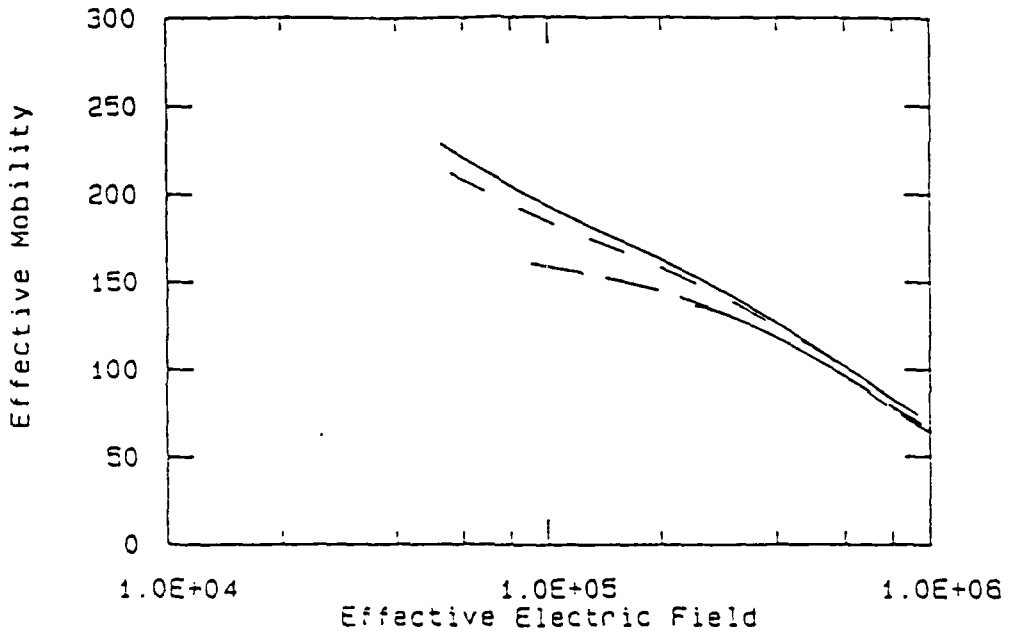


Fig. 16 Simulated $\mu_{eff}$ versus $E_{eff}$ for holes at 300 K. The substrate concentrations are $3 \times 10^{14}$ $cm^{-3}$ (solid line), $1.22 \times 10^{15}$ $cm^{-3}$ (dashed line), $1.3 \times 10^{16}$ $cm^{-3}$ (long-dashed line) and $1.4 \times 10^{17}$ $cm^{-3}$ (dash-dotted line). The simulated fixed oxide charge density is $10^{11}$ $cm^{-2}$.

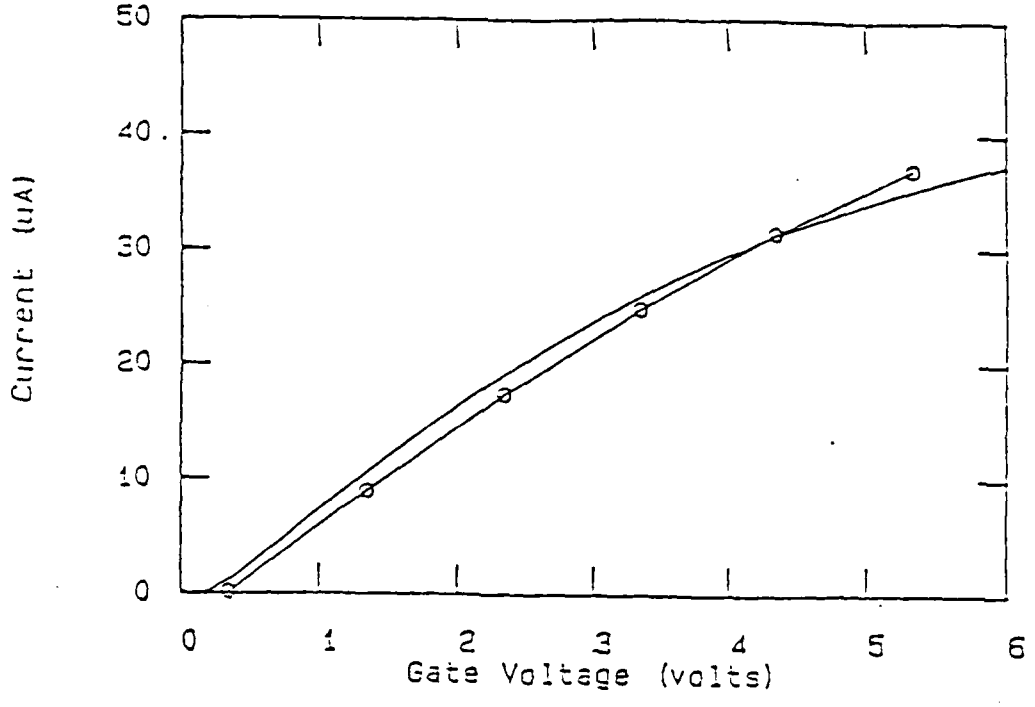


Fig. 17 Comparison of Experimental and Simulated Currents at 300 K with $V_{ds}$ = 0.1 volts. The measured (o) and the simulated (solid line) currents of the SEDAN are shown.

b) Mobility Model in MOSFET's

In order to model the characteristics of MOSFET's with doping gradients in the channel region sophisticated 2 dimensional simulation is needed. This kind of simulation in turn requires that the mobility be known as a function of the electric field in the inversion layer, or equivalently as a function of position. This microscopic mobility model is developed based on experimental measurements of the effective mobility as a function of the effective electric field in the inversion layer of MOSFET's. Experimentally, it has been shown that the effective mobility of inversion-electrons and holes in MOSFET's is uniquely related to the electric field in the inversion layer perpendicular to the $Si/SiO_2$ interface and is nearly independent of channel doping. The mobility model in any simulator should be such that the "collective" or effective mobility predicted by the microscopic mobility of simulated inversion carriers reproduces the experimental observations. Unfortunately, experience has shown that this is not the case in the public domain simulators which have been examined. Therefore, the new microscopic mobility model is constructed to predict the mobility of electrons and holes in Si near the $SiO_2$ interface. (Fig. 16) The mobility model was inserted in a modified device simulation program (called SEDAN) to predict the experimental characteristics of a long channel transistor, which was also fabricated. The agreement between the predicted and measured source drain current vs. gate voltage is seen to be good, Fig. 17.

c) Simulation of Focused Ion Beam Implanted Profiles

The focused ion beam is known to have a Gaussian beam profile. In addition, the beam, even if it had zero diameter in the simplest model, is assumed to spread as it enters a solid into a Gaussian distribution normal to the surface and along the surface. The distribution normal to the surface is taken to be a Gaussian with a standard deviation of $\Delta R_p$ called the range straggle, and parallel to the surface it is a Gaussian of standard deviation $\Delta R_t$ which is the transverse straggle. The diffusion of dopants during annealing further broadens these Gaussians. Thus, for example, the distribution of dopants along the surface normal to a focused-ion-beam-implanted line after annealing is a Gaussian whose standard deviation (half width) is just

$$\sigma = (R^2 + \Delta R_t^2 + 2Dt)^{1/2}$$

where R is the half width of the incident Gaussian beam, D is the diffusion coefficient, and t the time of diffusion. Any arbitrary implant distribution is modeled simply as a sum of Gaussians. This model requires little computation time, is accurate, and is described in more detail in Appendix III.

## References


1. R.L. Seliger and W.P. Fleming, J. Vac. Sci. Technol. 10, 1127 (Nov./Dec. 1973), abstract. Article: J. Appl. Phys. 45, 1416 (Mar. 1974).
   R. Levi-Setti, Scanning Electron Microscopy 1974 (Part I), Proc. 7th Annual Scanning Electron Microscope Symposium, IIT Res. Inst. (Chicago, Apr. 1974), p. 125.
   J.H. Orloff and L.W. Swanson, J. Vac. Sci. Technol. 12, 1209 (1975).

2. R. Clampit, K.L. Aitken and D.K. Jefferies, J. Vac. Sci. Technol. 12, 1208 (1975) (abstract), R. Clampit and D.K. Jefferies, Nucl. Instr. and Methods, 149, 739 (1978).

3. R.L. Seliger, V.W. Ward, V. Wang, and R.L. Kubena, Appl. Phys. Lett. 34, 510 (1979).

4. W.M. Clark, R.L. Seliger, M.W. Utlaut, A.E. Bell, L.W. Swanson, G.A. Schwind, and J.B. Jergenson, J. Vac. Sci. Technol. B5, 197 (1987).

5. V.Wang, J.W. Ward and R.L. Seliger, J. Vac. Sci. Technol. 19, 1158 (1981).

6. R.H. Walden, A.E. Schmitz, L.E. Larson, A.R. Kramer, and J. Pasiecznik, "A 4-bit, 1 GHz Sub-Half Micrometer CMOS/SOS Flash Analog-to-Digital Converter Using Focused Ion Beam Implants," Hughes Research Laboratories (Preprint).

7. J. Melngailis, J. Vac. Sci. Technol. B5, 469 (Mar/Apr 1987).

8. K. Ismail, O.L. El-Sayed, and G. Salmer, "Doping profile optimization in GaAs MESFET's," presented at the 15th ESSDERC, Aachen, W. Germany, Sept. 1985.

D. Personnel Who Have Worked on the Program or Have Collaborated:

Jarvis B. Jacob, Graduate Student, Electrical Eng. and Computer Science

Henri Lezec, Graduate Student, Electrical Eng. and Computer Science

Christian Musil, Graduate Student, Physics, Hughes Fellow

Khalid Ismail, Graduate Student, Electrical Eng. and Computer Science

Rex B. Lowther, Visiting Scientist from Harris Corp.

James Murguia, Graduate Student, Electrical Eng. and Computer Science

Len Mahoney, Lincoln Laboratory

Mark Shepard, Research Engineer

Dimitri Antoniadis, Assoc. Prof. of EE&CS, Co-Principal Investigator

John Melngailis, Principal Research Scientist, RLE, Principal Investigator

E. Publications

"Simulation of Implantation and Diffusion Profiles Made With a Focused Ion-Beam Implanter," R.E. Lowther, J.B. Jacobs, and D.A. Antoniadis. IEEE Tran. Electron Dev. Lett. Vol. ED-23, 1251(1986).

"Focused ion beam technology and Applications, a review," J. Melngailis, J. Vac. Sci. Technol. B5, 469 (1987).

"A Tunable-Frequency Gunn Diode Fabricated by Focused Ion-Beam Implantation," H.J. Lezec, K. Ismail, L.J. Mahoney, M.I. Shepard, D.A. Antoniadis, J. Melngailis, Electron Dev. Lett. Vol. ED-9, 476 (1988).

Thesis

"Modeling the Effects of the $Si/SiO_2$ Interface Proximity and Transverse Field on Carrier Mobility in MOSFET's." Jarvis B. Jacobs, July 1987, M.S. Electrical Engineering and Computer Science.

Seminars and Conference Presentations

June 1985, "Focused ion beams in I.C. restructuring and other applications", J. Melngailis, SRC In-Situ Processing Workshop.

May 1986, "Focused ion beam fabrication", J. Melngailis, ARO Workshop on Technologies of Ultrasmall Electronic Devices. Clemson, SC.

March 1987, "Focused ion beam microfabrication", J. Melngailis, American Vacuum Society Local Chapter Meeting. Bedford, MA.

Dec. 1987 "Focused ion beam implantation," H.J. Lezec, L.J. Mahoney, M.I. Shepard, and J. Melngailis, VLSI Review at M.I.T.

Mar. 1988 "Focused ion beam microfabrication," J. Melngailis, SPIE Symposium on Microlithography, Santa Clara, Calif. (invited talk).

Mar. 1988 "Focused ion beam microfabrication," seminar at TRW, Redondo Beach, Calif.

June 1988 "Tunable frequency of Gunn diodes fabricated by ion beam implantation," H.J. Lezec, K. Ismail, L.J. Mahoney, M.I. Shepard, D.A. Antoniadis and J. Melngailis EIPB Symposium Ft. Lauderdale Fla.

June 1988 "Tunable frequency of Gunn diodes fabricated by ion beam implantation," H.J. Lezec, K. Ismail, L.J. Mahoney, M.I. Shepard, D.A. Antoniadis and J. Melngailis DRC Boulder Colorado.

Sept. 1988 "Focused ion beam technology and applications," Seminar IBM Research Laboratory Zürich.

Sept. 1988 "Focused ion beam microfabrication," Seminar Siemens Research Lab. München.

Sept. 1988 "Focused ion beam induced deposition of metals," P.G. Blauner, J.S. Ro, Y. Butt, C.V. Thompson and J. Melngailis. Microcircuit Engineering Conf.

Sept. 1988 "Focused ion beam induced deposition," J. Melngailis, Amer. Vac. Soc. Annual Meeting, Atlanta Ga, (invited talk).

Appendix I

## Critical Review

# Focused ion beam technology and applications

John Melngailis
*Research Laboratory of Electronics, Massachusetts Institute of Technology, Cambridge, Massachusetts 02139*

(Received 19 August 1986; accepted 29 December 1986)

Ions of kiloelectron volt energies incident on a solid surface produce a number of effects: several atoms are sputtered off, several electrons are emitted, chemical reactions may be induced, atoms are displaced from their equilibrium positions, and ions implant themselves in the solid, altering its properties. Some of these effects, such as sputtering and implantation are widely used in semiconductor device fabrication and in other fields. Thus the capability to focus a beam of ions to submicrometer dimensions, i.e., dimensions compatible with the most demanding fabrication procedures, is an important development. The focused ion beam field has been spurred by the invention of the liquid metal ion source and by the utilization of focusing columns with mass separation capability. This has led to the use of alloy ion sources making available a large menu of ion species, in particular the dopants of Si and GaAs. The ability to sputter and to also induce deposition by causing breakdown of an adsorbed film has produced an immediate application of focused ion beams to photomask repair. The total number of focused ion beam fabrication systems in use worldwide is about 35, about 25 of them in Japan. In addition, there are many more simpler focused ion beam columns for specialized uses. The interest is growing rapidly. The following range of specifications of these systems has been reported: accelerating potential 3 to 200 kV, ion current density in focal spot up to 10 A/cm$^2$, beam diameters from 0.05 to 1 $\mu$m, deflection accuracy of the beam over the surface $\pm 0.1\,\mu$m, and ion species available Ga, Au, Si, Be, B, As, P, etc. Some of the applications which have been demonstrated or suggested include: mask repair, lithography (to replace electron beam lithography), direct, patterned, implantation doping of semiconductors, ion induced deposition for circuit repair or rewiring, scanning ion microscopy, and scanning ion mass spectroscopy.

## I. INTRODUCTION

Lithography is the key patterning step in all current integrated circuit fabrication. Resist is spun on a wafer, baked, and exposed in an intricate pattern, usually by ultraviolet light, although x rays and electron beams are beginning to play a role. After development and baking the surface is left partly covered by an inert organic film that "resists" various treatments to which the bare surface is subjected. The treatment may, for example, be material removal by a wet chemical etch or by a gaseous plasma; doping by ion implantation (broad beam); or addition of material by evaporation (lift-off). This patterned alteration of a surface using lithography is a multistep process, and treats the whole wafer in the same way.

Ion beams focused to submicrometer diameters offer a radical departure from this conventional fabrication routine. Resist may be eliminated and the dose of ions can be varied as a function of position on the wafer. This is illustrated in Fig. 1. The focused ion beam fabrication is a serial process, and the wafer is exposed point by point. Needless to say this is slow and some of the applications can be considered only over very limited sample areas. This will be discussed below as each application is examined in detail.

The first efforts to focus an ion beam for the purposes of integrated circuit fabrications date back to 1973.[1] The source of ions was a conventional implanter, and the beam diameter achieved was only 3 $\mu$m. However, the potential elegance of the technique was clear then. Polymethylmethacrylate (PMMA) (an electron and x-ray resist) was exposed, and direct maskless implantation into Si was carried out. Because the source of ions was not bright, the technique was very slow.

An important simultaneous activity was the development of the scanning proton microscope.[2] Here, a fine field emission tip was cooled to cryogenic temperatures and used to ionize hydrogen[2-5] or argon.[5] This type of source had a brightness of $10^4$ to $10^5$ times higher than the above-mentioned implanter, but, except for mention of micromachining[3] and creation of damage sites,[4] most applications appear to be aimed at proton microscopy.[6,7] The ion optics developed permitted resolutions of 0.2 $\mu$m to be attained.[4,6] However, because only gaseous elements were used, and the cryogenic source was cumbersome, the applications to microfabrication did not develop.

The liquid metal ion source[8,9] provided similarly high brightness, was easy to operate, and opened the menu to a larger variety of ion species. This greatly spurred applications. A beam of gallium ions was focused down to a diameter of 0.1 $\mu$m at a current density (at the focal spot) of 1.5 A/cm$^2$ ($10^{19}$ ions/cm$^2$ s) (Ref. 10). Lines of 0.1-$\mu$m width were milled in 40-nm-thick gold films on silicon.

The development of liquid metal alloy sources, which emitted ions of the typical semiconductor dopants, combined with the development of a crossed electric and magnetic field mass separator in the ion column[11,12] even further broadened the field of application. Now an ion beam with the ion species of choice could be focused on the sample. In particular, both silicon and GaAs could be doped either *n* type or *p* type. In the last five years the focused ion beam

 0734-211X/87/020469-27$01.00 © 1987 American Vacuum Society 

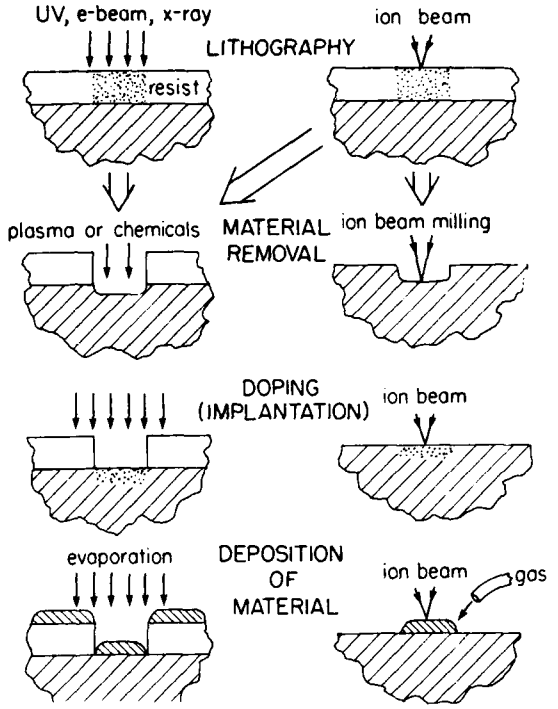


FIG. 1. Conventional resist based fabrication is shown on the left, i.e., resist is exposed and developed, then material is removed from the unprotected area or the unprotected area is implanted, or material is deposited on the exposed area. The focused ion beam can expose resist, but more importantly, it can remove material, implant, or deposit in a fine pattern *without* the use of resist or mask.

research has experienced rapid growth, particularly in Japan.

Much has been published in the field of focused ion beam fabrication, including a number of reviews. But the more comprehensive reviews are not recent,[13–15] and many of the others are relatively brief or directed at special audiences.[16–27]

The goal of this review is to provide a summary of the entire field of focused ion beam fabrication with an emphasis on its applications. First the interaction of ions with matter will be summarized. Second, machine technology will be discussed. Finally, each of the classes of application will be examined.

## II. INTERACTION OF IONS WITH MATTER

Due to the widespread use of ion implantation for integrated circuit fabrication and for other applications, there is a vast literature on the field of ion interaction with solids.[28–30] Those aspects most relevant to focused ion beam fabrication will be briefly summarized, and some detail on heating, which is particular to focused ion beams, will be presented.

### A. Ion distribution in a solid

In high performance integrated circuits doping of silicon is achieved by ion implantation.[31,32] Typical implantation energies used are in the 10- to 200-keV range. (This energy range is also accessible by focused ion beam machines.)

The incident ion loses energy to the electrons of the solid as well as to the atoms. Due to Coulomb interaction the passing ion excites the electrons in the solid to bound states or to continuum states. This is a smooth and predictable process. The loss to atoms, on the other hand, is in part due to a finite number of random collisions with a significant energy loss per event. Thus the ion is deflected from its path, and the atom in the solid is displaced from its lattice site. The ions, therefore, penetrate to an average depth $R_p$ called the range. If a Gaussian is fit to the distribution of ions around the depth $Z$, this Gaussian has a form $\exp[-(Z-R_p)^2/2(\Delta R_p)^2]$, where $\Delta R_p$ is called the range straggle. In addition, the collisions also produce an uncertainty in the transverse (along the surface) position of the ion in the solid. This is characterized by transverse straggle $\Delta R_t$. Plots of $R_p$, $\Delta R_p$, and $\Delta R_t$ for the typical dopants of Si exist.[31,32] For example, for a 100-keV $B^+$ $R_p = 0.3\,\mu$m, $\Delta R_p = 0.07\,\mu$m, and $\Delta R_t = 0.08\,\mu$m while for 100-keV $As^+$, $R_p = 0.06\,\mu$m, $\Delta R_p = 0.02\,\mu$m, and $\Delta R_t = 0.015\,\mu$m. Clearly, light ions penetrate deeper and scatter more.

### B. Effects of incident ions on the substrate

Above, we discussed how an ion loses energy and imbeds itself in the substrate. In addition the ion produces other changes in the substrate. These are illustrated in Fig. 2.

(1) Radiation damage results from the displacement of atoms from their lattice sites due to collisions with the ions. The cumulative effect is that after implantation of a dose of $10^{14}$ $As^+$ ions/cm$^2$ an amorphous layer is formed. Light ions such as $B^+$ do not form amorphous layers (Ref. 30, p. 112). The depth distribution of the damage follows approximately the distribution of the implanted ions.

(2) Sputtering is the removal of atoms from the substrate due to the incident ions. This occurs (and is widely used) at low energies 50–1000 eV. The yield, i.e., number of atoms removed per incident ion, increases with energy up to about 100 keV and then begins to decrease. Typical yields are 1 to 10 atoms/ion. The sputtered atoms leave the surface with a

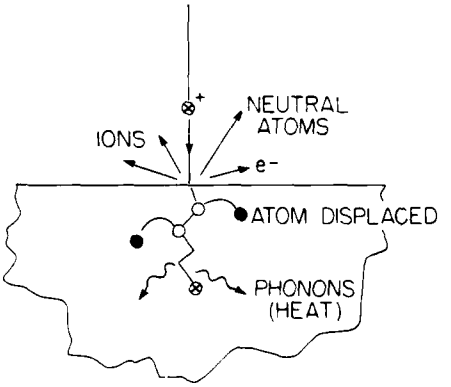


FIG. 2. Schematic of an ion penetrating surface, sputtering off neutral atoms and ionized substrate atoms, causing electron emission, displacement of atoms in solid (damage), and emission of phonons (heat). (Chemical changes are hard to show pictorially.)

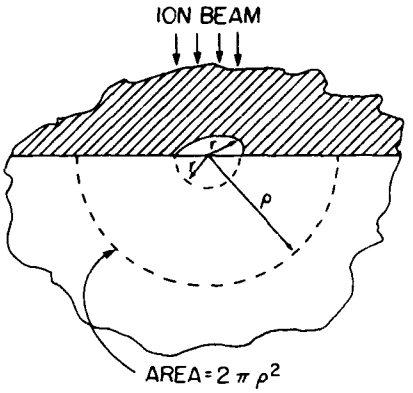


FIG. 3. Geometry for considering heat flow at point of ion beam incidence. Ion beam has radius $r$. In spherical coordinates $\rho$ is the radius from the center of the beam on the surface.

few eV of energy. As will be seen below sputtering with a focused ion beam has numerous applications.

(3) Electrons are also emitted when an ion strikes the surface. Again about 1–10 electrons are emitted per ion with typical energies of a few eV.

(4) Chemical effects produced by ions can be due to ion–electron interaction, as well as the ion–atom interaction which is also responsible for damage. An example of chemical effect in the bulk of a solid is the exposure of resist for ion lithography. Here, the ion changes the molecules of a (usually organic) solid to make it either soluble or insoluble in the developer. Examples of surface chemical effects are ion assisted etching and ion induced deposition due to the breakup of molecules of an adsorbed gas.

The above phenomena are common to all types of ion bombardment of solids. Heating, however, because of the small dimensions and high current densities is special for the focused ion beams and will be examined in more detail.

### C. Heating due to the focused ion beam

A 150-kV beam at 1 A/cm$^2$ current density implies a heat input of 150 kW/cm$^2$. However, one is dealing with $\sim 10^{-10}$ cm$^2$ for typical beam sizes. The heat flow can be modeled in a simple way, and the temperature rise under the beam can be estimated. Consider a uniform beam or radius $r$ incident on a semi-infinite solid, as shown in Fig. 3. A spherical coordinate system is centered at the point of impact with radial coordinate $\rho$. Neglect radiative (or other) heat loss from the surface. For a beam of voltage $V$ and current density $J$ the total input power is $VJ\pi r^2$. The thermal energy current flowing out of a hemisphere of radius $\rho$ into the semi-infinite solid is

$$Q = -K 2\pi\rho^2 \frac{dT}{d\rho}, \tag{1}$$

where $K$ is the thermal conductivity and $T$ is the temperature. If we equate this to the input power and integrate, we get for the temperature rise above the background at a radius $\rho$

$$T(\rho) - T(\infty) = (VJ/2K)(r^2/\rho), \quad \text{for } \rho \geqslant r. \tag{2}$$

Consider the radius $\rho = r$, i.e., the point where Eq. (2) predicts the highest temperature, then for $V = 150$ kV, $J = 1$ A/cm$^2$, $r = 0.05\,\mu$m, and taking the thermal conductivity of $SiO_2$ $K = 1.5 \times 10^{-2}$ W/cm °C, the temperature rise $T(r) - T(\infty)$ is 25 °C. This is for most purposes negligible. However, for larger beams, say $r = 0.3\,\mu$m, and a current density of 10 A/cm$^2$, which has been reported, the temperature rise $T(r) - T(\infty) = 1500$ °C, which is not at all negligible. The case considered here of $SiO_2$ is a worst case since, for example, the thermal conductivity of Si is 100× larger, and so the temperature rise expected would be 100× smaller.

Above we have considered the thermal conductivity with a microscopic model, though at macroscopic dimensions. By looking even more microscopically at the temperature rise due to an individual ion one encounters the phenomenon of thermal spikes. In the immediate vicinity of an ion's path into a crystal, the atoms are severely disturbed and may have a temperature of several thousand degrees.[33,34] Such thermal spikes relax in $10^{-10}$ to $10^{-11}$ s. They are thought to play a role in sputtering, crystallographic changes, chemical changes, and surface diffusion. However, whether the concept of temperature is useful and valid in this extreme circumstance is open to debate.[34]

## III. FOCUSED ION BEAM MACHINERY

A focused ion beam system can be thought of as composed of three main parts: the source of ions, the ion optics column, and the sample displacement table [see Fig. 4(a)]. A detailed understanding of these parts is too intricate for the scope of this review. Instead the principles of operation will be described and the current best performance and the potential improvements will be discussed.

### A. Source

The generation, deflection, and focusing of ions has close analogies in optics. Thus, to illuminate a small spot with a large flux a "bright" source of ions is needed with one or more "lenses" between the source and the spot. As mentioned in the Introduction, the early focused ion beam fabrication work used an implanter with a gaseous ion source.[1] Such a source emits ions from a relatively large area (several mm) and with considerable angular spread. The desired source would emit ions from a single point, preferably into a limited solid angle (or be larger but well-collimated, like a laser). The liquid metal field ionization source[8,9] and the gaseous field ionization source[2–7,35,36] approach this ideal. Table I (adapted from Ref. 37) compares the properties of three types of ion sources. The performance of a source is measured by its brightness, defined as

$$B = (I_s/A_s\Omega_s)\,(\text{A/cm}^2\,\text{sr}),$$

where $I_s$ is the current emitted by an area $A_s$ of the source into a solid angle $\Omega_s$. The solid angle into which a source emits ions is changed if a voltage $V_s$ exists between the source and the point of measurement. This is almost always the case, and the specific brightness $\beta = B/V_s$ is a more appropriate parameter. Nevertheless, the brightness $B$ is most often quoted. An excellent review of this and other points on sources and columns is found in Ref. 14.

Liquid metal field ionization sources are used on almost

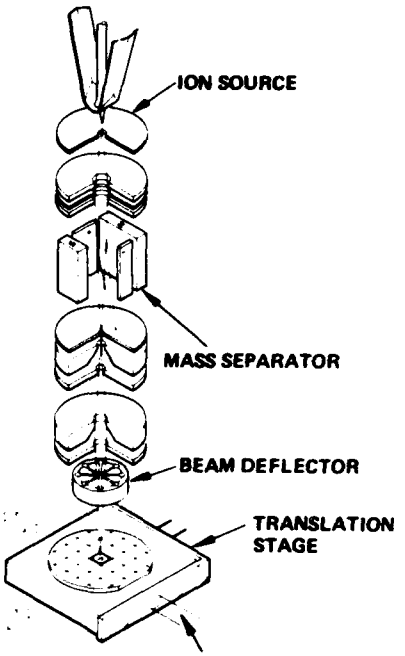


(a)

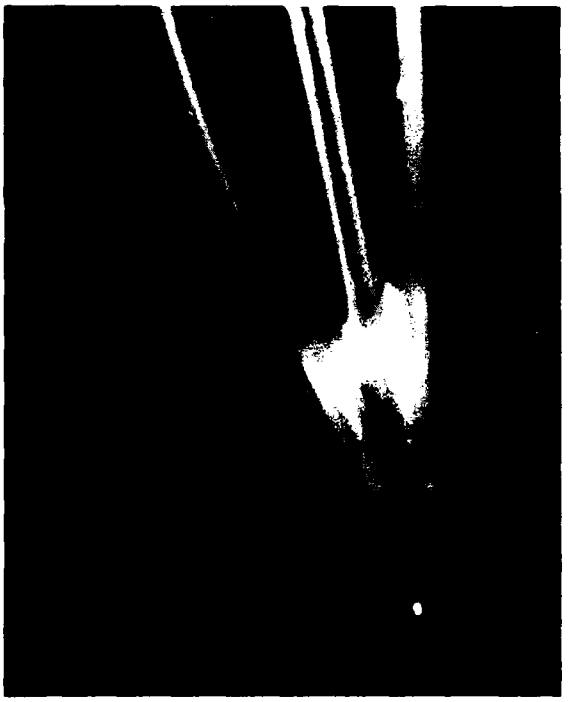

(b)

FIG. 4. (a) Schematic of a focused ion beam system including source, column, and sample stage (from Ref. 71). The series of concentric electrodes between the source and the mass separator and between the mass separator and the beam deflector are the electrostatic lenses. (b) Photo of liquid metal ion source operating in a test fixture (from Ion Beam Systems). The liquid gallium is held by surface tension between the U-shaped heater ribbon and the shank of the needle, which is 0.27-$\mu$m diameter. Some light is also seen to be emitted from the tip of the needle.

all of the focused ion beam systems now in operation and have been studied in some detail. In these sources a reservoir of liquid metal is maintained at one end of a sharp (usually tungsten) needle, see Fig. 4 (b). The metal wets the needle

TABLE I. Ion sources for focused beams.

| | Duoplasmatron | Field ion | Liquid metal |
|---|---|---|---|
| Brightness | $10^2$ A/cm$^2$ sr | $10^9$ | $10^6$ |
| Source size | 50 $\mu$m | 10 Å | 300 Å |
| Energy spread | 4 eV | 1 eV | 5–10 eV |
| Species | $Ar^+$ and others | $H_2^+$, $He^+$ | Ga, Au, Be, Si, Pd, B, P, As, Ni, Sb,..., |

and flows down to the tip. The tip of the needle faces an extraction aperture, a round washerlike electrode concentric with the tip and some distance below it. A voltage is applied between the tip and the aperture. The electric field is highest at the tip, and the sharper the tip, the higher the field. Also, the electric field exerts a stress on a metal surface, which in this case is liquid and can be displaced. As a result the liquid metal is pulled into a sharp cone and the ions are emitted from the tip of this cone. The radius of the tip has been measured to be less than 100 Å.[38] One might reason that there is instability, and the tip radius should decrease without limit; since the higher the field, the sharper the tip, and the sharper the tip the higher the field. However, the sharper the tip the higher the emission, and eventually space charge is thought to limit the current.[39,40] An alternate explanation invokes the hydrodynamics of liquid metal flow down the needle. This limits the current and determines the $I$–$V$ characteristics of the source. The fact that the emission current is strongly dependent on the needle radius and on whether the needle is smooth or has grooves[41] argues for this explanation over the space charge. For capillary-type sources, experiment and theory based on space charge seem to agree.[40] Whether space charge or flow limits the current in needle-type sources, the configuration appears to be stable over time, and a number of liquid metal sources can operate for 100 h or more.

The liquid metal can be of any composition as long it wets the needle, does not corrode it, and has a low vapor pressure in the molten state. The list of elements that have been incorporated into ion sources is quite extensive. Some of the sources with identifiable practical applications are listed in Table II. The most commonly used ion is gallium since it is liquid almost at room temperature and yields a long lifetime source. As will be discussed below the alloy sources such as Au/Be/Si or Pd/As/B need to be used in conjuction with a mass separator in the column. The current available in a given desired species is generally lower than in an elemental source such as Ga. For a detailed review of sources and source operating requirements, see Ref. 42.

The stability of the source current in operation is generally good (say $\pm$ 2%) on a scale of minutes. On a longer time scale some drift is observed. The current is a steep function of the extraction voltage,[56,57] and in practice the extraction voltage is adjusted from time to time. An intermediate extraction electrode can be constructed which is connected to a servo system to stabilize the current yet leave the overall extraction voltage unchanged. If the extraction voltage is changed, in most systems this means that the energy of the

TABLE II. Partial list of technologically important sources.

| Composition | Angular current density ($\mu$A/sr) | Current on sample in system (pA) | Current density on sample (A/cm$^2$) | Lifetime (h) | References |
|---|---|---|---|---|---|
| Ga | 26 | 1000 | 10 | 200 | 10, 43, 44 |
| $Au_{65}Si_{27}Be_8$ | | | | | |
| $Au_{59}Si_{26}Be_{15}$ | 20 $Be^{++}$ | | | 100 | 45, 46, 47, 48 |
| $Pd_{50}Ni_{26}$ | ... | | | | 49 |
| $Si_5Be_6B_{13}$ | | 134 $Be^{++}$<br>66 $Be^{+}$<br>150 $B^{+}$<br>200 $Si^{++}$ | | | |
| $Pd_2As$ | 5 $As^{++}$ | 30 pA $As^{++}$ | | 150 | 50 |
| $Pd_{70}As_{16}B_{14}$ | 1 $B^{+}$<br>3 $As^{+}$<br>4 $As^{++}$ | | | 150 | 50 |
| $Ni_{45}B_{45}Si_{10}$ | | (25%–35% $B^{+}$)<br>2000(at 100 $\mu$A total source) | | 250 | 51, 53 |
| $Pd_{64}As_{11}$<br>$B_9P_{16}$ | ... | (18 atm. % $P^{+}$) | | 25 | 50 |
| Cu-P | | (10 atm. % $P^{+}$) | | 20 | 52 |
| Al | 20–30 | | | 100 | 54 |
| Au | (1 to 100 $\mu$A total current) | | | 50 | 55 |

ions entering the column below is changed, and all of the lens voltages may need to be adjusted to maintain beam focus. The servo and extra electrode get around this problem. Another method to obtain precise doses of ions is simply to measure the beam current frequently and adjust the dwell time accordingly. This method has been automated.[48]

There are indications that the point of emission of the source can fluctuate.[58] In favorable circumstances this can be controlled so that the total fluctuation of the position of the spot focused on the sample is below 0.1 $\mu$m. The point of emission of the source also appears to move with changes in extraction voltage.[58] For a given source this is measurable and predictable, and must be kept in mind in the operation of any source servo system. Sharper source needle tips appear to lessen the fluctuation effects.[58]

The limits of the liquid metal field ionization source performance are largely determined by the electrostatic repulsion of the ions. Even though the diameter of the tip of the cone is about 100 Å, the emission appears to be taking place from a "virtual source" of 500- to 1000-Å diameter.[59] The origin of this increase in effective size is due to the mutual repulsion of the ions and has been modeled in detail by Monte Carlo methods.[59] An ion leaving the tip is accelerated by the applied electric field. In addition it experiences an electric field due to the other ions nearby. However, this electric field is random because of the statistical fluctuation in the number and location of the neighboring ions. Thus, the ions which enter the column will have a small random velocity in addition to the velocity produced by the applied extraction potential. The component of this random velocity normal to the axis of the system results in the increased virtual source size while the component along the axis just adds to or subtracts from the desired velocity. This latter effect results in a spread $\Delta E$ full width at half-maximum (FWHM) in the energy of the ions, $E$, which finally arrive at the sample. As will be discussed below this energy spread results in chromatic aberration.

The magnitude of the random velocity can be reduced by reducing the current since in the limit where the ions are emitted one at a time, far apart, the effect would be absent. The current dependence of the energy spread $\Delta E$ has been measured for a number of ions: Ga (Refs. 60–63), Si (Refs. 46 and 60) (from an alloy source), as well as Au, Al, In, and Bi (Ref. 60). Generally, $\Delta E$ is higher for heavier ions. Thus at 10 $\mu$A, total source current (a typical operating range) $\Delta E = 10$, 15, 24 eV for $Al^{+}$, $Ga^{+}$. $Au^{+}$, respectively.[60]

The distribution of energies tends to follow a Gaussian-type curve (which in some cases is asymmetrical). The width of the distributions (FWHM) varies from 5 to 25 eV as the current is varied from 0.5 to 25 $\mu$A (Ref. 61). At high and low currents the widths of the distributions appear to saturate.[46] The current of the source cannot be lowered below 0.5 to 1 $\mu$A because the source becomes unstable. The performance of liquid metal ion sources appears to be limited by fundamental considerations. We cannot at this time identify developments which might lead to radical improvements in performance.

The gaseous field ion source is similar to the liquid metal ion source but operates near liquid-helium temperatures and condenses either hydrogen[35] or helium[36] from a gas ambient (see also earlier work, Refs. 2–7). The emission occurs from a facet on a single-crystal tungsten needle. The facet is, in effect, a point of atomic dimensions. Very high brightness has been observed (Table I). This source is technologically more difficult to operate and is still in the research stage, although preliminary results have been obtained.[35] The primary interest in getting low atomic weight ions is in exposure of resist for lithography as will be discussed below.

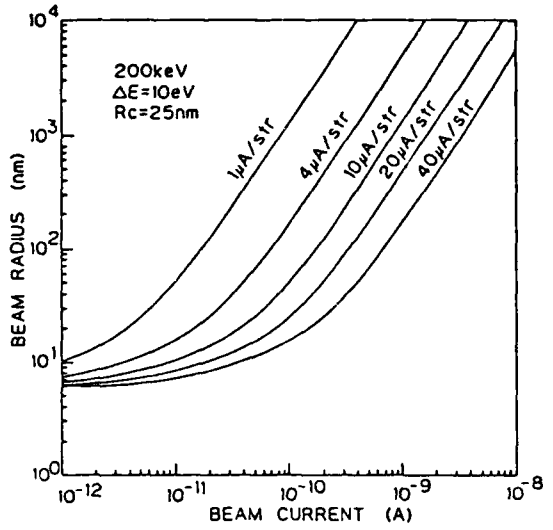


FIG. 5. The calculated beam radius at the sample vs beam current for various source angular current densities. The beam current is proportional to the product of the beam angle $\alpha$ squared and the angular current density (from Ref. 69).

## B. Column

### 1. Ion column

The column which focuses ions from the source onto the sample is very much analogous to a series of optical lenses which may focus a source of light in one plane onto another plane. Thus one speaks of ion optics or of ion lenses. (For a more detailed review of this area, see Ref. 14.)

In electron microscopes and electron beam (e-beam) lithography machines the lenses often use magnetic fields to bend the paths of electrons. For ions this is not usually practical. The higher fields needed would be difficult to generate, since the ions are more massive and travel more slowly. Ion lenses are for the most part electrostatic and consist of two (or more) very precisely machined washer-shaped electrodes at some high potentials. A schematic of a column is shown in Fig. 4. The beam passes through the center of these concentric electrodes and is deflected and accelerated by the electric fields. Since the structure and fields are cylindrically symmetric about the axis of the beam, and since the deflection of the beam by the electric field is proportional to the distance from the axis, the lenslike operation results.

One of the properties which limits the operation of a simple optical lens is chromatic aberration, i.e., the lens has a different focal length for different wavelengths of light. Similarly, an electrostatic lens has a focal length which depends on the energy of the ions. The most serious practical limitation to the performance of most present focused ion beam columns is this chromatic aberration. The chromatic aberration would cause an otherwise zero diameter beam to have a diameter $d_c$ given by

$$d_c = C_c \alpha (\Delta E / E), \tag{3}$$

where $C_c$ is the chromatic aberration coefficient, $\alpha$ is the half-angle of the beam arriving at the final focal spot, $\Delta E$ is the energy spread, and $E$ the total energy. (This expression refers to the sample or exit side of a lens. A similar expression can be written for the source side.[14]) The spread in energy of the ions appears to be a fundamental property of the field emission source. The origin of this spread is the statistical nature of the ion emission and the mutual electrostatic repulsion, as discussed above.

Spherical aberration is another effect which may increase the beam diameter. It arises from the nonideal radial dependence of the focusing fields of a lens, i.e., the focal length of the lens depends on how far an ion trajectory is off axis. The contribution to beam diameter from spherical aberration is given by

$$d_s = (1/2) C_s \alpha^3, \tag{4}$$

where $C_s$ is the spherical aberration coefficient. Since the spherical aberration is cubic in angle, it is usually negligible for the milliradian angles typically used.

Equations (3) and (4) hold for individual lenses or for combinations of lenses, provided that the coefficients are correctly added (see Ref. 64). The values of the aberration coefficients $C_s$ and $C_c$ are obtained by a computer calculation of the fields and ion trajectories in a lens system.[65–67]

The other important effect which contributes to the finite beam diameter is the virtual source diameter $d_0$ as discussed above. Thus the total diameter of the beam spot at the exit of the column is given by

$$d = (d_0^2 M^2 + d_c^2 + d_s^2)^{1/2}, \tag{5}$$

where $M$ is the magnification of the lens system, $d_c$ and $d_s$, depend on the beam acceptance half-angle $\alpha$ and can be reduced at the expense of total current. (This is done in practice by reducing the beam defining aperture below the sources.) The current density remains constant. The virtual source diameter term is the limiting value of the beam diameter that can be achieved as $\alpha$ is reduced. Generally for $\alpha < 1$ mrad the $d_0 M$ term dominates.[68] Another way to reduce the chromatic aberration is to increase the beam energy $E$ since it appears in the denominator of Eq. (3). Thus in a 200-kV system the observed beam diameter is 0.08 $\mu$m.[69]

The beam radius as a function of beam current and beam energy calculated for the 200-kV machine is shown in Figs. 5 and 6. This calculation is machine specific, and the details are not published. The general trends, however, follow the behavior discussed in a very simplified form above in Eq. (5). The beam current is proportional to $\alpha^2$ and the source angular current density (used as parameter in Fig. 5). The saturation at low beam current is presumably due to virtual source size as predicted by Eq. (5).

### 2. Mass separator

Low melting point metals such as Ga, In, or Sn can be liquified in a source as discussed above. Other desired species such as Si, Be, B, or As are incorporated into alloys which can operate in a liquid metal ion source. However, in such instances several species of ions are all emitted by the source. Mass separators using crossed electric and magnetic fields ($E \times B$) (Refs. 11 and 70) as well as sequential opposite magnetic field deflectors[71] have been developed.

The principle of operation of the ($E \times B$) mass filter is

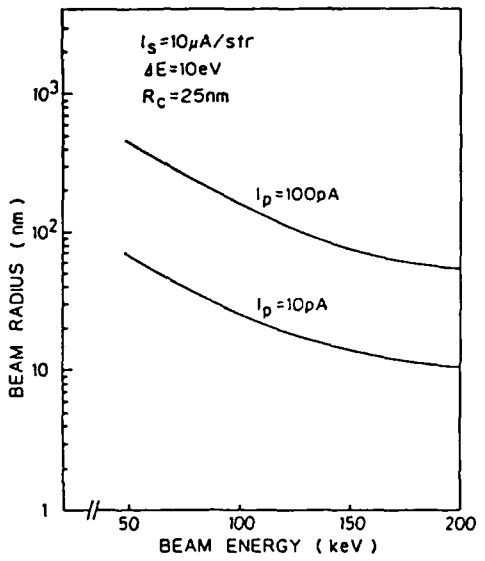


FIG. 6. Beam radius calculated as a function of beam energy (from Ref. 69).

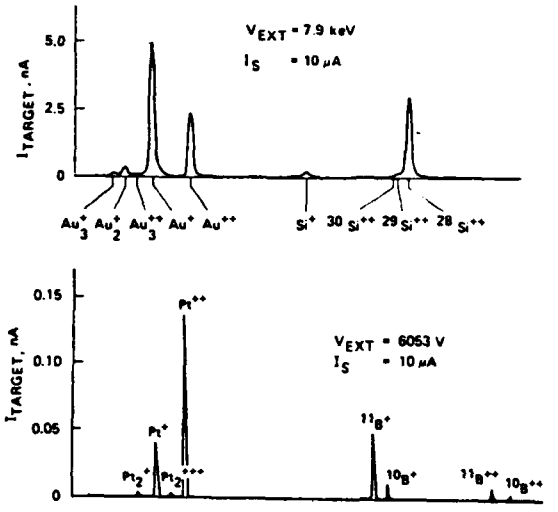


FIG. 8. Mass spectra of Si–Au source top and Pt–B bottom. The extraction voltages and total source currents are in the inset of each curve. The plots are obtained by sweeping either $B$ or $E$ in the ($EB$) filter and measuring the current passing through the aperture, Fig. 7 (from Ref. 11).

shown in Fig. 7. Strictly speaking it is a velocity filter, but, since all ions arriving at the filter have been accelerated through the same potential, ions of different mass or charge will have different velocities. The condition for passing through the filter undeflected is

$$E = vB, \tag{6}$$

where $E$ is the electric field, $B$ the magnetic field, and $v$ the velocity (mks units). The velocity of an ion of mass $m$ and charge $q$ accelerated by a potential $V$ is $v = (2qV/m)^{1/2}$. Thus the ions will pass through the filter if

$$\sqrt{2qV/m} = E/B. \tag{7}$$

In practice one can run a spectrum of the ions in a beam by sweeping either $E$ or $B$ and measuring the current in a Faraday cup below the mass separation aperture. A sample spectrum is shown in Fig. 8. The resolution of the filter depends on the geometry, i.e., the length of the filter $L$, the distance to the mass separation aperture $D$, the diameter of the mass separation aperture, and the diameter of the ion beam at the mass separation aperture (see Fig. 9). For small deflections we can assume the force due to the magnetic field remains

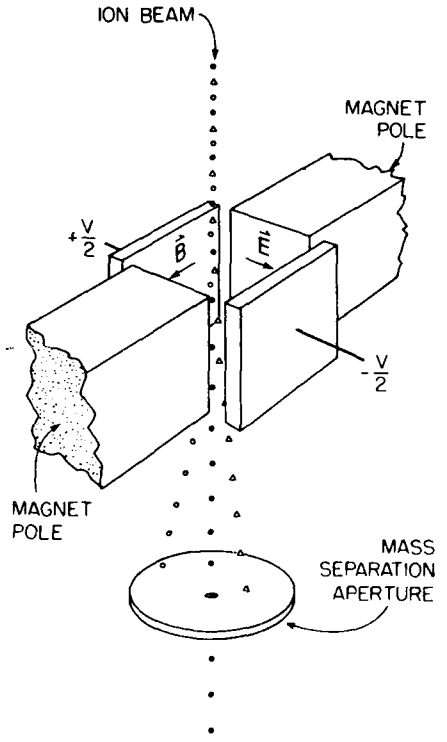


FIG. 7. Schematic of mass separator with a beam of three species of ions (represented as solid and open circles and triangles).

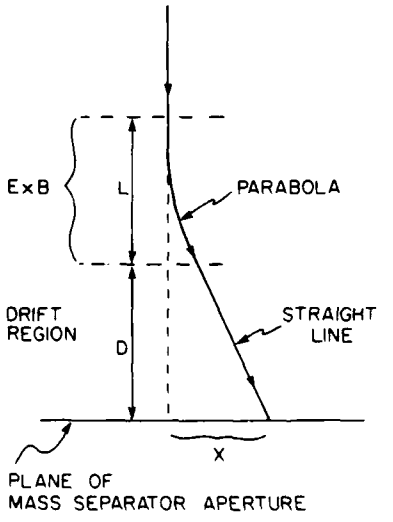


FIG. 9. Path of the ions through the $EB$ mass separator shown in Fig. 7 and the field-free drift region to the mass separation aperture.

collinear with the force due to the electric field. Then the deflection is

$$x = (L^2/2 + LD)(1/2V)[E - B\sqrt{2qV/m}]. \quad (8)$$

Differentiating this expression [Eq. (8)] with respect to $m$ and substituting the condition [Eq. (7)] above (since we are interested in the resolution at the point of no deflection) we get

$$\Delta x = -(L^2/2 + LD)(E/2V)(\Delta m/m). \quad (9)$$

Some typical numbers are $L = D = 3$ cm, $E = 80\,V$/cm, and $V = 10^4$ V. This yields

$$\Delta x = 270\,\mu\text{m}(\Delta m/m). \quad (10)$$

Note that for the above electric field and acceleration voltage the magnetic field $B$ is $1.22\times10^{-2}$ web/m$^2$ (122 G) for $Be^{++}$ ions, and $4.82\times10^{-2}$ web/m$^2$ (482 G) for $Ga^+$ ions. If mass separation capability needs to be maximized, then higher $E$ and $B$ fields can be used. For example, a 1600 G magnetic field has been reported.[11] For $Ga^+$ ions this corresponds to $\Delta x = 896\,\mu$m $(\Delta m/m)$. To maximize the mass resolution capability $(\Delta m/m)$ one would locate a beam crossover (focal plane) at the position of the mass separation aperture. A beam diameter at this focal plane of 5 $\mu$m has been reported.[11] Thus, if a 5-$\mu$m-diam aperture were used, the mass resolution could be $\Delta m/m = 0.006$. The isotopes of most elements could, therefore, be separated. In practice this much resolution is not needed and is, in general, obtained at the expense of other performance characteristics.

The $E\times B$ mass separator may introduce distortions into the focused ion beam in several ways:

(1) Nonaxis symmetric focusing.[72] A beam of circular cross section entering the $E\times B$ filter will emerge elliptical even though the fields are such that it is undeflected. This effect arises because along the axis of the $E$ field the potential varies approximately linearly. If we assume the center of the filter to be at the potential of the beam, i.e., ions on axis are neither accelerated nor decelerated when they approach the filter, then the ions which have been accelerated to a potential $V$ will be slightly decelerated on one side of the axis and accelerated on the other side. Thus, those ions will go through at different velocities and will be bent toward the axis by the magnetic field.[72]

(2) Variation in ion energy will translate into a variation in the amount of deflection by the $E\times B$ (velocity) filter. If the variation in energy of ions from the source is say 15 eV, then the numbers chosen above a point beam of $Ga^+$ ions would be elongated at the mass separation aperture by 0.27 $\mu$m. The effect on final spot size would be reduced by the demagnification.

(3) The fringing fields (both $E$ and $B$) will cause distortions if the beam is off center in the $E\times B$ or if it is of finite diameter. The $E$ and $B$ fields are perpendicular and have zero gradient in general only on the axis of the $E\times B$ filter. Thus any ions off axis will be deflected from the expected paths.

In practice, all of these distortions are minimized by operating with as low-field values as possible, and by careful alignment so that the beam is on axis. In addition, the effects (1) and (3) can be minimized by having the beam crossover in the center of the $E\times B$ rather than at the mass separation aperture.[43,70] Again, this sacrifices mass resolution to minimize distortion.

While the presence of an $E\times B$ mass separation filter does degrade the beam focus, in practice beam diameters of 0.08 $\mu$m have been reported with mass separation.[69]

An alternate mass separator filter has been implemented at Cambridge University. It uses four magnets to deflect the beam into a parallel offset path where a mass separation aperture is located and then back to the beam path.[71] It has the advantage that there is no line of sight from the source to the sample. Thus energetic neutrals, droplets, or other particles emitted by the source cannot reach the sample. In addition, the shift due to variation of the initial ion energy discussed above (2) is canceled. At this point not enough is known to judge whether the $E\times B$ or the four-magnet mass separator produces better results. Both types of systems have yielded submicrometer diameter beams.

Note that the earth's magnetic field may in some instances cause non-negligible effects, for example, in separation of isotopes. The earth's magnetic field is about $2.5\times10^{-5}$ web/m$^2$. Thus in a Ga ion beam of 10 keV energy traveling 10 cm in this field the $Ga^{69}$ and $Ga^{70}$ isotopes would be separated by 30 nm.

### 3. Beam blanking and deflection

A focused ion beam which is to be used for beam writing over selected areas needs a beam blanker, i.e., a means of turning the beam off. This is generally done by having a pair of electrodes on opposite sides of the beam and applying a voltage $-V_d/2$ and $+V_d/2$ to them so that the beam is deflected sideways and is not capable of passing through an aperture located downstream. If the beam writing is to be done at high speeds so that the beam is switched on at a given pixel for only 10–1000 ns, then the blanker must turn the beam on at an even higher rate. The sharpness with which the beam can be cut off and turned on is determined by the amount of time the ion needs to spend in the field to achieve the necessary deflection, by the abruptness of the electric field (i.e., amount of fringing), by the rise and fall time of the electrical pulse applied to the plates and by the magnitude of deflection needed. This is illustrated in Fig. 10. As seen in the figure, the blanking produces a slight "smearing" or tail on the end and beginning of a pulse of ions. The blanker should be optimized so that the number of ions in these tails is negligible compared to the number in the desired pulse.

The angle of deflection needed (typically $\sim$0.5 mrad) to turn off the beam is the ratio of the transverse velocity $v_x$ of the ions imparted by the deflector to the velocity along the beam axis $v_z$. How the rise time of the blanking pulse and the spatial fringing of the electric field contribute to the tails can be calculated.[73] Note that even if both the pulse and the field profile are ideal square waves, a tail will still be present due to the fact that the ion must spend a finite time in the blanker before it acquires the needed transverse velocity $v_x$ to be cut off. Some typical numbers are field of 20 V/mm, $v_z = 1.66\times10^5$ m/s (corresponding to $Ga^+$ at 10 keV) then to deflect the beam by 0.5 mrad it needs to spend at least 3 ns in the blanker before the needed deflection is produced. This

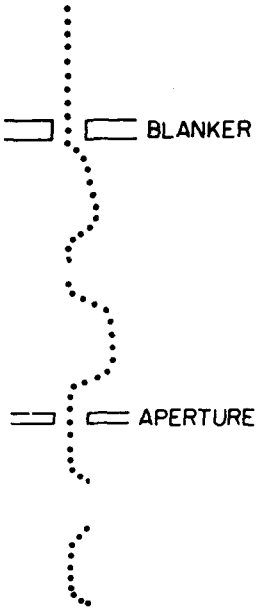


FIG. 10. A schematic of the operation of a blanker and the downstream aperture illustrating the origin of the tails due to beam chopping.

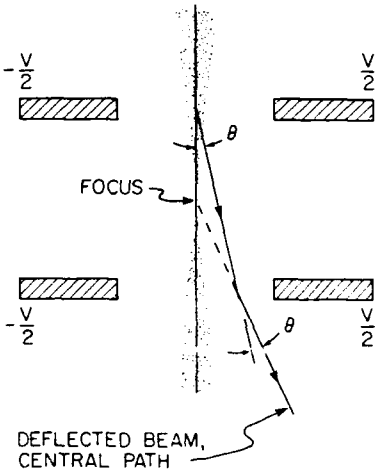


FIG. 11. Schematic of dual blanker scheme used to eliminate spatial beam tailing during blanking.

determines the minimum length of the tails in Fig. 10. Pulse rise times and fringing fields will further lengthen the tails.

The pulse tailing due to the blanking is minimized by having the aperture which stops the unwanted beam at a focal point. The beam there has a minimum diameter, and the angle of deflection $\theta$ needed to switch off the beam is minimized.

Another scheme which can, to first order, eliminate *spatial* pulse tailing, such as would occur when the clusters of ions in Fig. 10 are incident on the sample, uses two sets of blanking plates with a beam crossover (intermediate focus) at the symmetry point between them.[66,74] Then if the same polarity is applied to the two sets of plates (a delay time may be built in to account for the transit time), the beam focus appears not to move when the deflected ion paths are projected straight back through the deflector (see Fig. 11). Thus the final focal spot on the sample will not move as the beam is blanked off. It will of course still "fade out" in time.

To accomplish beam writing of arbitrary patterns the blanker is used in conjunction with a deflection system. One strategy is to specify the pattern by trapezoids.[75] A combined vector/raster scan approach can be used. A blanked-off beam is first deflected to a given trapezoid corner. Then it is turned on and the trapezoid is "filled in" by a raster scan. If a very light dose, say $6\times10^{11}$ ions/cm$^2$, is needed, for example, for resist exposure or channel doping, then for a typical beam current density of $6\times10^{18}$ ions/cm$^2$ s (1 A/cm$^2$) the dwell time per pixel is $10^{-7}$ s. Thus the first and last pixel of a trapezoid may have small tails on them where the dose is 10%–25% of the desired level due to the nonabrupt blanking. In most practical situations this is probably not serious, but nevertheless should not be ignored.

The beam blanking and beam deflection, in general, do not occur at the same point in the column. Thus their operation has to be synchronized to take into account the finite transit time of the ions between them.

The beam deflector has been abundantly analyzed and developed in connection with e-beam lithography.[76–78] The main issues are writing accuracy and focal spot distortion as a function of deflection. Electrostatic deflectors are usually octopoles so that one has more control over the field parameters. The distortions are often of either the "pincushion" or "barrel" type, i.e., if one specifies that a square be written, say, surrounding the scan field, its sides may either be concave (pincushion) or convex (barrel). In the corners of the field the beam spot which is circular in the center of the field may become elliptical.[67] Both of these effects grow rapidly as the field size is increased. Thus a small field is desirable.

### 4. Beam profile

The ultimate resolution of any patterning done with focused ion beams will depend on the beam profile. The cur-

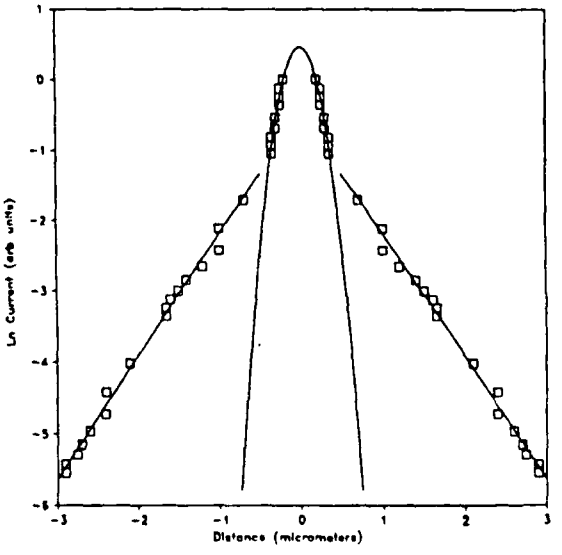


FIG. 12. Plot of natural log of the current vs distance from the center of the beam. The squares are measured data, the center curve is the Gaussian fit (FWHM = 0.5 $\mu$m) and the lines are fits to the exponential tails (from Ref. 79).

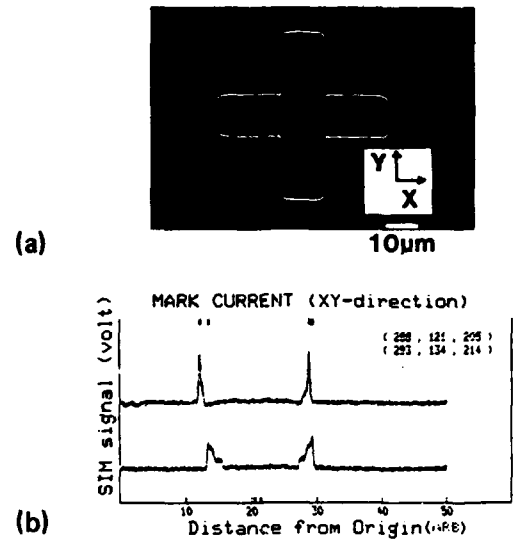


FIG. 13. (a) A cross etched into the surface of GaAs 1.5-$\mu$m deep used as an alignment mark, covered by 1-$\mu$m-thick MBE layer, viewed in a scanning ion microscope. (b) The derivative of the secondary electron current measured by scanning across the areas of the cross (from Ref. 48).

rent density in the ion beam spot focused on a sample is thought to have a Gaussian profile. However, detailed measurements have shown that about 2–3 orders of magnitude below the peak the beam profile deviates from a Gaussian and shows wider skirts (Fig. 12). This has been observed both for simple nonmass-separated, single-lens columns,[79,80] and for the mass separated three lens columns.[81,82]

The effect has been simulated[80] by assuming a nonlaminar distribution of emitted ions from the source. Thus these beam skirts would appear to originate in the ion source. How these skirts might be reduced by different column configurations or by apertures placed in the ion column has not been studied. Also, since the nonlaminar flow of ions from the source is presumably due to the transverse random velocity component of ions produced by their mutual repulsion (discussed above), the magnitude of the skirts should depend on total source extraction current in much the same way as the energy spread depends on extraction current.[59,62]

In practice the skirts in the beam profile must be taken into account if one wants to expose one area to a high dose immediately adjacent to another area which is to have a low dose.

## 5. The sample stage

We have discussed the main elements which make up an ion column. This column can focus a beam down to a 0.1-$\mu$m spot or less and deflect this spot accurately and rapidly over a field typically 100–500 $\mu$m in width and height. If we wish to address a larger sample (say, 5-in. diameter), a stage is needed to position the sample precisely under the beam while maintaining it in the focal plane. (Since the beam angle is small $\sim$0.5 mrad, the depth of focus can be 50–100 $\mu$m.) This capability has been well-developed for e-beam lithography.[33] The central element is a laser interferometer which measures the position of the stage to an accuracy of 0.01 $\mu$m. The interferometer reflects laser light from two mirrors, one lined up along the $x$ axis, the other along the $y$ axis. These mirrors must have a length equal to the length of travel. Thus the flatness of these mirrors must be better than 0.01 $\mu$m over distances of 15 cm. In addition, they must be aligned to the axis of motion of the stage. The stage is driven on special bearings by computer controlled electric motors. These motors can position the stage to within $\pm 2$ $\mu$m of a desired location. The position achieved can, of course, be measured to 100$\times$ better accuracy with the laser interferometer. The maximum speed of stage is typically 2.5 cm/s.

## 6. Pattern writing and alignment

The aim of the focused ion beam system is to write a pattern on a substrate with a precision of 0.1 $\mu$m or better. For this the stage motion and the beam deflection need to be integrated. This can be done by computer control, in much the same way as in e-beam lithography systems.

If one needs to align to existing features, the scanning ion microscope capability is used. Typically, crosses with well-defined edges are fabricated as alignment marks[48,83] (see Fig. 13). These crosses can be located on the screen visually, or a precise location can be determined by scanning the beam over the arms of the cross under computer control and detecting the electrons emitted. The secondary electron emission for various geometry sidewalls has been studied.[84] The interferometer reads the stage position to an accuracy of $\pm 0.01$ $\mu$m. The error signal between the desired position and the achieved position (usually less than 2 $\mu$m) can be added to the deflection signal automatically.

## 7. Potential improvements in apparatus

The directions of desired improvement are smaller beam diameter, larger current density in the beam, longer source lifetime, and faster operation or higher throughput.

*a. Source.* As discussed above the limiting value of the source diameter is determined by the virtual source size. This is of fundamental origin and at this time except for a new invention we see no radical improvement. Likewise the current density in the beam as well as the beam diameter is limited through the energy spread of the ions emitted by the source. Again this is of fundamental origin.

The source lifetimes are mostly limited by chemistry: reaction of the molten alloy with the needle, or with background gas due to poor vacuum, and change in the composition of the alloy. There has been steady improvement in this aspect of source technology, and it is expected to continue.

The gaseous field ion source is continuing to receive attention as discussed above. This source yields higher brightness and a potentially smaller beam of helium of hydrogen ions is possible. However, this source operates at cryogenic temperatures and is cumbersome. Because of the ion species its primary use would be in resist exposure, i.e., lithography.

*b. Column.* More improvement is to be expected in column operation than in sources. Given that the energy spread of the ions from the source is fundamental one should design lenses in the column with lower chromatic aberration coefficients. One approach is to add more elements to the electrostatic lens and to optimize the placement and potentials on

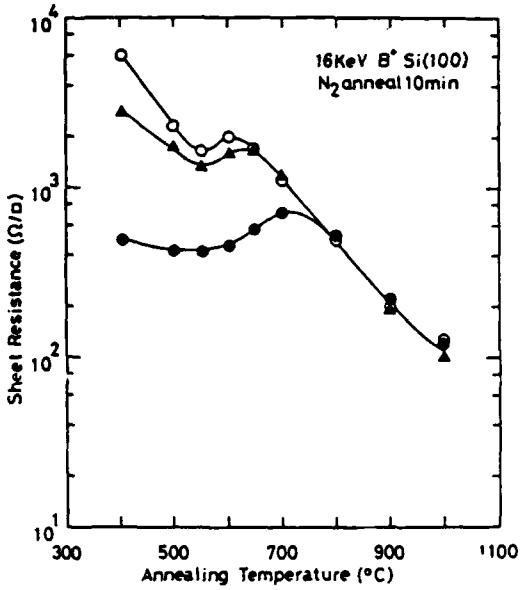


FIG. 14. Annealing of 16 keV $1\times10^{15}$ $B^+$ ions/cm$^2$ implanted into Si. Open circles: conventional implant. Triangles: focused ion beam rapid scan 9 cm/s. Solid circles: focused ion beam slow scan $4\times10^{-2}$ cm/s (from Ref. 93).

these elements to minimize the chromatic aberration coefficient.[44,85] This has been successful in achieving operation with a current density of 10 A/cm$^2$ in the beam spot at the sample.[44]

Another, more radical, approach is to use combined electric and magnetic quadrapole lenses. Such achromatic doublets have been fabricated and tested with a Van de Graaff accelerator.[86] The tests were performed over a very wide range of energies, 450 to 800 keV, and the beam diameter varied from 15 to 25 $\mu$m. With only magnetic focusing the diameter varied by 85 $\mu$m as the energy was varied.[86] When applied to focused ion beams, these achromatic quadrapole doublet lenses are projected[87] to yield beam diameters of 31 nm and current densities of 100 A/cm$^2$. This is a 100-fold improvement in the presently achieved current density. Computer programs for designing multiple lenses have been developed,[88] which have succeeded in predicting the experimentally observed properties of the achromatic doublet.[89] These programs can also be used to analyze a proposed achromatic triplet.[88] The triplet lens has the advantage that the magnification in $x$ and $y$ can be made the same whereas in the doublet they are not. In practice the difference in magnification can also be overcome by using a stigmator.

Another proposed focused ion beam system design aims at achieving ultrafine, 10-nm beams rather than high current density.[89] This system focuses a demagnified image of an intermediate aperture on the target (Koehler illumination) rather than forming the image of the source tip on the target. Sharper, more squared, beam profiles instead of the usual Gaussian may be a potential advantage.

Compared to e-beam lithography, which has had 15 years of intensive development, ion beam writing is in its infancy. At this point we see most potential improvement in current density and beam diameter. If these improvements materialize, then pressure will no doubt build up to improve other aspects of the system such as the writing capability.

Since the focused ion beams have a number of important areas of application, as will be discussed below, we expect that the drive to advance the technology of the machinery will increase.

## IV. APPLICATIONS

That the capability to focus a beam of ions to submicron dimensions has many possible applications was clear from the very beginning. In fact, the earliest work[1] already reported exposure of resist and maskless implantation into semiconductors. This potentially widespread impact has spurred the development of the machinery. The availability of machines has in turn stimulated new applications. The underlying reason for the many applications is that energetic ions interact with surfaces of solids in a number of ways as described above. The applications demonstrated so far can be grouped into six categories according to the physical interaction processes utilized. They are the following: implantation, milling, surface chemistry, lithography or bulk chemistry, microscopy, and materials analysis. We will look at each of these categories in turn.

### A. Implantation

#### *1. General considerations*

The main applications of focused ion beam implantation conceived so far is in the doping of semiconductors. As discussed above alloy sources (see Table II) have been developed which will emit the main dopants of Si and GaAs, such as B, As, Be, and Si. In many of these species both singly and doubly charged ions are emitted. Thus the range of energies available for implantations is doubled.

The attraction of focused ion beam implantation is that it is a maskless resistless process, and, in addition, the dose can be varied from point to point on a wafer. Thus one can make device side by side each with a different dopant dose, and one can vary the doping as a function of position within a given device, e.g., introduce a lateral gradient of carrier density. Because the current density in a focused ion beam is many orders of magnitude higher than the current density in a conventional implanter, one must first establish that implantation of a given dose by a focused ion beam is the same as conventional implantation. Results reported so far indicate that this is largely true. Boron implants into Si and Be implants into GaAs at 70–80 keV have yielded the same Hall mobilities as conventional fabrication.[90] Similarly Si metal-oxide-semiconductor field-effect transistors[91] (MOSFET's) and npn bipolar transistors[92] fabricated by conventional implantation and by focused ion beam implantation programmed to yield the same dose showed the same device characteristics.

On the other hand, if Si is implanted with B and if the electrical activation of the implant is studied as a function of anneal temperature, some differences are observed.[93] In these measurements three types of implants are compared, conventional, rapid, repeated-scan focused ion beam, and slow-scan ($4\times10^{-2}$ cm/s single scan) focused ion beam, see Fig. 14. When annealed above 800 °C all three implants

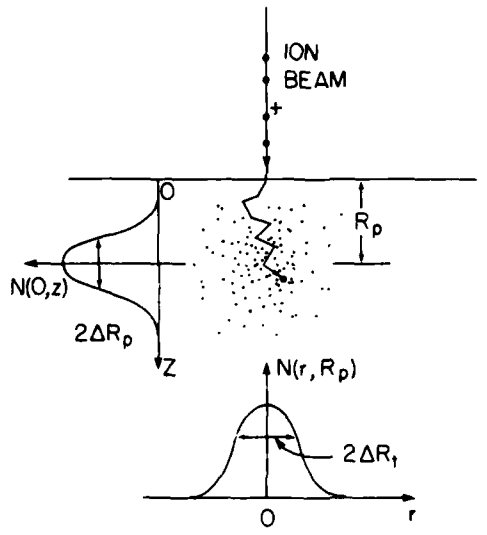


FIG. 15. Shows a large number of ions entering a solid surface at a single point. Due to random processes the ions distribute themselves in the solid in a cloud of density $N(r,z)$ (in cylindrical coordinates with origin at the point of entry). The profiles in both width and depth are modeled as Gaussian. The solid is assumed to be unaltered by the beam, i.e., the last ion scatters the same as the first.

showed the same electrical activation. However, when annealed at temperatures of 400 to 800 °C the slow-scan focused ion beam implant showed a much higher degree of electrical activation than the other two as if some annealing had already taken place. Note that the analysis above indicates that heating of the sample under the Gaussian beam should be negligible. In any case, these results are not inconsistent with the other observations[90–92] since, when the implanted material is annealed for complete electrical activation, no difference is observed between the three cases.

The implantation of Si and Be into GaAs has similarly been studied.[94] The electrical and optical characteristics of conventional and focused ion beam implants are comparable. In some cases the focused ion beam implants showed slightly higher electrical activation efficiency.[94] Thus one is reassured that focused ion beam implants can be substituted for conventional implants.

The degree of spreading of the implanted ions after they have hit the target is important in focused ion beam implantation. For conventional implants this has been modeled as range straggle, i.e., distribution of ions in depth, and as transverse straggle, i.e., distribution of ions parallel to the surface (see Fig. 15). In addition, the implant has to be annealed to remove the damage and to place the impurity atoms on lattice sites where they will contribute charge carriers. Some diffusion will occur to further broaden the distribution. The straggle and diffusion both can be modeled by Gaussians. Thus if the beam has an initial radius $R$ incident along the $z$ axis at the origin of a cylindrical coordinate system then it will produce a distribution in the solid as a function diffusion time $t$ given by

$$N(r,z,t) = \frac{N}{(2\pi)^{3/2}(\Delta R_p^2 + 2Dt)^{1/2}(R^2 + \Delta R_t^2 + 2Dt)} \times \exp\left( -\frac{1}{2}\frac{(z-R_p)^2}{(\Delta R_p^2 + 2Dt)} - \frac{1}{2}\frac{r^2}{(R^2 + \Delta R_t^2 + 2Dt)} \right). \quad (11)$$

In this case $R$ is the radius of the beam at 0.61 if the peak of the Gaussian is at 1. Values of the range $R_p$, range straggle $\Delta R_p$, and transverse straggle $\Delta R_t$ are available in the literature.[31,32] Some sample numbers can be read from Figs. 16 and 17. The diffusion coefficient $D$ is in practice not just dependent on temperature but also concentration, damage, and other effects. However, some approximate constant values are $D = 3\times10^{-14}$ cm$^2$/s for B in Si at $T = 900$ °C (Ref. 31). So for a typical anneal of 30 min $2Dt = 0.1$ $\mu$m which indicates the degree of spreading expected. In rapid thermal annealing the temperature is higher, 1200 °C, and the time shorter, e.g., 10 s. Thus, $D = 10^{-12}$ cm$^2$/s and $2Dt = 0.04$ $\mu$m. This is confirmed in practice as, i.e., rapid thermal anneal minimizes spreading of the dopants.

The expression, Eq. (11), is more than an empirical fit to the observed profile. The Gaussian is, in fact, a solution to the diffusion equation as it applies to the thermal displacement of the dopants and to the random walk (straggle) during implantation.

This model has not been tested thoroughly by experiment except in the $z$ direction. Here, the situation is the same as in conventional large area implantation, and the profiles have been measured abundantly. The Gaussian model of the straggle represented by Eq. (11) (with $t = 0$) and the data of Figs. 16 and 17 are the lowest order fit to the data. The distribution of implants is often skewed and departs from a Gaussian beyond the central peak of the distribution. For example, boron which is lighter than Si preferentially scatters backward while arsenic preferentially scatters forward. With focused ion beams, implantation of Si and Be into GaAs has shown that for doses above $10^{14}$ ions/cm$^2$, the lateral spread observed by chemical staining is higher than expected from the beam diameter and the simple range straggle model.[94]

In any case the distribution of dopants due to straggle or diffusion is a concern whether the pattern on the surface is defined by resist or oxide or by focusing of the ion beam. This concern becomes ever more serious as device dimensions shrink, and as smaller beam diameters become available.

The effective diameter of the beam has also been measured by exposing and developing PMMA and by implanting the channel of a MOSFET with narrow B beam at various dose levels.[81] The implantation is done in a line in the middle of the channel parallel to the current flow direction. Thus the effective channel width is decreased as a function of focused ion beam doping level, and the beam profile can be derived by measuring the threshold voltage. As in the above measurements the implant profile or the PMMA exposure profile is a combination of the beam profile, the straggle during penetration, and for the doping case the diffusion during annealing. As discussed above, these latest results (Fig. 12)

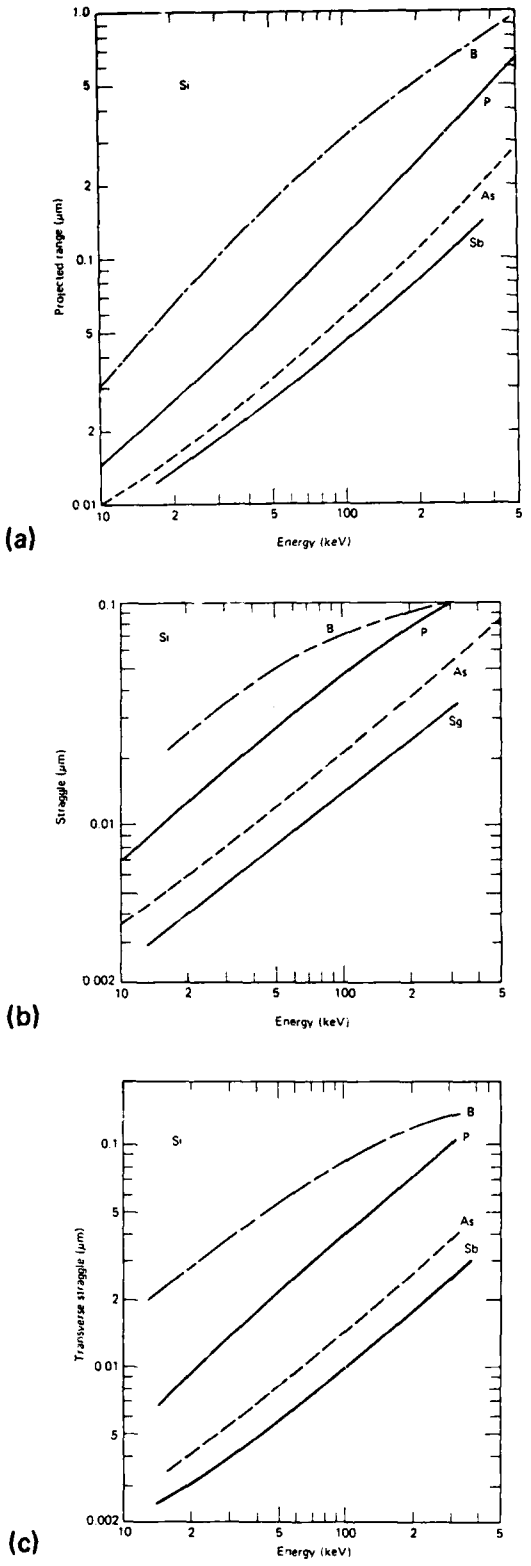


FIG. 16. Plots of (a) range $R_p$; (b) range straggle $\Delta R_p$; (c) transverse straggle $\Delta R_t$ for implantation into silicon (Ref. 32).

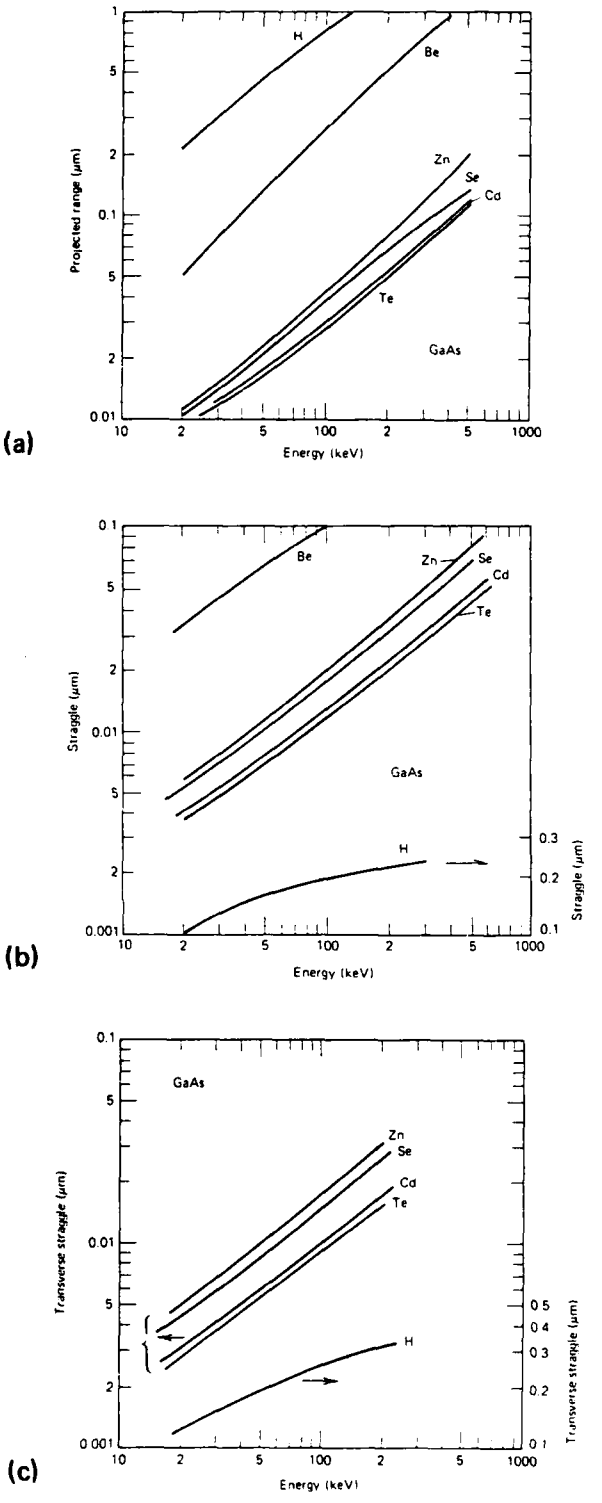


FIG. 17. Plots of (a) range $R_p$; (b) range straggle $\Delta R_p$; (c) transverse straggle $\Delta R_t$ for implantation into GaAs (Ref. 32).

indicate that the beam deviates from a Gaussian shape and has higher shoulders at about two orders of magnitude below the beam center. This is thought to be due largely to the initial beam profile.

The novel capability that focused ion beams provide is the patterning in the plane of the sample during implantation. As has been shown above, the resolution with which this patterning can be done is limited by the beam diameter, by the transverse straggle, and by diffusion during annealing. In most cases if the beam diameter is of order 0.1 $\mu$m the other two effects can be kept at or below the same level.

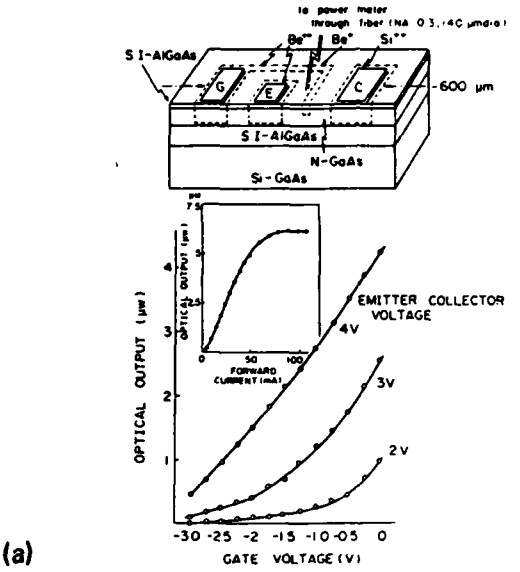


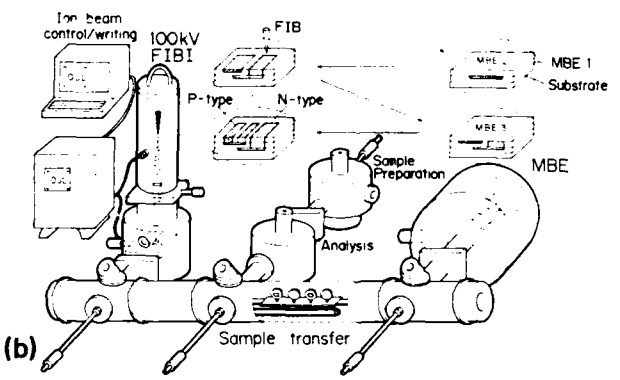


FIG. 18. (a) Junction field effect transistor and light emitting diode fabricated in a single process with focused ion beam implantation (from Ref. 94). The layers are 10-$\mu$m GaAs buffer, 2-$\mu$m undoped $Al_{35}Ga_{65}As$, 1.4-$\mu$m $n$-type GaAs, and undoped AlGaAs. The substrate is 100 semi-insulating GaAs. The higher resolution emitter ($p+$), gate ($p+$) and collector ($n+$), were defined by focused ion beam. Be or Si ions were selected by the computer controlled mass separator. Alignment was made to bench marks in the upper AlGaAs layer (see Fig. 13). Both ions were implanted at 80 and 160 keV. (b) Schematic of the ultrahigh vacuum system at the Optoelectronics Joint Research Laboratory in Kawasaki which combines an MBE system with a focused ion beam system (from Ref. 100). Sample analysis and sample preparation chambers are also included. By shuttling a wafer back and forth between the MBE and the ion beam, material can be patterned by implanting either donors or acceptors and then overgrown with new layers, as shown in Fig. 18(a).

### 2. Device fabrication

In silicon both MOSFET's[81,90,91,95] and bipolar devices[92,96,97] as well as resistor structures[98] have been fabricated using focused ion beams; mainly boron, but also arsenic,[95,96] has been implanted. While one of the goals of this work has been to demonstrate that focused ion beam implantation yields equivalent results to conventional implantation, i.e., no unexpected problems arise, the special lateral-doping-variation capabilities have also been exploited.

In bipolar devices the doping of the base under the emitter has been graded using focused ion beams. If the doping is reduced in the center of this region relative to the edges, the base resistance is somewhat lowered.[97] Various doping profiles have been produced and compared.[97]

In MOSFET's the focused ion beam has been used to implant boron in the middle of an $n$-doped channel thus making it $p$ type.[81] The minimum effective channel length is determined by the beam diameter to be 0.1 to 0.2 $\mu$m. These devices are reported to have 80% higher gain factor and 20% higher breakdown voltage than a conventional MOSFET.[81] Very recently, focused ion beams have been used to adjust the thresholds of transistors in the complementary metal-oxide semiconductor (CMOS) configuration in both $n$ and $p$ substrates and $n$ and $p$ wells.[95] The dose was varied in ten steps from $1\times10^{12}$ to $1\times10^{13}$ ions/cm$^2$ of both B and As. Smooth variation of threshold voltage as a function of dose was observed. Total variation was 0.8 to 1.2 V over the dose range.

In GaAs focused ion beams have been used to fabricate field-effect transistor's[90] (FET's) and combined light emitting diodes and junction field effect tranistors (J-FET's).[94] In addition, Ga implantation into $n$-type, Si-doped GaAs has been used to render the material insulating, i.e., increase its resistance by four orders of magnitude.[99] The FETs have shown characteristics similar to conventionally fabricated devices demonstrating the utility of the focused ion beam technique. The combined J-FET-LED (light energy diode) is shown in Fig. 18(a). Here, a molecular-beam epitaxy (MBE) grown heterostructure substrate was used, and both Si and Be were implanted with the focused ion beam.[94] A Au–Si–Be liquid metal ion source emits both singly and doubly ionized Be and Si. Thus by tuning the $E\times B$ mass filter one could implant either Be or Si, and select ions of either energy $E$ or $2E$, i.e., either 80 or 160 keV. The ion doses used are over $5\times10^{13}$ ions/cm$^2$ and are realized by varying the dwell time of the ion beam at each position. The focused ion beam system used in these implants is connected by an ultrahigh vacuum (UHV) sample transfer tube to a MBE system. Thus implantation and overgrowth can take place without contamination by atmospheric exposure.[94,100] This system, which represents an important step toward *in situ* fabrication, permits one to build many different devices integrated monolithically on the same substrate.[100] It is shown in Fig. 18(b).

MBE provides a means of growing III-V (and other) semiconductors with doping and composition control at the monolayer level. Since the band gap can thus be tailored from layer to layer, various quantum effects have been observed. The ability to further "write" on a layer with a focused ion beam may provide the opportunity to make quantum "dots" or other structures. Unfortunately, this is not straightforward since the focused ion beam at a few tens of keV energy will damage the MBE grown layers.

Clearly, a focused beam of low-energy ions, i.e., a few hundred eV or lower, is desirable for this application. Retarding fields to reduce the arrival energy of electrons[101] and ions[102] have been considered. For an ion beam current of 10 nA a retarding field which brings the energy from 50 kV to 500 eV is calculated[102] to suffer an increase in spot size from 0.3 to 0.8 $\mu$m due to space change. This beam broadening is found to fall rapidly as the current is lowered. Since many of

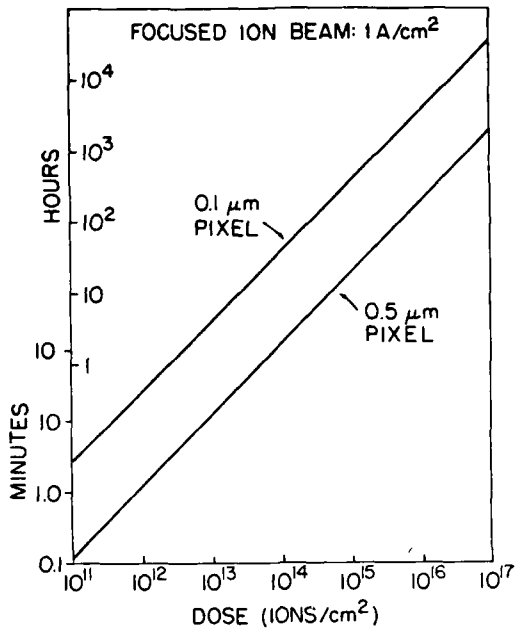


FIG. 19. The time taken to expose 1 cm² as a function of dose for two beam diameters (or pixel sizes).

the focused ion beam systems have beam currents of the typical semiconductor dopants in the 10- to 100-pA range, the space charge broadening should be negligible. The direct retarding field configurations considered so far[102] require that the sample be at an awkwardly high potential (e.g., ~50 kV). Lower energy ion beams would be advantageous not only for implantation into MBE grown layers but in other applications as well. As discussed above, Figs. 16 and 17, the straggle of the ions in a solid decreases with decreasing energy. Thus for implants with submicron resolution, lower energies are an advantage. For example, boron implanted into Si at 100 kV has a transverse straggle $\Delta R_t = 0.08\,\mu$m but at 10 kV this falls to $\Delta R_t = 0.016\,\mu$m.

An indirect application of focused ion beams to MBE grown materials is the selective disordering of the superlattice layers. A number of ion species can be used: Ga (Refs. 103 and 104), Si (Refs. 105–107), BE (Ref. 108), and others.[105] Doses of $10^{13}$ to $10^{15}$ ions/cm² followed by anneals in the range of 750–850 °C cause AlGaAs/GaAs superlattice to interdiffuse only where the implantation has occurred. In the case of Si doping followed by Be implant the reverse is true, i.e., the implant inhibits the interdiffusion.[108] This technique has been applied to make multiple quantum well lasers with a buried optical waveguide using a Be focused ion beam[108] as well as quantum dots with a conventional Ga implant using 0.1 $\mu$m e-beam lithographically defined resist dots. This last fact indicates that the potential lateral resolution of this technique is at least 0.1 $\mu$m.

The focused ion beam even at the current state of development has the capability to provide a variety of implant species, doses, and energies in a single fabrication step. This opens the possibility of combining a number of different devices on a single chip where normal fabrication would lead to an impossible number of different fabrication steps. On the other hand, focused ion beam fabrication in its present state is serial and, therefore, the throughput is limited. Figure 19 plots the time needed to implant a square cm to various doses. Therefore, focused ion beams are unlikely to replace conventional ion implanters for routine chip fabrication. The applications are likely to be in device prototyping and in special high performance devices. This is particularly true in GaAs and other III-V's where optical, logic, and microwave devices can be combined on the same substrate.

## B. Ion milling

### 1. General considerations

Broad beam ion milling, where ions (usually $Ar^+$) of a few hundred eV energy are incident on a surface, is a widely used method of material removal.[109] Usually one to two atoms of the substrate are removed per incident ion. This is called the yield. For focused ion beams, where the energy is about two orders of magnitude higher the situation is expected to be similar. The yield increases slowly as a function of energy then flattens out and turns downward at about 50 keV.[110]

With focused ion beams the characteristics of the milling (such as yield) are geometry dependent. When an ion beam is scanned in a line on a surface, a trench is produced which initially has the shape of an inverse Gaussian as expected from the beam profile. However, when the dose is increased, the trench becomes sharp, narrow, V-shaped, and unexpectedly deep[111,112] (see Fig. 20). In addition, the shape of a milled feature is also dependent on whether it is obtained with a single scan or repetitive scans even though the total dose is kept the same.[112,113] This is illustrated by the results shown in Fig. 21, where a 10× 10-$\mu$m square was scanned on Si to the same dose level using 200 repeated scans or a single scan. The shape in the multiscan is, as expected, a flat bottomed pit, but in the single scan the pit is very asymmetrical and about three to four times deeper at the end that was last scanned. Such effects are attributed to a combination of redeposition and self-focusing.[111,112]

Clearly, yield should be defined (and measured) in such a way that these geometric effects are avoided, namely with repetitive scanning over an area with lateral dimensions much larger than the depth milled. Thus if the material has a density $\rho_n$ (atoms/cm³), and an ion dose $\Delta$ (ions/cm²)

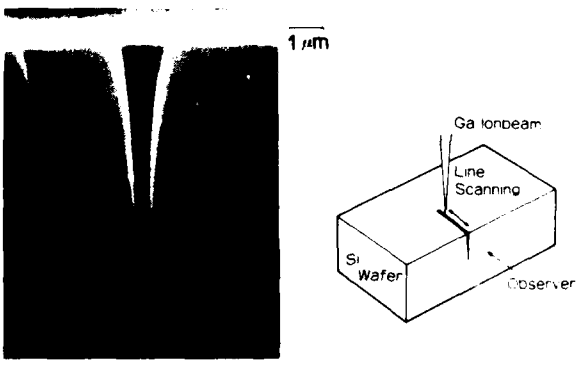


FIG. 20. Cross section of a groove made in Si with a focused ion beam of 30-kV Ga ions at 0.5 nA, scanned at 5 $\mu$m/s 120 times (from Ref. 112).

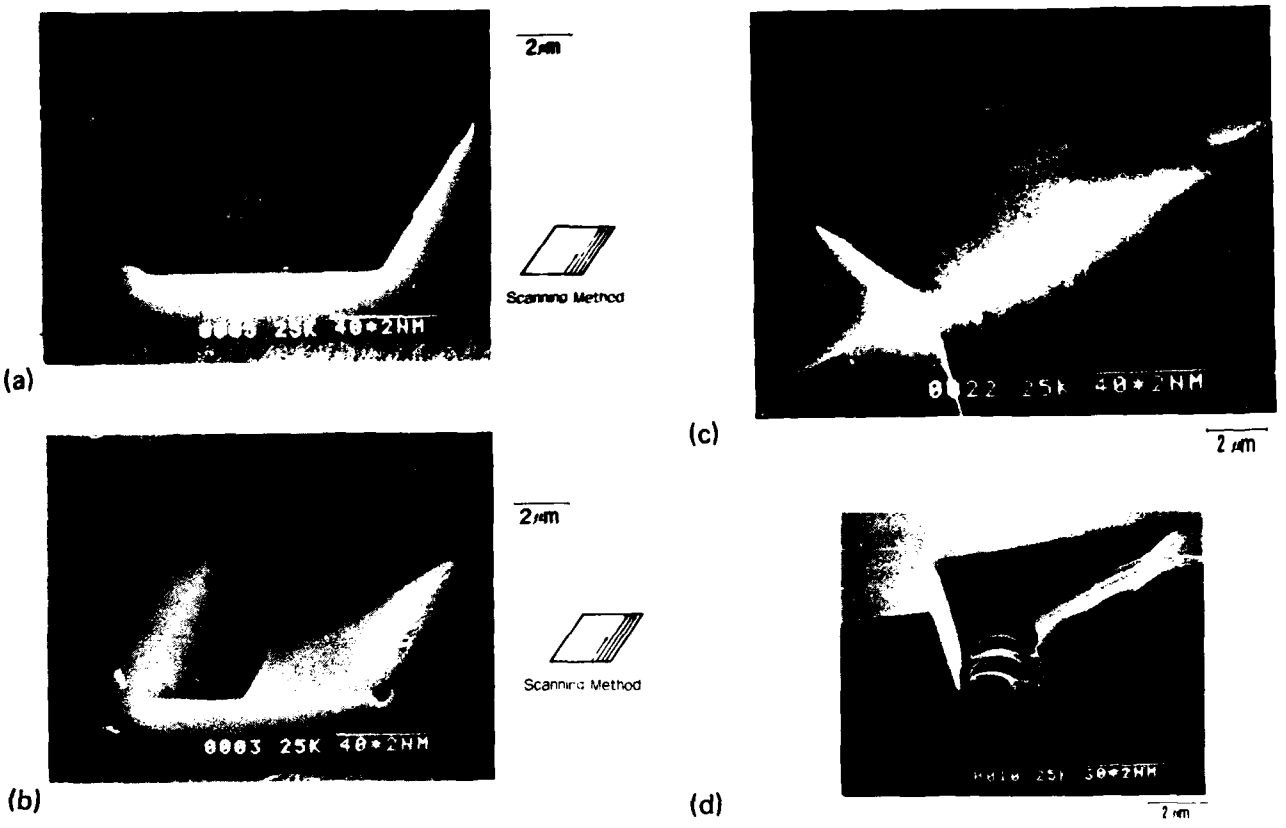


FIG. 21. Ion beam removal of silicon showing the dependence of feature shape on milling schedule (from Ref. 112). (a) Fast repetitive scan with 30 kV, 0.5 nA, 10 ms/line, 300 lines, repeated 200 times, total dose: $1.9\times10^{18}$/cm$^2$; (b) slow single scan with 30 kV, 0.5 nA, 2 s/line, 300 lines, 1 time, total dose $1.9\times10^{18}$/cm$^2$; (c) cross section of fast repetitive scanned area with the same conditions as (a); (d) cross section of slow single-scanned area with 30 kV, 0.6 nA, 2 s/line, 200 lines, 1 time, total dose $1.5\times10^{18}$/cm$^2$.

mills the material to a depth $d$ (cm), then the yield can be defined as

$$Y = (\rho_n d/\Delta) \text{ (atoms/ion)}. \quad (12)$$

Since for focused ion beams the milling ion is in most cases buried in the materials and may cause it to swell, the yield defined this way may not correspond exactly to the atoms removed per ion. Although various milling results have been reported, there is a shortage of data on milling yield. Table III shows data we have been able to glean from various sources.

### 2. Mask repair

The most immediate application of focused ion beams has turned out to be the repair of photomasks. Ion milling plays a central role here, as illustrated in Fig. 22. To repair opaque defects the unwanted chromium is simply milled off.[114,116–119] As the milling proceeds the bared glass surface is not smooth. However, if the milling is continued, a smooth surface is produced.[114] The milling ions do, of course, also imbed themselves into the glass. When gold ions are used to mill off the chromium, the remaining glass appears stained when viewed in an optical transmission microscope.[120] Such staining has also been reported for Ga ions which produce about 20% decrease in transmission.[121]

Clear defects can be repaired by milling a light scattering structure into the area to be rendered opaque.[116] A grating or a prism, for example, acts to scatter the light, and the area appears opaque when viewed in transmission, particularly when the incident light is collimated. This is usually the case in lithography application.

Focused ion beams are able to repair defects with a resolution of 0.2 to 0.3 $\mu$m (and finer if needed). Thus for optical masks with submicron features which are used in 1:1 projection or in contact printing such resolution is required. Laser mask repair techniques cannot achieve as fine a control (see, e.g., Fig. 23).

The repair of opaque defects in x-ray lithography masks

TABLE III. Sputter yields.

| Substrate | Ion | Energy (keV) | Yield atoms/ion | References |
|---|---|---|---|---|
| Cr | $Ga^+$ | 30–70 | 2.3 | 114 |
| Glass | $Ga^+$ | 70 | 0.68[a] | 114 |
| Cr | $Au^+$ | 50–70 | 4.5 | 114 |
| Si | $Ga^+$ | 30 | 2.6 | 112 |
| Al | $Ga^+$ | 68 | 4.2 | 115 |
| $SiO_2$ | Ga | 68 | 2.0[b] | 115 |

[a] Corresponding to sputtering rate of 0.064 $\mu$m$^3$/nC.
[b] Molecules/ion.

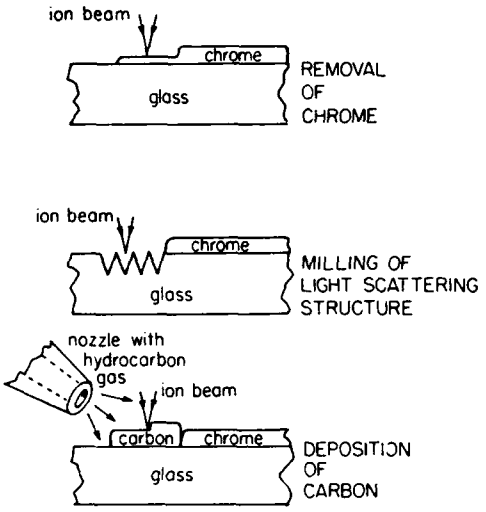


FIG. 22. Focused ion beam repair of photomasks. Top: removal of chrome by ion milling over programmed area. Middle: milling of light scattering structure to produce opaque area replacing missing chrome. Bottom: replacing missing chrome by ion induced deposition of carbon.

the higher resolution of the focused ion beam and is a clear advantage.[122,123]

### 3. Circuit microsurgery

Ion milling can also be used to intervene in fabricated or partially fabricated integrated circuits, for example, to cut conductors[115,124–126] as shown in Fig. 23. In addition, the focused ion beam can also be used to sense the voltage level of a part of an integrated circuit.[126,127] Thus direct diagnostics are possible. The focused ion beam has also been used to remove the passivation layer so that electron beam voltage contrast measurements can be carried out (Ref. 128).

With current research beams the cutting of a conductor, particularly if it is covered by a passivation layer can take several minutes.[115] This is because a beam with a current density of 1 A/cm$^2$ and a diameter of 0.1 to 0.2 $\mu$m is used even though the cut may need to be $\sim$1-$\mu$m wide. Since the etch time varies as the inverse square of the beam diameter, a diameter equal to the cut width should reduce the time by a factor of 25 to 100. In addition, beam current densities of 10 A/cm$^2$ have been reported.[44] Thus the cuts which now take several minutes could be made in a seconds or less. The main applications of this type of intervention are discretionary wiring and circuit debugging, where some small alterations in a circuit can be made without the need to repeat all of the fabrication steps.

Although the joining of two conductors using ion milling is not straightforward, a technique has been demonstrated for connecting two interesting metal films separated by an insulator such as $SiO_2$. As shown in Fig. 24, a straight sided hole is first milled through the top conductor and the insulator down to the lower conductor.[115,127] The milling area is then reduced and the material redeposited on the sidewalls produces a short circuit between the two conductors. Thus a window $1.5\times1.5$ $\mu$m milled through 0.6 $\mu$m of Al and 0.65 $\mu$m of $SiO_2$ followed by a concentric hole $1\times1$ $\mu$m yielded a connection of 0.4-$\Omega$ resistance and took 86 s to fabricate.[115] As discussed above this time can be reduced by at least two

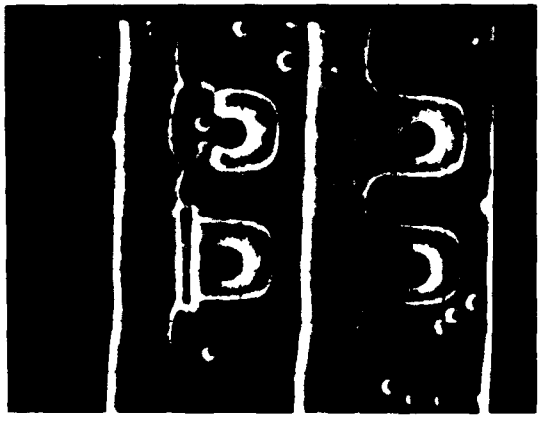

FIG. 23. Scanning ion microscope image of ROM comparing laser (upper left) and focused ion beam (lower left) cutting of conductors. The focused ion beam cut is 1 $\mu$m-wide and much neater and better controlled (from Ref. 123).

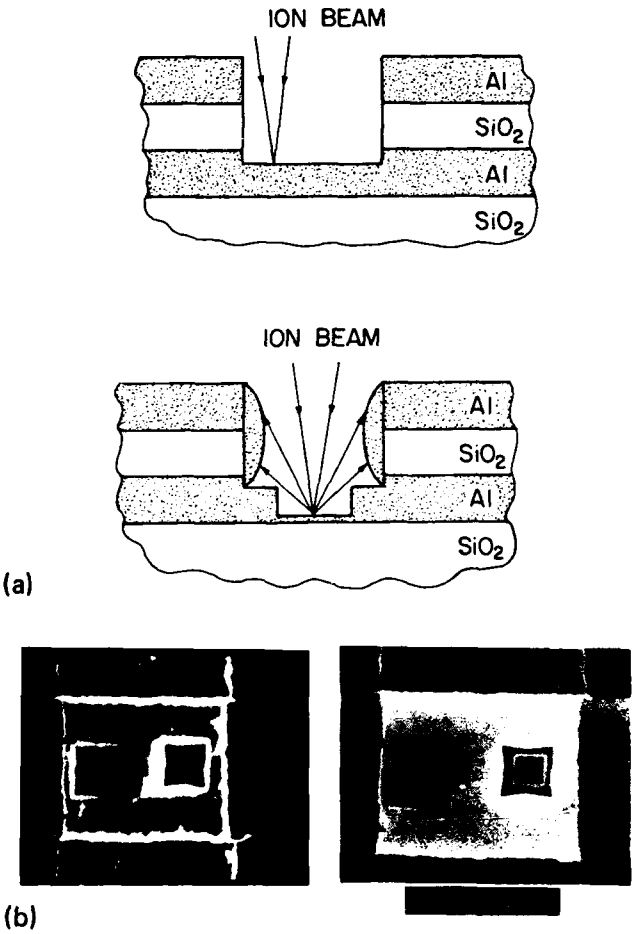


FIG. 24. (a) The joining of conductors using ion redeposition of the lower layer of metal (from Ref. 115). (b) Top view of milled via with redeposition. On left, scanning ion micrograph; on right, scanning electron micrograph. Resistance of the connection formed between levels is 0.4 $\Omega$.

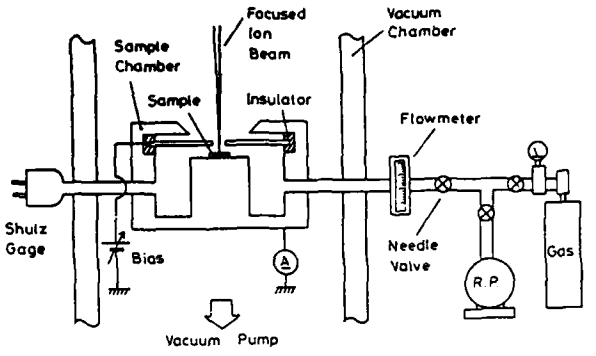


FIG. 25. Chamber used for ion beam assisted etching (and deposition) (from Ref. 136). The focused ion beam enters through a small bore hole. The gas, $Cl_2$ for etching, is fed into the chamber. The top of the chamber can be biased to extract the secondary electron due to the ion beam. Thus imaging of the sample can be done.

orders of magnitude by using a somewhat larger and a more intense beam. Furthermore, with the same 0.1- to 0.15-$\mu$m-diam beam, the window dimensions were reduced to $0.5\times0.5$ $\mu$m to yield a connection of 4-$\Omega$ resistance fabricated in 7 s.[127] For most integrated circuit applications a 4-$\Omega$ resistance is quite acceptable. This technique, while promising, requires that the conductors to be connected be intersecting. Ion induced deposition of conductors, discussed below, may be a more universal technique.

Very recently, microsurgery of optical circuits has also been reported (Refs. 129 and 130). Semiconductor lasers have been fabricated where the "mirror" ends have been cut by focused ion beam milling. These lasers show a decrease in quantum efficiency of only 8% compared to lasers with cleaved ends. This easy, versatile method of fabrication opens the door to a number of applications such as coupled cavity lasers (already reported[131,132]), integral lenses, and laser cavity length tuning.

## C. Ion induced surface chemistry

If a local gas ambient is produced near a surface, then the impact of energetic ions on that surface can induce chemical reactions. Thus focused ion beam assisted etching and focused ion beam induced deposition have been reported. (The term ion *induced* deposition is preferred over ion *assisted* deposition because the effect does not take place without the ion beam and because the term "ion *assisted* deposition" is being used to describe direct sputter or e-beam deposition with simultaneous ion bombardment.) The ion induced chemistry is thought to occur in an adsorbed layer rather than in the gas above the surface. The phenomenon bears some resemblance to laser induced chemistry,[133] where an incident laser is used to activate surface reactions. The resolution of this process is ultimately limited by the focal spots which can be achieved with light. Features of $\sim0.4$ $\mu$m dimension have been reported. In addition, electron beams may also be used to initiate reactions.[134] Here, the resolution may be as fine or finer than achievable with ion beams. In fact, a 0.15-$\mu$m-wide line has been reported.[134]

### 1. Etching

The apparatus used in the focused ion beam assisted etching is shown in Fig. 25 (Refs. 135 and 136). The sample is located in a separate chamber which has a small hole 0.5 to 2 mm in diameter in a 0.2-mm-thick plate. The ion beam is incident on the sample through this hole and can be deflected to produce patterns. A gas such as $Cl_2$ is introduced into the chamber up to a pressure of 30 mTorr. The vacuum outside of the chamber where the focused ion beam is generated is maintained near $10^{-6}$ Torr.

With this apparatus both silicon[136] and GaAs[135] have been etched. The etch rate for GaAs obtained is about ten times larger than the milling rate that would be obtained in the absence of the $Cl_2$ gas. Grooves 6-$\mu$m deep and 0.1-$\mu$m wide at the bottom have been etched in silicon.[136] The maximum etch rate observed corresponds to the removal of 10 Si atoms per incident $Ga^+$ ion (35 keV). The etch rate was dependent on the ion beam scan speed, and for fast, repeated scans above $\sim1000$ $\mu$m/s dropped to zero. This was tentatively attributed to the fact that $Cl_2$ builds up an adsorbed layer which prevents the ion beam from reaching the $Cl_2$/Si interface. At slower scan speeds the beam removes the excess $Cl_2$ and initiates chemical reaction at the interface.[136]

### 2. Deposition

If a gas, such as $Al(CH_3)_3$ or $WF_6$, is substituted for the $Cl_2$ in the apparatus of Fig. 25, deposition rather than etching is observed.[137–139] With $Al(CH_3)_3$ and a 35-keV $Ga^+$ ion beam a line with an approximately Gaussian cross section and 0.5-$\mu$m width is deposited (see Fig. 26). This beam profile is believed to reflect the intensity profile of the incident ion beam. The gas pressure in the cell (as in Fig. 25) was 30 mTorr and the line dose of $Ga^+$ ions was $1.3\times10^{13}$/cm. Thus it is estimated that with a 1-A/cm$^2$ beam of 0.5-$\mu$m diameter a 100-$\mu$m-long line such as in Fig. 25 is written in 10 s.

The composition of a large area of film deposited using a 50-keV $Ar^+$ ions was found by Auger analysis to be composed of aluminum, oxygen, and carbon in the ratios Al:O:C of 5.2:3.5:0.2 (Ref. 139). The inclusion of oxygen is thought to be due to the background gas in the vacuum chamber. This is not surprising since cermets (mixtures of Al and O) are typically e-beam evaporated with a background as of 2–

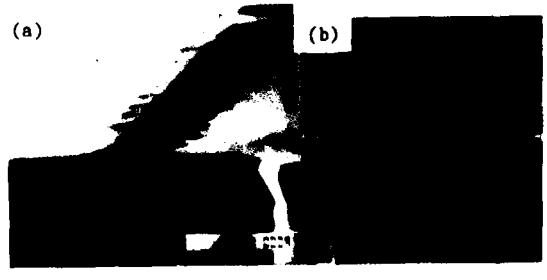


FIG. 26. A film deposited on Si from $Al(CH_3)_3$ gas using 35 kV $Ga^+$ ions (from Ref. 138). The linewidth is 0.5 $\mu$ (FWHM), and its profile is the beam profile; (a) shows line in perspective and (b) in an end view. Chamber used is similar to the one shown in Fig. 25.

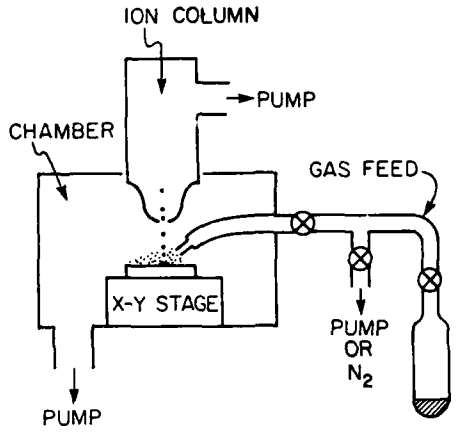


FIG. 27. A schematic of the focused ion beam chamber with capillary gas feed tubing (from Ref. 142). Since the vapor pressure of the gold compound was 0.7 Torr at room temperature a fairly large diameter capillary 1.4-mm inner diameter was used. For other gases such as $WF_6$ 0.15-mm diameter is appropriate.

$5\times10^{-6}$ Torr of $O_2$.[140] Tungsten deposition from $WF_6$ with 50-keV $Ar^+$ irradiation yielded films of composition ratio W:O of 2:1. No fluorine was detected.[139]

In an experiment,[141] where $WF_6$ gas was fed to the surface with a small capillary tube in place of the enclosure (Fig. 25) and a 750-V $Ar^+$ ion beam at 0.5 mA/cm$^2$ was used to bombard the entire surface a deposit was observed at the mouth of the tube. It was Auger analyzed to have a composition of W:O:C of 9:0.5:0.5. The surface was first cleaned by ion bombardment with no $WF_6$ flowing. If this was not done, the carbon content was near 30%.

Recently, gold has been deposited using focused (and implanter) ion beams and a capillary feed (Fig. 27) of dimethyl–gold–hexafluoroacetylacetonate.[142] Linewidths of $\sim0.5$ $\mu$m, equal to the ion beam diameter, have been observed (Fig. 28).

The film thickness deposited versus dose has been investigated with $Be^{++}$ and $Au^{++}$ ions. The dependence is approximately linear, and with $Al(CH_3)_3$ 130 nm are deposited with a $Au^{++}$ dose of $10^{17}$ ions/cm$^2$. With $Be^{++}$ the rate was half as large.[139]

The mechanism of breakup of the adsorbed gas film is thought to include both nuclear collision processes and electronic collision processes. Heating is ruled out.[139]

Overall the results so far are promising. Focused ion beam induced carbon deposition from hydrocarbon gases is already being used to repair defects in photomasks.[118,119] Details of these processes are proprietary. With more development work ion induced deposition will find other applications. For example, since conducting metal films can be deposited with conductivity comparable to poly Si,[142] integrated circuit microsurgery (discussed above) takes on a new dimension. Now, one can first dig through the passivation and then deposit-in a metal plug and run a conducting film to another part of the circuit. In addition, gate arrays could be connected over limited areas for prototyping. Because ion bombardment (or ion assisted etching) can be naturally made to precede deposition, contacts could be made where contamination or oxidation is detrimental such as in III–V compounds grown by MBE. Ion induced deposition may well play a central role in future *in situ*, all vacuum processing.

## D. Focused ion beam lithography or ion induced chemistry in the bulk

The word lithography as it is used in microfabrication has come to mean the transfer of a pattern from a mask with transparent and opaque areas or from a computer memory to a surface relief in a thin film on a substrate. This thin film is called a resist and the transfer vehicle can be either UV photons, x rays, electrons, or ions. In reference to ions there is a tendency to broaden the meaning of lithography further and refer to the entire field of focused ion beam fabrication as ion beam lithography; this is unfortunate. Since as we see from the above examples of patterned implants, ion milling, and ion induced deposition or etching, the focused ion beam permits patterning *without* the use of resist or mask.

In this section the use of focused ion beams to alter a surface film (resist), either organic or inorganic, in a desired pattern will be discussed. This film is then treated (developed) so as to create a relief pattern. The resist can be either positive or negative, i.e., the development either removes the exposed or the unexposed parts of the film.

In the previous section ion induced chemical reactions on the surface were discussed. In lithography the chemical reactions occur in the bulk of a film. Usually the film is on the surface of a substrate solely for the purpose of patterning.

### *1. Organic resist*

All patterning in present day microfabrication of integrated circuits is done using organic resist films. While, as discussed above, one of the main attractions of focused ion beam fabrication is that it may in some cases eliminate this dependence on the standard mask/resist processing, resist

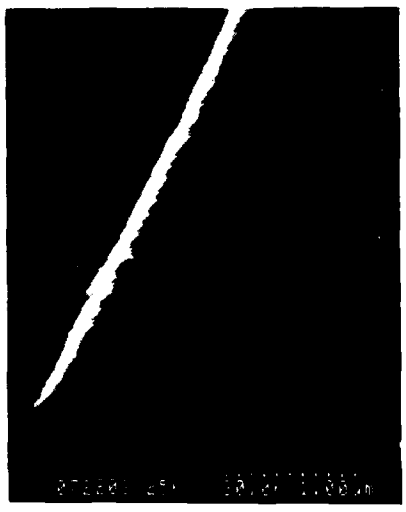

FIG. 28. Focused ion beam deposition of a submicron width gold stripe (from Ref. 142). The total line dose of 15-kV $Ga^+$ ions is $2.5\times10^{13}$ ions/cm. The composition of the film is Au 75%, Ga 20%, carbon $<5$%, oxygen $<5$%. The yield is 4 to 5 gold atoms/ion. The resistivity is $5\times10^{-4}$ to $1.3\times10^{-3}$ $\Omega$ cm (bulk Au $= 2.5$ $\mu\Omega$ cm).

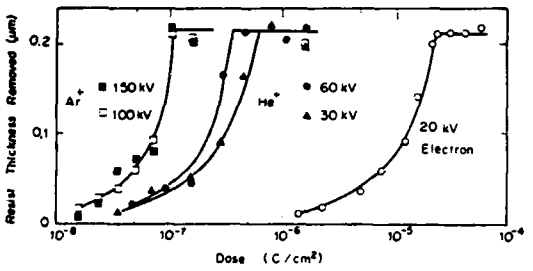


FIG. 29. Exposure characteristics of PMMA resist with electron and ion irradiation (from Ref. 144). The curves are of resist thickness removed after a development time of 2 min in MIBK (methyl isobutyl ketone) at 25 °C. The initial film thickness was 0.21 $\mu$m.

exposure itself is also a potential application of ion beams. The early work on focused ion beams[1] already demonstrated the exposure of PMMA (polymethylmethacrylate, a deep UV, e-beam, or x-ray resist). Focused ion beam lithography is in principle similar to e-beam lithography.

The dose needed to expose most resists such as PMMA by ions is about two orders of magnitude lower than for electrons[143–145] (see Fig. 29). Thus a dose of $2\times10^{-5}$ C/cm$^2$ is needed to expose PMMA with 20 keV electrons while for argon ions at 120 or 150 keV a dose of 0.3 to $1\times10^{-7}$ C/cm$^2$ (or 2 to $6\times10^{11}$ ions/cm$^2$) is sufficient.[143–145] This comparison is somewhat unfair since electrons penetrate much deeper into resist than ions.[143,146] Curves of energy deposition rate are shown in Fig. 30. Also the higher the mass of the ion the lower its penetration depth into the resist, and the lower the dose (per unit area) required to expose resist. Of course, a potential drawback is that the resist thickness which can be used is limited.

Another important limitation of focused ion beam exposure of resists is shot noise.[147,148] The numbers for the dose needed for exposure quoted above are for large features. If one wants to expose features of, say 0.1 $\mu$m, then at $10^{-7}$ C/cm$^2$, there would only be 70 ions incident per $0.1\times0.1$ $\mu$m area. The statistical fluctuation in this number may create variations in exposure level and, in addition, may create edge roughness of exposed lines. Monte Carlo calculations of the energy deposited in resist by incident ions have been used to simulate these fluctuations. The conclusion is that for a $0.1\times0.1$ $\mu$m area, which is to be well-formed down to a resolution of 0.01 $\mu$m, about 1200 ions are needed for complete exposure[147] (see Fig. 31). The calculations are for 50 keV protons ($H^+$ ions), 100 keV $H_2^+$, and 150 keV $Li^+$ ions and yield about the same result. In addition, since more than an order of magnitude of overexposure is needed to avoid the shot noise, broadening of the features by 300–500 Å is to be expected.[147]

Another analysis of the statistical effects of ion beam exposure of resists concludes that for a probability of 99% that all pixels on 1 cm$^2$ are exposed one needs to have only 30 ions

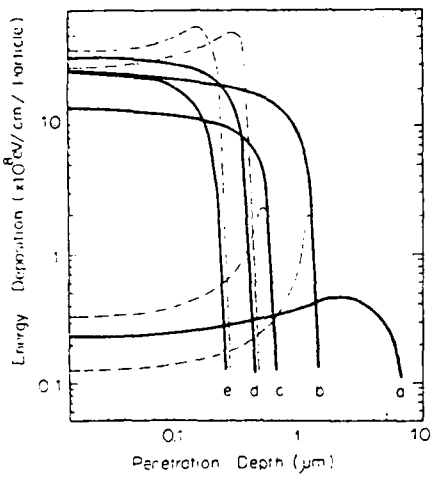


FIG. 30. Calculated curves of energy deposition rate in PMMA resist as a function of the penetration depth: (a) 20 kV electron; ( , 200 kV $He^+$; (c) 60 kV $He^+$; (d) 250 kV $Ar^+$; and (e) 150 kV $Ar^+$. For the curves representing the ions, solid and broken lines are of electronic and of nuclear collision loss, respectively (from Ref. 144).

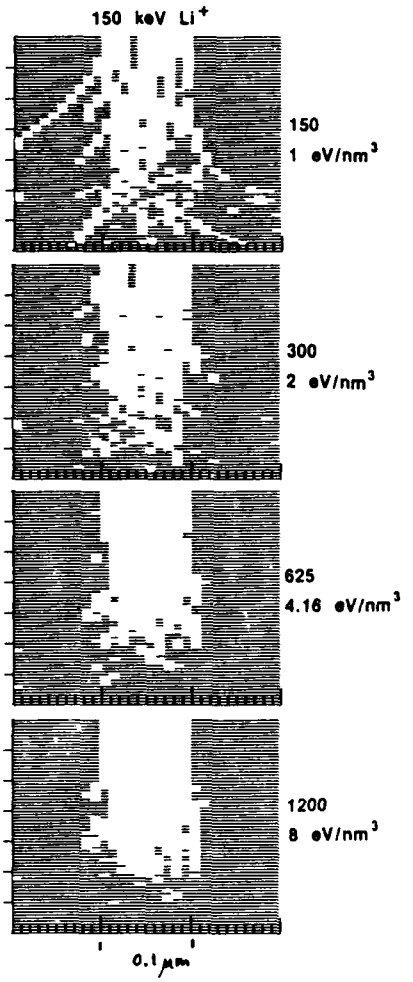


FIG. 31. Resist exposure profiles for 150, 300, 625, and 1200 Li ions of 150 keV energy incident on a $0.1\times0.1$ $\mu$m area (from Ref. 147). The resist is taken to be PMMA 0.4-$\mu$m thick. (Note that the horizontal and vertical scales are not the same. The random paths of ions are followed by a Monte Carlo computer simulation. The resist and substrate is divided into cubic bins 10 nm on a side. If the incoming ion has lost enough energy in a given bin to increase its dissolution rate in the developer to 1/2 of "complete" exposure then this bin is shown clear in the figure.)

FIG. 32. Chloromethylstyrene, a negative resist, exposed with 100-kV $Be^{++}$ to a dose of $3.5\times10^{12}$ (ions/cm$^2$) (from Ref. 152). Resist thickness 300 nm, linewidth 50 nm.

incident on a $0.1\times0.1$ $\mu$m pixel.[148] The discrepancy appears in part to be due to the fact that in the Monte Carlo calculation[147] a finite volume of resist is considered and the pixel is required to be "well-formed." Thus the $0.1\times0.1$-$\mu$m pixel corresponds to higher "resolution." A recent analysis addresses this issue of resolution and particle statistics.[153] It concludes that 29 ions are needed per $0.05\times0.05$-$\mu$m pixel. This variation in results arises because the criteria for exposure and the definition of a pixel are different.

Experimentally PMMA and poly(trimethylsilystyrene-co-chloromethylstyrene), P($SiSt_{90}$-$CMS_{10}$), have been exposed in fine lines with ever decreasing doses of 100-kV $Ga^+$ ions until the lines became discontinuous.[149] The P($SiSt_{90}$-$CMS_{10}$) is continuous at a dose of $1.5\times10^{11}$ ions/cm$^2$ but discontinuous at $7.2\times10^{10}$ ions/cm$^2$. The linewidth is 0.11 $\mu$m. Thus there are only 18 ions per ($0.11\times0.11$ $\mu$m) area element in the continuous line and nine in the discontinuous. For PMMA a continuous line 0.06-$\mu$m wide is obtained with $Ga^+$ at $9\times10^{11}$ ions/cm$^2$ which becomes discontinuous at one-half that dose.[149] The continuous line has 32 ions per ($0.06\times0.06$ $\mu$m) pixel. PMMA has also been exposed by $Be^{++}$ ions. At 140 keV 0.45-$\mu$m-thick PMMA was exposed with a 0.1-$\mu$m-diam beam to yield well formed lines with vertical sidewalls and a width below 0.15 $\mu$m.[150] At 200 keV $Be^{++}$ ions were able to form lines of 0.03-$\mu$m width with a line dose of $3.4\times10^7$ ions/cm even though the Gaussian beam width was 0.18 $\mu$m.[151] In this case the line width is, of course, a steep function of dose.

Chloromethylstyrene (CMS) is a negative resist and has been successfully used with 100 kV $Be^{++}$ ions. Well-formed lines of 50-nm width have been exposed in 300-nm-thick resist[152] (see Fig. 32).

An important practical consideration is the time needed to expose a given area with a fine pattern. As seen above if a $Ga^+$ beam is used doses between $1.5\times10^{11}$ and $10^{12}$ ions/cm$^2$ are needed. Thus for a 0.1-$\mu$m-diam beam at 1 A/cm$^2$ 50% of a 1-cm$^2$ area can be exposed in 1.5 to 10 min. It should be noted that beams of 10 A/cm$^2$ have been reported,[44] and 100 A/cm$^2$ have been projected.[87] The very high brightness liquid gas ion sources[35,36] have not yet been applied to lithography. In addition, a statistical analysis which compares all lithographies on the same footing finds that the pattern transfer rate for focused ion beams and e-beams is nearly the same.[153] Considering the fact that e-beam lithography has had 15 years of intensive development while ion beams are in comparative infancy, the outlook for practical ion beam lithography in the future is good.

To avoid proximity effects and coax high resolution out of e-beam lithography multilevel resists or other tricks are used.[146] Such measures are being explored for ion beams. For example, a bilevel scheme with poly(trimethylstyrene-co-chloromethylstyrene) on top of AZ 1450J resist has been used.[149] The upper level is exposed by a dose of $2.4\times10^{11}$ ions/cm$^2$ of $Ga^+$ at 100 keV. After development the upper level resists an oxygen reactive ion etch. Thus high aspect ratio structures are produced (see Fig. 33).

The finite range of the ions in the resist can be used to advantage. By carefully choosing the resist thickness and ion energy one can minimize the damage to the substrate.[154] In addition, the finite range can be used to advantage to create special structures. For example, a T-shaped metal gate structure is shown in Fig. 34, which uses alternate exposures by 200-keV Be and Si ions.[155]

Plasma development of PMMA exposed by focused ion beams has also been demonstrated.[156,157] Here, PMMA acts as a negative resist, and the areas that are ion irradiated show a much decreased etch rate in $O_2$ containing plasmas. The doses required, however, are in the range of $6\times10^{14}$ to $10^{16}$ ions/cm$^2$, i.e., 2–3 orders of magnitude higher than for normal, wet developed, PMMA exposure.

### 2. Inorganic resists (or etch rate modification by ion bombardment)

Focused ion beams have been used to pattern a thin film or a surface by first implanting a region and then etching it in either a plasma or a liquid. The implanted region can become either soluble or insoluble. (i.e., the "resist" is either positive or negative.) This phenomenon is included under lithography because it can be used to pattern thin film which can then serve as a mask for further processing steps. Of course, thin film or surface patterned by implantation and etching can be the end in itself. In this case the term lithography does not really apply.

A number of materials have been patterned in this way as summarized in Table IV. The physical phenomena responsible for the etch rate change appear to be diverse. In Si and GaAs (Ref. 159) the ions appear to damage the substrate and increase the etch rate in the damaged regions. The Sb implant in Cr appears to not be attacked by the $CCl_4$ plasma, even though the amount of Sb implanted corresponds to a little more than a monolayer. This implant withstands the etching of the surrounding Cr to a depth of 0.5 $\mu$m. After the $CCl_4$ plasma etching the Sb concentration on the surface increases.[158] Al/O cermets can act as ion resist[162] as well as III–IV compounds.[163] In the latter case photoelectrochemical etching is used and very low doses are needed ($\sim5\times10^{10}$ ions/cm$^2$).

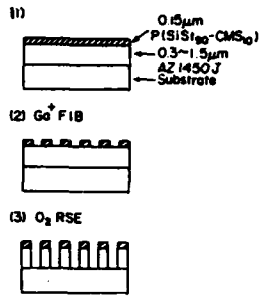


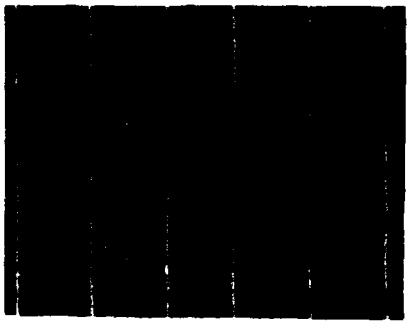

POLY(TRIMETHYLSILSTYRENE-CO-CHLOROMETHYLSTYRENE)
$P(SiST_{90}\text{-}CMS_{10})$ EXPOSED WITH 100 KEV
$GA^+$ AT $2.4 \times 10^{11}$ IONS/$CM^2$

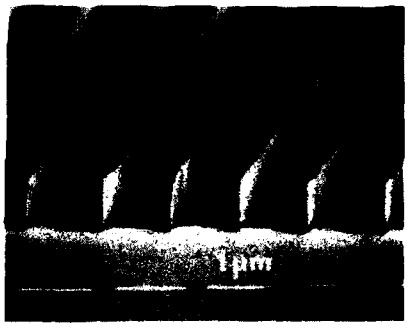


AFTER $O_2$ RIE OF AZ RESIST
USING $P(SiST_{90}\text{-}CMS_{10})$
AS MASK

FIG. 33. Bilevel resist exposure with 100-keV $Ga^+$ at a dose of $2.4\times10^{11}$ ions/cm$^2$ (from Ref. 149). Schematic shows steps in the fabrication, on right is photo of the first layer after development, and the perspective view lower left is the lower level patterned by $O_2$ reactive ion etching.

## E. Microanalysis

Secondary ion mass spectroscopy (SIMS) is a standard surface analysis technique of high sensitivity. In this technique an ion beam probe, often many micrometers in diameter, is used to sputter off atoms and ions from a surface. These are then picked up by a mass spectrometer and analyzed. The composition of the surface can thus be measured. The development of finely focused ion beams has permitted the ion probe resolution to be pushed below 0.1 $\mu$m, in some cases to 20 nm (see Refs. 166–169).

An apparatus developed jointly by the University of Chicago and the Hughes Research Laboratories is shown schematically in Fig. 35. If this apparatus is set up to detect $Ca^{40+}$ ions, for example, which are present in the specimen in 23% concentration, then a counting rate of $2\times10^4$ counts/s pA (or 1 count/300 incident ions) is observed.[166]

The mass analysis capability can be added to most focused ion beam systems, for example, those with mass separation.[170]

The ultrahigh resolution SIMS has been used to analyze fossil diatoms, minerals, and contaminants on Si,[166] as well as integrated circuits,[167] optical fibers,[168] and graphite intercalated compounds.[171] A sample of analysis of an integrated circuit is shown in Fig. 36. The locations of Al, Si, and Ca are displayed. The latter element is a contaminant. As shown in part (a) of the figure all ion species can be collected to show a topographic figure. Alternatively the secondary electrons can be collected to yield a similar figure as will be discussed in the next section.

## F. Scanning ion microscopy

Every focused ion beam system known has a channel electron multiplier for detecting the electrons emitted from the

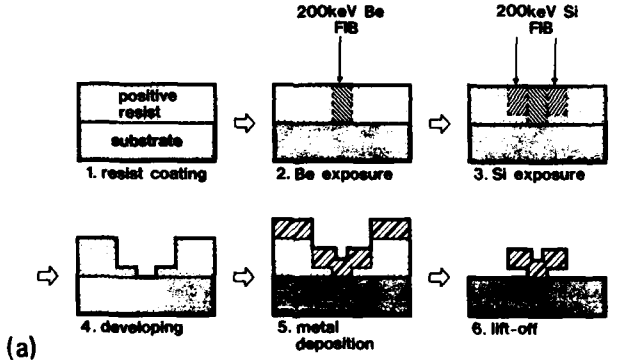


FIG. 34. (a) Shows the fabrication sequence for producing the T-shaped gate structure (from Ref. 155); (b) shows the resist (PMMA) pattern (left) and the resulting metal gate pattern (right) produced by liftoff.

TABLE IV. Inorganic film (resist) patterning.

| Material | Implant | Etch | Remarks | References |
|---|---|---|---|---|
| Cr | 50 or 100 keV Sb | $CCl_4$ plasma | 0.3 to 0.4-$\mu$m wide 0.5-$\mu$m deep | 158 |
| Si | 50 keV $In^+$ $\sim 5\times10^{13}$ ions/cm$^2$ (50 keV $Sn^+$ and 50 keV $Ga^+$ also used) | $H_3PO_4$ at 195°C (implant etched) | 50-nm-wide wide lines formed | 159 |
| GaAs | 50 keV $Ga^+$ $1.2\times10^{14}$ ions/cm$^2$ | HCL at 50 °C (implant etched) | 30-nm-wide lines formed | 159, 160 |
| Al | 50 keV $As^+$, $Sb^+$ ($N_2 + Ar^+$ implanter) $5\times10^{15}$ ions/cm$^2$ | $H_3PO_4$ (irradiated area not etched) | Carbon contamination resist formed | 161 |
| Al/O cermet | 30 and 75 keV $Ar^+$ 70 keV $Ga^+$ | $H_3PO_4/HNO_3$ Transene A (irradiated not etched) | $Al_2O_3$ enhanced on surface | 162 |
| GaAs, InP, InGaAs, InGaAsP, InGaAsP $n$ type | 20 keV $Ga^+$ $<5\times10^{10}$ ions/cm$^2$ | Photoelectrochemical, 2-M-$H_2SO_4$ electrolyte | Very low dose needed | 163 |
| $SiO_2$ | 20–70 keV $Ga^+$ 140 keV $Si^{++}$ ($1.2\times10^{13}$ to $6\times10^{14}$ ions/cm$^2$) | Ammonium fluoride and glacial acetic acid (exposed area etched) | Implant changes etch rate by up to factor of 5 | 164 |
| Spin-on glass | 16 keV $Ga^+$ ($10^{16}$ ions/cm$^2$) | $CHF_3/O_2$ plasma | Implant reduces etch rate by 30% | 165 |

surface where the ion beam is incident. The signal from the channel electron muliplier is used to modulate a cathode ray tube. Thus the scanning ion microscope is the same as a scanning electron microscope except that an ion beam instead of an electron beam is scanned over the surface. (Figure 35 shows a channel electron multiplier on the right, for example, as well as a mass spectrometer on the left of the beam.)

This imaging capability supports many of the applications discussed above. It is used to focus the ion beam when initially setting up operation, to examine just milled features [see Fig. 24(b)], and to align to existing features on a wafer (see Fig. 13). Imaging is also very much a part of mask repair by focused ion beams. One first locates the defect on the screen, outlines its perimeter and then removes it by either ion milling or deposition. While an area is being examined, it is of course also being sputtered away and implanted. These, usually undesirable, effects can be minimized by using frame storage, i.e., forming an image on the screen and then blanking off the beam. In general, less than a monolayer is sputtered off to make an image.

In addition to the imaging as a support for other applica-

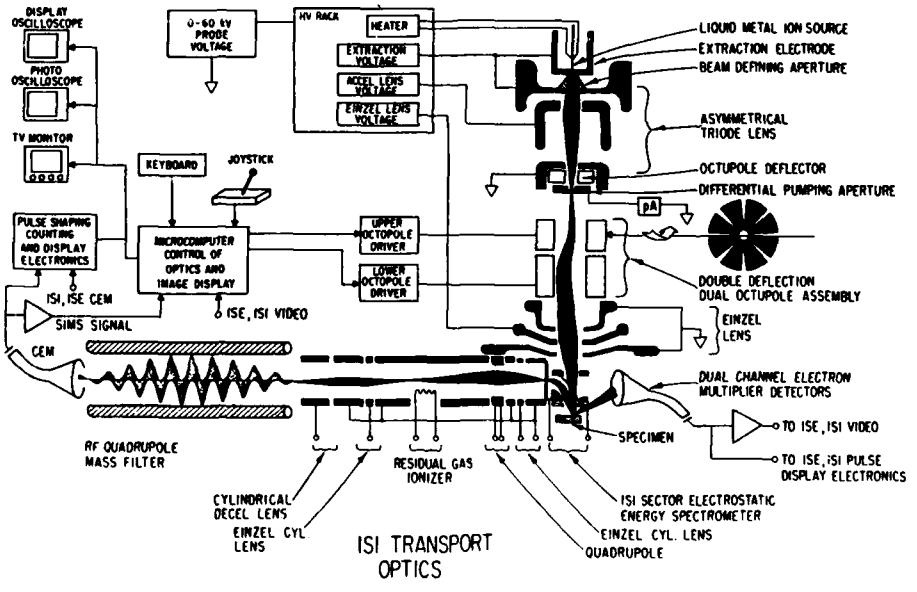


FIG. 35. Schematic of a scanning ion microprobe (from Ref. 166) developed jointly by the University of Chicago and the Hughes Research Laboratories. The ion probe operates with elemental liquid metal ion sources, typically $Ga^+$, with a total acceleration voltage of 40 to 60 kV. With an ion current of 1.6 pA on the sample the probe beam diameter is calculated to be 20 nm.

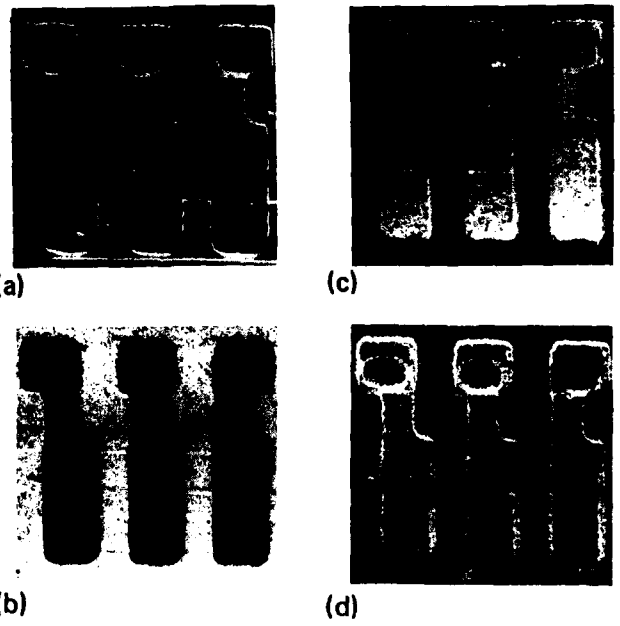


FIG. 36. Integrated circuit section, coated with Pd–Au to prevent charging (from Ref. 167). 10 $\mu$m. (a) Surface topography from ion induced secondary ion signal, i.e., all species of emitted ions are collected and used to modulate the intensity on the CRT, 64 s to make image. (b) Same area but $Si^{28}$ is collected for $1.6\times10^6$ counts in 225 s. (c) $Al^{27}$ ions collected for $1.4\times10^6$ counts in 256 s. (d) $Ca^{40}$ ion map. $7.9\times10^5$ counts in 512 s. The full field size in each is 50 $\mu$m.

tions, the focused ion beam can be considered as a microscopy tool in its own right[43,172] (see Fig. 37). Here it is in competition with the scanning electron microscope (SEM). While most electron microscopes have beam diameters at least an order of magnitude finer than present ion beams, the ion microscope still offers some unique advantages. As seen in Fig. 24(b), for example, where the same area is displayed in a SEM and a scanning ion microscope (SIM), the SIM is more sensitive to surface topography. The SEM on the other hand, often does not have enough contrast to show up surface features such as shallow steps, which are visible even in a high power optical microscope. The SIM also has a large depth of focus[69] and often is less sensitive to charging of insulating surfaces.[172] In many cases of SEM examination samples have to be coated with 10 to 30 nm of metal to be observable, and the advantages of an ultrafine beam are not fully utilized.

Thus scanning ion microscopy may be a useful high-resolution imaging tool in addition to supporting all of the other focused ion beam applications.

## V. SUMMARY

We have discussed the machinery needed to generate finely focused ion beams, and have reviewed the applications, mainly in the area of microelectronics fabrication. The areas of application can be grouped as follows: direct maskless, resistless patterned implantation; ion milling; ion induced surface reactions for etching or deposition; lithography, i.e., exposure of resist; microanalysis; and microscopy. So far most applications, with the possible exception of photomask repair, are in the research stage.

Because of their versatility and their ability to eliminate conventional mask/resist patterning, focused ion beams are likely to play a role in *in situ* processing. The first step in that direction is the joining of focused ion beam and MBE.[100] Here, future development of low-energy ion beams may be important.[101,102] Ion induced deposition raises the possibility of *in situ* contacts and wiring.

Focused ion beam fabrication is serial, i.e., point by point, and of necessity slow. Yet even at present many applications are feasible. In the future, the development of achromatic lenses may increase the beam current by a factor of 100. Shaped beams, already developed for e-beam lithography, greatly increase processing speed at the expense of some flexibility. Projection of stencil masks has shown pattern transfer rates of $10^5$ times higher than point beams[173] but gives up more flexibility. Developments in source technology, such as elemental sources to replace alloy sources or novel molecular-beam ion sources, which have been analyzed theoretically,[174] may remove the need for mass separation, simplify the ion columns, and lead to higher beam currents.

The use of focused ion beams in lithography is very analogous to e-beam lithography. However, ions have less proximity effect and may well be preferred in the future as the machinery develops.

The repair of photomasks by focused ion beams appears to be entering the commercial market. X-ray lithography masks, which will have much finer features and be even more complex, will demand focused ion beam milling and ion induced deposition of high $z$ material such as Au or W. Not only can masks be repaired but in some case fabricated or partly fabricated integrated circuits can be addressed and altered locally for defect avoidance or for design error correction for prototyping.

The many diverse and important applications of focused ion beams discussed herein indicate that it is a fruitful area of research. This has been recognized and the field has grown to where there are at least 35 sophisticated systems in use

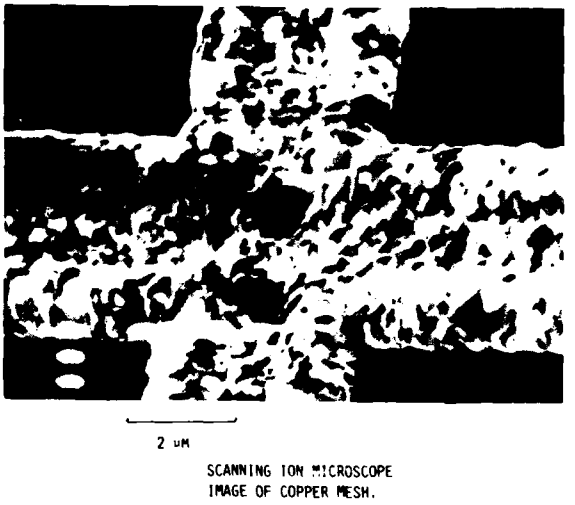


FIG. 37. Scanning ion microscope image of a copper mesh (from P. Prewett IBS Dubillier). A resolution of 40 nm is evident.

worldwide, about 25 of them in Japan. The outcome of the research will point to where the focused ion beam will find applications in manufacturing.

## ACKNOWLEDGMENTS

Although the writing of this paper was not directly sponsored, the author's focused ion beam work at MIT is supported by DARPA, Draper Laboratories, Hitachi, and Nippon Telegraph and Telephone. The author is grateful to the many colleagues who have sent preprints and answered queries. Thanks are due H. Yamaguchi, S. Matsui, E. Miyauchi, H. Morimoto, L. R. Harriott, K. Gamo, R. L. Seliger, R. Levi-Setti, and P. D. Prewett for providing copies of figures. Critical comments on all or part of the manuscript by N. P. Economou, H. Lezec, and W. Thompson as well as by the anonymous reviewers have been most helpful. Two factors have played a key role in the conception of this paper and indeed in the author's entry into this field: The first is the help that R. L. Seliger and his colleagues at Hughes Research Laboratories have provided by sharing their knowledge and experience and by collaborating in research, and the second is the learning experience that H. I. Smith has provided by asking the author to give guest lectures on focused ion beams and implantation in his course on Submicrometer Structures Technology over the past three years.

[1]R. L. Seliger and W. P. Fleming, J. Vac. Sci. Technol. **10**, 1127 (1973); J. Appl. Phys. **45**, 1416 (1974).
[2]R. Levi-Setti, in *Scanning Electron Microscopy 1974*, Part I, Proceedings of the 7th Annual Scanning Electron Microscope Symposium (IIT Research Institute, Chicago, IL, 1974), p. 125.
[3]J. H. Orloff and L. W. Swanson, J. Vac. Sci. Technol. **12**, 1209 (1975).
[4]J. H. Orloff and L. W. Swanson, J. Vac. Sci. Technol. **15**, 845 (1978).
[5]J. H. Orloff and L. W. Swanson, J. Appl. Phys. **50**, 6026 (1979).
[6]W. H. Escovitz, T. R. Fox, and R. Levi-Setti, Proc. Natl. Acad. Sci. USA **72**, 1826 (1975).
[7]R. Levi-Setti and T. R. Fox, Nucl. Instrum. Methods **168**, 139 (1986).
[8]R. Clampit, K. L. Aitken, and D. K. Jefferies, J. Vac. Sci. Technol. **12**, 1208 (1975); R. Clampit and D. K. Jefferies, Nucl. Instrum. Methods **149**, 739 (1978).
[9]V. E. Krohn and G. R. Ringo, Appl. Phys. Lett. **27**, 479 (1975).
[10]R. L. Seliger, V. W. Ward, V. Wang, and R. L. Kubena, Appl. Phys. Lett. **34**, 510 (1979).
[11]V. Wang, J. W. Ward, and R. L. Seliger, J. Vac. Sci. Technol. **19**, 1158 (1981).
[12]T. Shiokawa, P. H. Kim, K. Toyoda, and S. Namba, J. Vac. Sci. Technol. B **1**, 1117 (1983).
[13]W. L. Brown, T. Venkatesan, and A. Wagner, Nucl. Instrum. Methods **191**, 157 (1981).
[14]R. Levi-Setti, Adv. Electron. Electron Phys. Suppl. A **13**, 261 (1980).
[15]S. Namba, in Proceedings of the International Ion Engineering Congress, Kyoto, Japan, 11–16 Sept. 1983, p. 1533.
[16]P. D. Prewett, Vacuum **34**, 931 (1984).
[17]J. J. Muray, in Proceedings of the International Ion Engineering Congress, Kyoto, Japan, 12–16 Sept. 1983.
[18]A. Wagner, Solid State Technol. **26**, 97 (1983).
[19]A. Wagner, Nucl. Instrum. Methods Phys. Res. **218**, 355 (1983).
[20]R. H. Reuss, Nucl. Instrum. Methods Physics Res. B **10/11**, 515 (1985).
[21]J. J. Muray, Semicond. Int. **7**, 130 (1984).
[22]M. Hassel-Shearer and G. Cogswell, Semicond. Int. **7**, 145 (1984).
[23]J. A. Doherty, B. W. Ward, and E. M. Kellogg, IEEE Trans. Components, Hybrids Manuf. Technol. **6**, 329 (1983).
[24]K. Gamo, K. Yamashita, and S. Namba, in *Microcircuit Engineering 83*, edited by H. Ahmed (Academic, New York, 1983), p. 143.
[25]K. Gamo and S. Namba, Mater. Res. Soc. Proc. **45**, 223 (1985).
[26]M. I. Current and A. Wagner, SPIE **393**, 177 (1983).
[27]J. Melngailis, IEEE Electrotechnol. Rev. **1986**, 58.
[28]*Ion Bombardment Modification of Surfaces*, edited by O. Anciello and R. Kelly (Elsevier, New York, 1984).
[29]*Ion Implantation and Beam Processing*, edited by J. S. Williams and J. M. Poate (Academic, New York, 1984).
[30]*Ion Implantation, Science and Technology*, edited by J. F. Ziegler (Academic, New York, 1984).
[31]*VLSI Technology*, edited by S. M. Sze (McGraw-Hill, New York, 1985).
[32]S. K. Ghandi, *VLSI Fabrication Principles* (Wiley, New York, 1985).
[33]R. Kelley, Radiat. Eff. **32**, 91 (1977); R. P. Webb and D. E. Harrison, Nucl. Instrum. Methods Phys. B **2**, 660 (1984).
[34]W. L. Brown, in *Beam Solid Interactions and Phase Transformations*, edited by H. Kurz, G. L. Olson, and J. M. Poate (North-Holland, Amsterdam, 1986), Vol. 51, p. 53.
[35]R. J. Blackwell, J. A. Kubby, G. N. Lewis, and B. M. Siegel, J. Vac. Sci. Technol. B **3**, 82 (1985), and references therein.
[36]T. Itakura, K. Horiuchi, and S. Yamamoto, Microcircuit Eng. **3**, 153 (1985).
[37]I. Brodie and J. M. Muray, *The Physics of Microfabrication* (Plenum, New York, 1982), p. 137.
[38]G. Benassayag and P. Sudraud, J. Phys. (Paris) Suppl. No. 12 **45**, C9-223 (1984).
[39]N. K. Kang and L. W. Swanson, Appl. Phys. **30**, 95 (1982).
[40]G. L. R. Mair, J. Phys. D **17**, 2323 (1984).
[41]A. Wagner, Appl. Phys. Lett. **40**, 440 (1982).
[42]M. J. Bozack, L. W. Swanson, and J. Orloff, in *Scanning Electron Microscopy* (SEM, Inc., AMF O'Hare, Chicago, IL, 1985), Vol. IV, p. 1339.
[43]N. Anazawa, R. Aihara, M. Okunuki, and R. Shimuzu, in *Scanning Electron Microscopy* (SEM, Inc., AMF O'Hare, Chicago, IL, 1985), Vol. IV, p. 1443.
[44]K. Kurihara, J. Vac. Sci. Technol. B **3**, 41 (1985).
[45]E. Miyauchi, H. Hashimoto, and T. Utsumi, Jpn. J. Appl. Phys. **22**, L225 (1983).
[46]K. Gamo, T. Matsui, and S. Namba, Jpn. Appl. Phys. **22**, L692 (1983).
[47]H. Arimoto, E. Miyauchi, and H. Hashimoto, Jpn. J. Appl. Phys. **24**, L288 (1985).
[48]E. Miyauchi, T. Morita, A. Takamori, H. Arimoto, Y. Bamba, and H. Hashimoto, J. Vac. Sci. Technol. B **4**, 189 (1986).
[49]H. Arimoto, A. Takamori, E. Miyauchi, and H. Hashimoto, J. Vac. Sci. Technol. B **3**, 54 (1986).
[50]W. M. Clark, R. L. Seliger, M. W. Utlaut, A. E. Bell, L. W. Swanson, G. A. Schwind, and J. B. Jergensen, J. Vac. Sci. Technol. B **5**, 197 (1987).
[51]T. Ishitani, K. Umemura, Y. Kawami, and H. Tamura, J. Phys. (Paris) Colloq., Suppl. No. 12 **45**, C9 (1984).
[52]T. Ishitani, K. Umemura, and H. Tamura, Jpn. J. Appl. Phys. **23**, L330 (1984).
[53]T. Ishitani, K. Umemura, S. Hosoki, S. Takayama, and H. Tamura, J. Vac. Sci. Technol. A **2**, 1365 (1984).
[54]Y. Torii and H. Yamada, Jpn. J. Appl. Phys. **22**, L444 (1983).
[55]A. Wagner and T. M. Hall, J. Vac. Sci. Technol. **16**, 1871 (1979).
[56]L. W. Swanson, G. A. Schwind, A. E. Bell, and J. E. Brady, J. Vac. Sci. Technol. **16**, 1864 (1979).
[57]R. J. Culbertson, G. H. Robertson, and T. Sakurai, J. Vac. Sci. Technol. **16**, 1868 (1979).
[58]H. Arimoto, T. Morita, and E. Miyauchi, Jpn. J. Appl. Phys. **25**, L507 (1985).
[59]J. W. Ward, J. Vac. Sci. Technol. B **3**, 207 (1985).
[60]L. W. Swanson, Nucl. Instrum. Methods Phys. Res. **218**, 347 (1983).
[61]L. W. Swanson, in *Electron Optical Systems for Microscopy Microanalysis and Microlithography*, edited by J. Hren, F. Lenz, E. Munro, and P. Sewell (SEM Inc., AMF O'Hare, Chicago, IL, 1984), p. 137.
[62]G. L. R. Maier, R. G. Forbes, R. V. Latham, and T. Mulvey, in *Microcircuit Engineering '83*, edited by H. Ahmed, J. R. A. Cleaver, and G. A. C. Jones (Academic, New York, 1983), p. 171.
[63]G. L. R. Maier and T. Mulvey, in *Scanning Electron Microscopy* (SEM Inc., AMF O'Hare, Chicago, IL, 1985), Vol. III, p. 959.
[64]J. Orloff, Optik **63**, 369 (1983).
[65]E. Munro, in *Image Processing and Computer-aided Design in Electron*

*Optics*, edited by P. W. Hawkes (Academic, New York, 1973), p. 284.
[66]H. Paik, G. N. Lewis, E. J. Kirkland, and B. M. Siegel, J. Vac. Sci. Technol. B **3**, 75 (1985).
[67]W. Thompson, I. Honjo, M. Utlant, and H. Enge, J. Vac. Sci. Technol. B **1**, 1125 (1983).
[68]K. Gamo, Y. Inomoto, Y. Ochiai, and S. Namba, in *Proceedings of the Symposium on Electron and Ion Beam Science and Technology, Tenth International Conference* (Electrochemical Society, Pennington, NJ, 1983), Vol. 83-2, p, 422.
[69]T. Shiokawa, P. H. Kim, K. Toyoda, S. Nama, K. Gamo, R. Aihara, and N. Anazawa, Jpn. J. Appl. Phys. **24**, L566 (1985); H. Sawaragi, R. Aihara, S. Matsui, and K. Mori, J. Vac. Sci. Technol. (to be published).
[70]N. Anazawa, R. Aihara, E. Ban, and M. Okunuki, SPIE Conf. **393**, 137 (1983).
[71]J. R. A. Cleaver, P. J Heard, and H. Ahmed, in *Microcircuit Engineering '83*, edited by H. Ahmed, J. R. A. Cleaver, and G. A. C. Jones (Academic, New York, 1983), p. 135.
[72]R. L. Seliger, J. Appl. Phys. **43**, 2352 (1972).
[73]J. Melngailis (unpublished).
[74]H. P. Kuo, J. Foster, W. Haase, J. Kelly, and B. M. Oliver, in *Proceedings of the Symposium on Electron and Ion Beam Science and Technology* (Electrochemical Society, Pennington, NJ, 1983), p. 78.
[75]W. Thompson, T. Bowe, S. Morlock, A. Moskowitz, and E. Tsiang, SPIE **632**, 85 (1986).
[76]T. H. P. Chang and R. Vishwanathan, J. Vac. Sci. Technol. **15**, 878 (1978).
[77]G. A. C. Jones and G. Owen, in Ref. 76, p. 896.
[78]J. Pasiecnik and J. W. Reeds, in Ref. 76, p. 909.
[79]K. D. Cummings, L. R. Harriott, G. C. Chi, and F. W. Ostermayer, Jr., SPIE **632**, 93 (1986).
[80]J. W. Ward, M. W. Utlaut, and R. L. Kubena, J. Vac. Sci. Technol. B **5**, 169 (1987).
[81]Y. Wada, S. Shukuri, M. Tamura, H. Masada, and T. Ishitani, in Proceedings of the Electrochemical Society Meeting, Las Vegas, Nevada Oct. 1985, p. 133.
[82]J. Melngailis and W. Thompson (unpublished).
[83]H. Morimoto, Y. Sasaki, H. Onoda, and T. Kato, Appl. Phys. Lett. **46**, 898 (1985).
[84]T. Morita, E. Miyauchi, H. Arimoto, A. Takamori, Y. Bamba, and H. Hashimoto, J. Vac. Sci. Technol. B **4**, 829 (1986).
[85]K. Kurihara, Jpn. J. Appl. Phys. **24**, 225 (1985).
[86]F. W. Martin and R. Goloski, Appl. Phys. Lett. **40**, 191 (1982); Nucl. Instrum. Methods **197**, 111 (1982).
[87]F. W. Martin, NSF Report No. ECS 8460351, Nanobeam Corp., Dedham, MA, 1985.
[88]M. R. Smith and E. Munro, J. Vac. Sci. Technol. B **5**, 161 (1987).
[89]J. Orloff and P. Sudraud, Microelectron. Eng. **3**, 161 (1985).
[90]R. L. Kubena, C. L. Anderson, R. L. Seliger, R. A. Jullens, and E. H. Stevens, J. Vac. Sci. Technol. **19**, 916 (1981).
[91]R. L. Kubena, J. Y. M. Lee, R. A. Jullens, R. G. Brault, P. L. Middleton, and E. H. Stevens, IEEE Trans. Electron Devices **31**, 1186 (1984).
[92]R. H. Reuss, D. M. Morgan, E. W. Greeneich, W. M. Clark, and D. B. Rensch, J. Vac. Sci. Technol. B **3**, 62 (1985).
[93]M. Tamura, S. Shukuri, S. Tachi, T. Ishitani, and H. Tamura, Jpn. J. Appl. Phys. **22**, L698 (1983).
[94]E. Miyauchi and H. Hashimoto, Nucl. Instrum. Methods Phys. Res. B **7/8**, 851 (1985).
[95]J. Y. Lee and R. L. Kubena, Appl. Phys. Lett. **48**, 668 (1986).
[96]R. H. Reuss, D. Morgan, and A. Goldenetz, J. Vac. Sci. Technol. B **4**, 290 (1986).
[97]S. D. Chu, J. C. Corelli, and A. J. Steckl, J. Vac. Sci. Technol. B **4**, 375 (1986).
[98]H. Hamadeh, J. C. Corelli, A. J. Steckl, and L. L. Berry, J. Vac. Sci. Technol. B **3**, 91 (1986).
[99]K. Nakamura, T. Nozaki, T. Shiokawa, K. Toyoda, and S. Namba, Jpn. J. Appl. Phys. **24**, L903 (1985).
[100]E. Miyauchi and H. Hashimoto, J. Vac. Sci. Technol. A **4**, 933 (1986).
[101]T. H. Newman and R. F. W. Pease, SPIE **471**, 25 (1984).
[102]D. H. Narum and R. F. W. Pease, J. Vac. Sci. Technol. B **4**, 154 (1986).
[103]Y. Hirayama, Y. Suzuki, S. Tarucha, and H. Okamoto, Jpn. J. Appl. Phys. **24**, L516 (1985).
[104]P. M. Petroff, J. Cibert, G. J. Dolan, S. Pearton, A. C. Gossard, and J. H. English, in Proceedings of the 1986 Materials Research Society Symposium C (North-Holland, New York, to be published), Vol. 76, Paper No. C1.2.
[105]Y. Hirayama, Y. Suzuki, and H. Okamoto, Jpn. J. Appl. Phys. **24**, 1498 (1985).
[106]K. Ishida, K. Matsui, T. Fukunaga, T. Takamori, and H. Nakashima, Jpn. J. Appl. Phys. **25**, L690 (1986).
[107]T. Venkatesan, S. A. Schwartz, D. M. Hwang, R. Bhat, M. Koza, H. W. Yoon, and P. Mei, Appl. Phys. Lett. **49**, 701 (1986).
[108]K. Ishida, T. Takamori, K. Matsui, T. Fukunaga, T. Morita, E. Miyauchi, H. Hashimoto, and H. Nakashima, Jpn. J. Appl. Phys. **25**, L783 (1986).
[109]See for example H. I. Smith, in *Proceedings of the Symposium on Etching for Pattern Definition* (Electrochemical Society, Pennington, NJ, 1976), p. 133; S. Somekh, J. Vac. Sci. Technol. **13**, 1003 (1976).
[110]N. Matsunami, Y. Yamamura, Y. Itikawa, N. Itoh, Y. Kazumata, S. Miyagawa, K. Morita, R. Shimizu, and H. Tawara, At. Data Nucl. Data Tables **31**, 1 (1984).
[111]R. L. Kubena, R. L. Seliger, and E. H. Stevens, Thin Solid Films **92**, 165 (1982).
[112]H. Yamaguchi, A. Shimase, S. Haraichi, and T. Miyauchi, J. Vac. Sci. Technol. B **3**, 71 (1985).
[113]H. Morimoto, Y. Sasaki, Y. Watakabe, and T. Kato, J. Appl. Phys. **57**, 159 (1985).
[114]P. J. Heard, J. R. A. Cleaver, and H. Ahmed, J. Vac. Sci. Technol. B **3** (1985).
[115]J. Melngailis, C. R. Musil, E. H. Stevens, M. Utlaut, E. M. Kellogg, R. T. Post, M. W. Geis, and R. W. Mountain, J. Vac. Sci. Technol. B **4**, 176 (1986).
[116]A. Wagner, Nucl. Instrum. Methods Phys. Res. **218**, 355 (1985).
[117]J. R. A. Cleaver, H. Ahmed, P. J. Heard, P. D. Prewett, G. J. Dunn, and H. Kaufman, Microelectron. Eng. **3**, 253 (1985).
[118]H. C. Kaufman, W. B. Thompson, and G. J. Dunn, SPIE **632**, 60 (1986).
[119]M. Yamamoto, M. Sato, H. Kyogoku, K. Aita, Y. Nakagawa, A. Yasaka, R. Takasawa, and O. Hattori, SPIE **632**, 97 (1986).
[120]J. Melngailis (unpublished).
[121]A. Wagner, in Proceedings of the 1986 Materials Research Society Symposium B and C (North-Holland, New York, to be published), Vols. 75 and 76, Paper No. B-C1.4.
[122]D. K. Atwood, G. J. Fisanick, W. A. Johnson, and A. Wagner, SPIE **471**, 127 (1984).
[123]H. Betz, A. Heuberger, N. P. Economou, and D. C. Shaver, SPIE **632**, 67 (1986).
[124]T. Ishitani, Y. Kawanami, and H. Todokoro, Jpn. J. Appl. Phys. **24**, L133 (1985).
[125]L. R. Harriott, A. Wagner, and F. Fritz, J. Vac. Sci. Technol. B **4**, 185 (1986).
[126]D. C. Shaver and B. W. Ward, J. Vac. Sci. Technol. B **4**, 185 (1986).
[127]C. R. Musil, J. L. Bartelt, and J. Melngailis, IEEE Electron Devices Lett. **7**, 285 (1986).
[128]J. Puretz, J. Orloff, and L. Swanson, SPIE **471**, 38 (1984).
[129]L. R. Harriott, R. E. Scotti, K. D. Cummings, and A. F. Ambrose, Appl. Phys. Lett. **48**, 1704 (1986).
[130]J. Puretz, R. K. DeFreez, R. A. Elliott, and J. Orloff, Electron. Lett. **22**, 700 (1986).
[131]R. K. DeFreez, J. Puretz, R. H. Elliott, J. Orloff, and L. W. Swanson, Electron. Lett. **22**, 919 (1986).
[132]L. R. Harriott, R. E. Scotti, K. D. Cummings, and A. F. Ambrose, J. Vac. Sci. Technol. B **5**, 207 (1987).
[133]For a review of laser-microchemical processing see, for example, D. J. Ehrlich and J. Y. Tsao, J. Vac. Sci. Technol. B **1**, 969 (1983).
[134]S. Matsui and K. Mori, J. Vac. Sci. Technol. B **4**, 299 (1986).
[135]Y. Ochiai, K. Gamo, and S. Namba, J. Vac. Sci. Technol. B **3**, 67 (1985).
[136]Y. Ochiai, K. Shihoyama, T. Shiokawa, K. Toyoda, A. Masuyama, K. Gamo, and S. Namba, J. Vac. Sci. Technol. B **4**, 333 (1986).
[137]K. Gamo, N Takakura, N. Samoto, R. Shimizu, and S. Namba, Jpn. J. Appl. Phys. **23**, L293 (1984).
[138]K. Gamo, N. Takakura, D. Takehara, and S. Namba, Extended Abstract 16th International Conference on Solid State Devices and Materials (Kobe, Japan, 1984), p. 31.

[139]K. Gamo and S. Namba, in *Proceedings of Symposium on Reduced Temperature Processing for VLSI* (Electrochemical Society, Pennington, NJ, 1986), Vol. 86-5.
[140]D. J. Ehrlich, J. Y. Tsao, and C. O. Bozler, J. Vac. Sci. Technol. B **3**, 1 (1985).
[141]H. Lezec and J. Melngailis (unpublished).
[142]G. M. Shedd, A. D. Dubner, H. Lezec, and J. Melngailis, Appl. Phys. Lett. **49**, 1584 (1986).
[143]J. E. Jensen, Solid State Technol. **27**, 145 (1984).
[144]M. Komuro, N. Atoda, and H. Kawakatsu, J. Electrochem. Soc. **126**, 483 (1979).
[145]H. Ryssel, H. Kranz, K. Haberger, and J. Bosch, in *Microcircuit Engineering 80*, edited by R. P. Kramer (Delft U. P., The Netherlands, 1981), p. 293. H. Ryssel, K. Haberger, and H. Kranz, J. Vac. Sci. Technol. **9**, 1358 (1981).
[146]For a review of resists and e-beam lithography see, for example, *Introduction to Microlithography*, edited by L. F. Thompson, C. G. Wilson, and M. J. Bowden (American Chemical Society, Washington, DC, 1983).
[147]A. Macrander, D. Barr, and A. Wagner, SPIE **33**, 142 (1982).
[148]H. Ryssel, G. Prinke, H. Bernt, K. Haberger, and K. Hoffmann, Appl. Phys. **27**, 239 (1982).
[149]S. Matsui, K. Mori, K. Saigo, T. Shiokawa, K. Toyoda, and S. Namba, J. Vac. Sci. Technol. B **4**, 845 (1986).
[150]D. F. Reich, D. J. Fray, A. F. Evanson, J. R. H. Cleaver, and H. Ahmed, Microcircuit Eng. **5**, 171 (1986).
[151]T. Shiokawa, Y. Aoyagi, P. H. Kim, K. Toyoda, and S. Namba, Jpn. J. Appl. Phys. **23**, L232 (1984).
[152]S. Matsui, J. Vac. Sci. Technol. (to be published).
[153]H. I. Smith, J. Vac. Sci. Technol. B **4**, 148 (1986).
[154]Ph. David and L. Karapiperis, Microelectron. Eng. **3**, 178 (1985).
[155]H. Morimoto, H. Onoda, Takaaki Kato, Y. Sasaki, K. Saitoh, and Tadao Kato, J. Vac. Sci. Technol. B **4**, 205 (1986).
[156]H. Kuwano, J. Appl. Phys. **55**, 1149 (1984).
[157]T. Kato, H. Morimoto, K. Tsukamoto, H. Shinohara, and M. Inuishi, in Proceedings of the VLSI Symposium, 15 May 1985, Kobe, Japan, p. 72.
[158]K. Gamo, K. Moriizumi, Y. Ochiai, M. Takai, S. Namba, T. Shiokawa, and T. Minamisono, Jpn. J. Appl. Phys. **23**, L642 (1984).
[159]M. Komuro, H. Hiroshima, H. Tanoue, and T. Kanayuama, J. Vac. Sci. Technol. B **1**, 985 (1983).
[160]M. Komuro, T. Kanayama, H. Hiroshima, and H. Tanoue, Appl. Phys. Lett. **42**, 908 (1983).
[161]K. Gamo, G. Huang, K. Moriizumi, N. Samoto, R. Shimizu, and S. Namba, Nucl. Instrum. Methods Phys. Res. B **7/8**, 864 (1985).
[162]J. Melngailis, D. J. Ehrlich, J. Randal, and S. Pang, J. Vac. Sci. Technol. B **5**, 379 (1987).
[163]K. D. Cummings, L. R. Harriott, G. C. Chi, and F. W. Ostermayer, Jr., Appl. Phys. Lett. **48**, 659 (1986).
[164]J. R. A. Cleaver, P. J. Heard, A. F. Evason, and H. Ahmed. Appl. Phys. Lett. **49**, 654 (1986).
[165]A. Milgram and J. Puretz, J. Vac. Sci. Technol. B **3**, 879 (1985).
[166]R. Levi-Setti, G. Crow, and Y. L. Wang, *Scanning Electron Microscopy* (SEM Inc., AMF O'Hare, Chicago, IL, 1985), p. 535.
[167]R. Levi-Setti, Y. L. Wang, and G. Crow, J. Phys. (Paris) Colloq. Suppl. No. 12 **45**, C9-197 (1984).
[168]A. R. Bayly, A. R. Waugh, and K. Anderson, Nucl. Instrum. Methods Phys. Res. **218**, 375 (1983).
[169]A. R. Waugh, A. R. Bayly, and K. Anderson, Vacuum **34**, 103 (1984).
[170]N. W. Parker, W. P. Robinson, and J. M. Snyder, SPIE **632**, 76 (1986).
[171]R. Levi-Setti *et al.*, Phys. Rev. Lett. **54**, 2615 (1985).
[172]P. D. Prewett, Vacuum **34**, 931 (1984).
[173]G. Stengl, H. Loschner, W. Maurer, and P. Wolf, J. Vac. Sci. Technol. B **4**, 194 (1986).
[174]M. R. McMillan, NSF Final Project Report NSF Award No. 84600864 (National Science Foundation, Washington, DC, 1985).

Appendix II

EDL/9/9//23208

# A Tunable-Frequency Gunn Diode Fabricated by Focused Ion-Beam Implantation

**Henri J. Lezec**
**Khalid Ismail**
**Leonard J. Mahoney**
**Mark I. Shepard**
**Dimitri A. Antoniadis**
**John Melngailis**

**Reprinted from**
**IEEE ELECTRON DEVICE LETTERS**
**Vol. 9, No. 9, September 1988**

# A Tunable-Frequency Gunn Diode Fabricated by Focused Ion-Beam Implantation

HENRI J. LEZEC, KHALID ISMAIL, LEONARD J. MAHONEY, MARK I. SHEPARD, MEMBER, IEEE, DIMITRI A. ANTONIADIS, SENIOR MEMBER, IEEE, AND JOHN MELNGAILIS, SENIOR MEMBER, IEEE

*Abstract*—**We report the fabrication of a planar Gunn diode in which the fundamental transit-time mode oscillation frequency can be tuned over the range 6–23 GHz by varying the dc bias across the device. The wide-band tunability is due to a linear doping concentration gradient between the contacts. This lateral doping profile was created by implanting the device with a focused beam of silicon ions and smoothly increasing the dose from contact to contact. A Gunn diode with a uniform active region, also fabricated with the focused ion beam, displays a relatively constant oscillation frequency in the same bias range.**

## I. Introduction

GaAs GUNN diodes are one of the most important solid-state sources of microwave power. Frequency tuning over a limited range is usually obtained in resonant circuits where a Gunn diode may operate in different modes of oscillation. Tuning is produced with an external device either mechanically, by varying the dimensions of a resonant cavity, or electronically using varactor diodes or ferrimagnetic material, particularly YIG spheres.

In 1967, Sandbank [1] and Shoji [2] proposed a Gunn diode with a transit-time mode frequency that is directly tunable with bias voltage. This effect can be obtained by smoothly increasing either the doping concentration or the cross section of the device from cathode to anode. Since a technology that allows precise control of lateral or vertical doping profiles was not available at the time, Gunn diodes with nonuniform cross sections were built instead. Tapered Gunn diodes [1], [2] and Gunn diodes with concentric electrodes [3]–[5] have displayed wide-band frequency tunability when connected to nonresonant resistive loads. For example, a planar Gunn diode with concentric electrodes was tunable with bias voltage over a range of 6.6–18 GHz [4].

With the recent advent of focused ion-beam technology, it becomes possible to implant planar structures with laterally graded doping profiles (for a review of the field of focused ion-beam technology see [6]). In our focused ion-beam system, ions of common semiconductor dopants can be accelerated up to 300 keV (if doubly ionized), focused down to a 0.1-$\mu$m spot size, and deflected under computer control for local implantation of arbitrary geometries. By modifying the exposure time per pixel as the beam is scanned along the surface of a wafer, smoothly varying lateral doping profiles can be achieved. We report the first use of this doping technique to build a planar tunable-frequency Gunn diode.

A vertical tunable-frequency Gunn diode could be built by grading the doping concentration of the active layer during epitaxial growth. The technology has already been demonstrated: using molecular beam epitaxy, Ondria and Ross [7] improved the operation of GaAs Gunn diodes by grading the active region doping profiles to minimize temperature gradients.

A distinct advantage of *planar* tunable-frequency Gunn diodes fabricated by focused ion-beam implantation is that they can be integrated directly into monolithic circuits. In addition, diodes with different lateral doping profiles and frequency versus bias characteristics can be defined on the same wafer or in the same circuit.

## II. Principle of Operation

In a uniformly doped device, the fundamental transit-time frequency of oscillation is determined by the time it takes for the dipole domain to propagate from the cathode, where it nucleates, to the anode, where it discharges. The frequency is inversely proportional to this time and is relatively constant as a function of applied field.

In a device in which the doping level increases from cathode to anode, the applied electric field decreases from cathode to anode. The length over which the electric field exceeds the domain sustaining value $E_s \simeq 2$ kV/cm defines the length of repeated travel of the domain. When a domain reaches the point at which the field has dropped to $E_s$ it dissolves, and a new domain is nucleated at the cathode. By varying the bias voltage, this point can be shifted across the sample, thus allowing control of the transit-time frequency [8]. When the bias across the device is increased, for example, the point at which the field has dropped to $E_s$ moves toward the anode; the transit length and transit time increase and the frequency of oscillation decreases.

## III. Fabrication

Semi-insulating GaAs was first implanted with a 140-keV, 25-pA, $Si^{++}$ focused ion beam. The beam diameter was estimated to be about 0.15 $\mu$m from the resolution obtained while imaging a free-standing gold grating of 0.1-$\mu$m-wide lines. The planar implant geometry is shown in Fig. 1(a). The

Manuscript received May 11, 1988; revised July 8, 1988. This work was supported by DARPA/DOD under Contract MDA 903-85-C-0215 at M.I.T. and by the Department of the Air Force at Lincoln Laboratory.

H. J. Lezec, K. Ismail, M. I. Shepard, and D. A. Antoniadis are with the Department of Electrical Engineering and Computer Science, Massachusetts Institute of Technology, Cambridge, MA 02139.

L. J. Mahoney is with Lincoln Laboratory, Massachusetts Institute of Technology, Lexington, MA 02173.

J. Melngailis is with the Research Laboratory of Electronics, Massachusetts Institute of Technology, Cambridge, MA 02139.

IEEE Log Number 8823208.

0741-3106/88/0900-0476$01.00 © 1988 IEEE

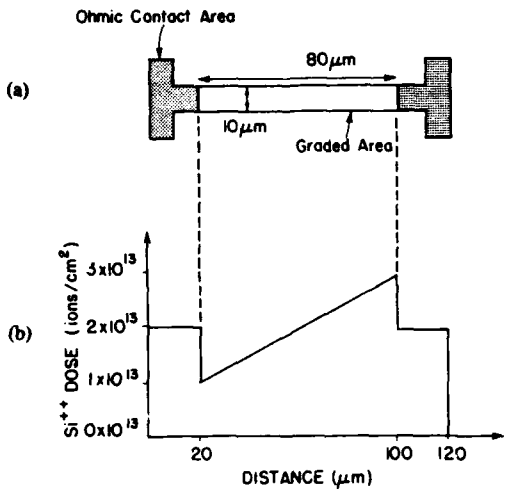


Fig. 1. (a) Focused ion-beam planar implant geometry. (b) Lateral dose profile.

focused ion beam was used to implant both the ohmic contact areas and the active area where the Gunn domains propagate. The ohmic contact areas were given a uniform dose of $2 \times 10^{13}$ ions $cm^{-2}$. The width of the active region was 10 $\mu$m, and the length was 80 $\mu$m. Implants were performed with respect to alignment marks etched into the wafer. The pattern array was previously specified on a CAD system and implanted under computer control. One particular doping profile is shown in Fig. 1(b): the dose was varied linearly from $10^{13}$ to $3 \times 10^{13}$ $cm^{-2}$ over the 80 $\mu$m length of the active region. This profile was obtained by vectoring the beam with increasing dwell time from one ohmic contact to the other. A pixel spacing of 0.05 $\mu$m was chosen to produce a smoothly varying profile.

The implant was annealed at 850°C for 20 min with a cap consisting of 700 Å of $Si_3N_4$ and 3000 Å of $SiO_2$. Ni/Ge/Au ohmic contacts were defined using optical lithography and lift-off, and annealed for 30 s at 450°C.

The processed GaAs wafer was diced, and individual devices were heat-sunk and wire-bonded to 50-Ω microstrip test fixtures.

## IV. Results

The instrumentation for measuring the current oscillation frequency is shown in Fig. 2. Each device is dc biased using an HP 11612A bias network, and the frequency spectrum and power level are measured with an HP 8566A spectrum analyzer. No attempt was made to match the impedance of the device to the 50-Ω load.

A voltage on the order of 20–25 V is typically required to induce transit-time mode Gunn oscillations in the 80-$\mu$m-long devices. At lower applied voltages, the peak electric field in the device is everywhere below the threshold for domain nucleation ($\simeq 3$ kV/cm), and oscillations do not occur.

A device with a uniform active region dose of $10^{13}$ $cm^{-2}$ oscillates at 1.6 GHz at a bias of 34 V. The fundamental mode power into the 50-Ω load is $-10$ dBm or 0.1 mW. The oscillation frequency shows a relatively weak dependence on bias: it drops to 1.57 GHz when the bias is raised to 37 V. This

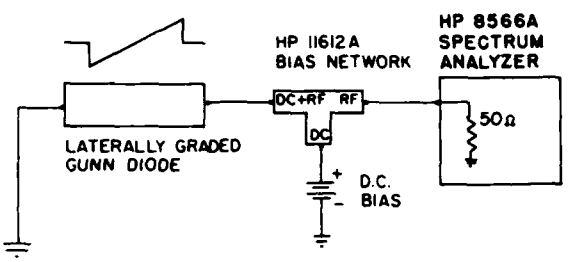


Fig. 2. Frequency measurement instrumentation.

weak $-10$-MHz/V dependence results from the decrease of domain velocity at higher electric fields.

In contrast, a device with the lateral doping gradient of Fig. 1(b) displays a very strong dependence of frequency on bias. The frequency is smoothly tunable with dc bias over a 17-GHz range. This dependence is displayed in Fig. 3(a). As the bias across the device is increased from 26 to 37 V, the frequency decreases smoothly from 23 to 6 GHz. A maximum dependence of $-5.1$ GHz/V is obtained around a bias of 26.5 V. The device does not oscillate for biases below 26 V, and the oscillation power decays rapidly to negligible levels for biases above 37 V.

Assuming a constant domain velocity $v = 10^7$ cm/s, the domain propagation length $l$ in the laterally graded device at a given bias can be estimated from the frequency $f = v/l$. As the bias is increased from 26 to 37 V, $l$ is found to increase linearly from 4 to 17 $\mu$m. Thus only the initial portion of the device contributes to the variable frequency effect. A shorter device would be preferable, presenting less parasitic resistance and allowing operating bias levels four to five times lower.

A composite power spectrum for the fundamental oscillation mode of the laterally graded device is shown at a few discrete voltage levels in Fig. 3(b). A full width at half-maximum of 10 MHz and a signal-to-noise ratio of 30 dB is obtained over most of the tunability range. The power into the 50-Ω load ranges from a minimum of $-47$ dBm at 26 V to a maximum of $-38$ dBm at 30 V. The power levels are low because of the parasitic series resistance and the absence of a matching circuit.

We have conducted some preliminary numerical simulations of laterally graded Gunn diodes using a transient energy model derived from Boltzmann's transport equation in the relaxation time approximation. The same model has been previously used to optimize the doping profile of GaAs MESFET's [9]. The solution is performed in the time domain and allows us to observe domain nucleation, motion, and discharge. As the bias voltage is increased, a given domain is observed to travel a longer distance into the anode region before a second domain is triggered at the cathode, quenching the first one. We have used this program to model the performance of the 80-$\mu$m graded device of Fig. 1. To minimize computational time in assessing the range over which the frequency can be tuned, only the initial 30 $\mu$m of the graded region on the cathode side was included in the model. This approach is valid since the domain remains well within that portion of the device at all times and biases: the simulated range of travel approaches an asymptotic limit of 20 $\mu$m as the

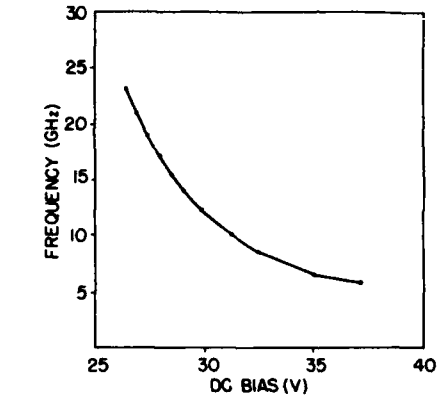


(a)

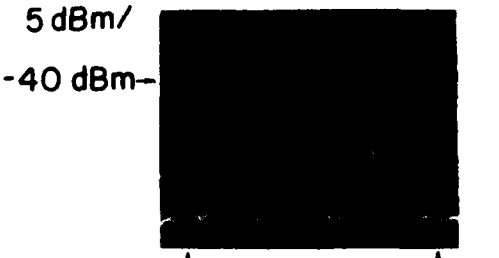


(b)

Fig. 3. (a) Frequency versus voltage curve of the device of Fig. 1. (b) Spectrum composite.

bias is increased. The simulated frequency of oscillation decreases from a maximum of 28 GHz at the onset of oscillation at low bias to an asymptotic limit of 5 GHz at high biases. This is in good agreement with the experimental data of Fig. 3(a). The program is now being used to predict the effect of other doping profiles on the tunability characteristics. For example, a device with a logarithmic doping profile (steep at the cathode and gradually flattening out towards the anode) displays increased tunability compared to a device with a linear doping profile and the same endpoint doping concentrations.

## V. Conclusion

A tunable-frequency Gunn diode has been fabricated with the novel capability of the focused ion beam to implant a lateral doping gradient. The frequency can be tuned over a wide range by varying the dc bias across the device. No adjustment of resonant cavities or tuning of external circuits is required. The planar configuration of this tunable oscillator makes it ideally suited for integration into monolithic GaAs circuits. This device could prove to be useful as a wide-band voltage-controlled oscillator in a number of applications such as collision-avoidance radar.

## Acknowledgment

The authors wish to thank R. A. Murphy, C.-L. Chen, and E. Brown of Lincoln Laboratory, and A. Chu of M/A-COM for helpful discussions. They also wish to thank D. Landers of Lincoln Laboratory for assistance in device packaging, and G. Stevens and M. Utlaut of Hughes, and M. Nasser-Ghodsi of Angenics for advice on focused ion-beam system operation. The liquid metal ion source was provided by Hughes Research Laboratories.

## References

[1] C. P. Sandbank, "Synthesis of complex electronic functions by solid state bulk effects," *Solid-State Electron.*, vol. 10, pp. 369–380, 1967.

[2] M. Shoji, "Functional bulk semiconductor oscillators," *IEEE Trans. Electron Devices*, vol. ED-14, no. 9, pp. 535–546, Sept. 1967.

[3] B. Jeppson, I. Marklund, and K. Olsson, "Voltage tuning of concentric planar Gunn diodes," *Electron. Lett.*, vol. 3, no. 11, pp. 498–500, Nov. 1967.

[4] G. M. Clarke, A. L. Elridge, and J. C. Bass, "Planar Gunn-effect oscillators with concentric electrodes," *Electron. Lett.*, vol. 5, no. 20, pp. 471–472, Oct. 1969

[5] C. O. Newton and G. Bew, "Frequency measurements on Gunn effect devices with concentric electrodes," *J. Phys. D: Appl. Phys.*, vol. 3, pp. 1189–1198, 1970.

[6] J. Melngailis, "Focused ion beam technology and applications," *J. Vac. Sci. Technol.*, vol. 5, no. 2, pp. 469–495, Mar./Apr. 1987.

[7] J. Ondria and R. Ross, "Improved performance of fundamental and second harmonic MMW oscillators through active device doping concentration contouring," in *IEEE MTT-S Dig.*, 1987, pp. 977–980.

[8] B. G. Bosch and R. W. Engelman, *Gunn-Effect Electronics*. New York: Wiley, 1975, p. 372.

[9] K. Ismail, O. L. El-Sayed, and G. Salmer, "Doping profile optimization in GaAs MESFETs," presented at the 15th ESSDERC, Aachen, W. Germany, Sept. 1985.

# Simulation of Implantation and Diffusion of Profiles Made with a Focused Ion-Beam Implanter

REX E. LOWTHER, JARVIS B. JACOBS, AND DIMITRI A. ANTONIADIS

*Abstract*—A method is presented by which two-dimensional profiles made with a focused ion-beam implanter are quickly and easily calculated. Advantage is taken of the Gaussian nature of the beam and its interaction with the target to represent the dose versus position as a sum of Gaussian functions spaced along the beam path. The vertical profile, taken either from measured data or from a one-dimensional simulation, is also fit to a sum of Gaussian functions. With this form, and assuming uniform diffusivity, subsequent diffusion steps can be modeled as a simple increase in the standard deviation of the Gaussian functions—eliminating the need to step in time. A method for satisfying the boundary condition at the surface and for modeling a variable oxide thickness on this surface is also demonstrated.

SINCE FOCUSED ion-beam (FIB) implanters allow for control of dopant profiles in the lateral direction, simulation of these profiles must be at least two-dimensional. Conventional 2-D numerical simulation of subsequent diffusion steps can be very computationally intensive because it involves discretization in both spatial dimensions and in time. The method described here greatly reduces this computational expense by eliminating the need to step in time. For most device applications, where the FIB will be used to tailor dopant profiles in the device active region, the dopant concentrations will usually be low enough so that diffusivity can be approximated as uniform. On this assumption, the initial implanted profile is fitted to a sum of Gaussian basis functions. Since a Gaussian-shaped profile will, upon uniform diffusion, remain Gaussian, the diffusion steps are modeled by merely increasing the variance of these functions.

For practical reasons the FIB energy is not changed during a scan, since this would require refocusing of the beam. If we make the further assumption (to be relaxed later) of uniform oxide thickness on the silicon surface, the two-dimensional problem becomes separable into two one-dimensional problems. The concentration $C(x, y)$ in this case is approximately the product of the lateral profile $X(x)$ and the vertical profile $Y(y)$. In the lateral direction, the nature of the FIB readily lends itself to the method of fitting the dose (in atoms per square centimeter) as a function of position to a sum of Gaussian functions with centers spaced along the path of the beam. It is accepted that both the lateral spread of the FIB before hitting the target [1] and the lateral spread of an infinitely thin beam after hitting the target [2], [3] can be described accurately enough as Gaussian. (The magnitude of the former must be determined for each machine while the latter is available in the literature, e.g., [4].) The resultant lateral (parallel to the surface) profile produced by aiming the FIB implanter at one spot is then another Gaussian with a variance equal to the sums of these variances. The coefficient of each Gaussian is therefore proportional to the dose received when the beam is aimed at the center of that Gaussian. This dose is determined by linear interpolation from a table of positions and doses supplied by the user. Fig. 1 shows the function $X(x)$ for several scans for which the FIB intensity $I(x)$ (in units of atoms per square centimeters) is varied according to

$$I(x) = \begin{cases} 1.0\text{E}15, & x \le 0.5 - \Delta \\ 0.5\text{E}15\,[1 + (0.5 - x)/\Delta], & 0.5 - \Delta < x > 0.5 + \Delta \\ 0.0, & x \ge 0.5 + \Delta \end{cases} \quad (1)$$

with

$$\Delta = 0.0, 0.1, 0.2, 0.3\ \mu\text{m}.$$

For demonstrational reasons, the FIB lateral standard deviation used here, including the spread after hitting the target, is set at 0.1 $\mu$m. Note that in the special case $\Delta = 0.0$, $X(x)$ is, by definition, a complementary error function—the function often used to model profiles at a mask edge.

Measurements [1] have shown that the beam distribution before hitting the target is fitted quite well by a Gaussian function within two decades of the peak value. At three decades, however, the ion concentration is significantly greater than that predicted from a fit by a single Gaussian. As mentioned above, we have chosen to ignore this departure because it is small and because accurate beam measurements are not yet available. If, however, a more accurate treatment is desired, each Gaussian function used above can be replaced by a sum of just two or

Manuscript received September 9, 1985; revised February 18, 1986. This work was supported by DARPA under Contract MDA903-85-C-0125. J. B. Jacobs was supported under a grant from the National Consortium for Graduate Degrees for Minorities in Engineering, Inc.

R. E. Lowther is with Harris Semiconductor, Melbourne, FL 32901.

J. B. Jacobs and D. A. Antoniadis are with the Department of Computer Science and Electrical Engineering, Massachusetts Institute of Technology, Cambridge, MA 02139.

IEEE Log Number 8609161.

0018-9383/86/0900-1251$01.00 © 1986 IEEE

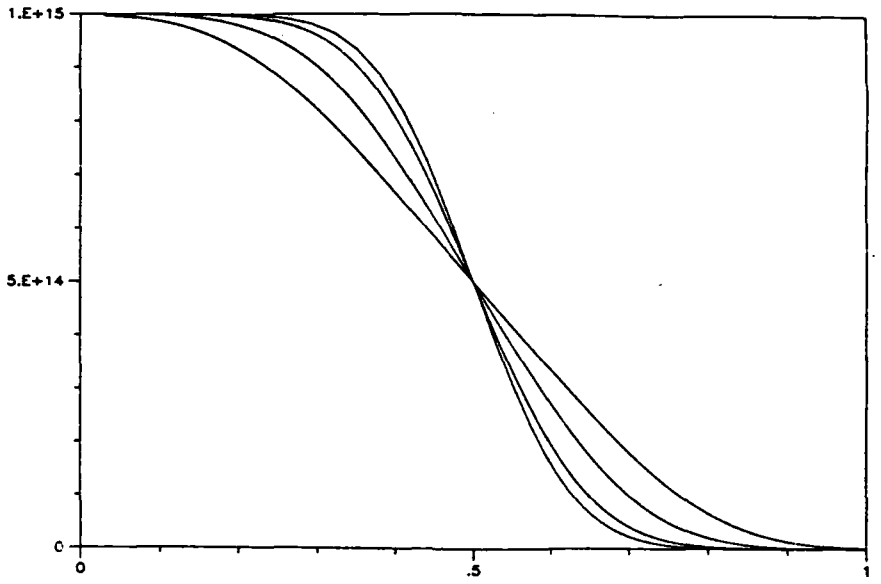


Fig. 1. Dose (in atoms per square centimeter) versus position (in micrometers) for the beam scans defined in (1).

three Gaussians with identical positions but differing variances. In this case, it is the near-Gaussian shape of the FIB that allows for the small number of terms in the sum.

In the vertical direction, perpendicular to the surface, the initial profile is input either as a table or as a set of moments of a Pearson IV distribution. These data may either describe the vertical profile before, after, or between the subsequent diffusion steps and also may be taken from the output of a one-dimensional process simulator. For diffusion steps already modeled in the initial vertical profile, these steps model the lateral diffusion only.

If vertical diffusion is also simulated by this method, the experimental profile, $Y(y)$, is fitted to a sum of Gaussian functions

$$Y(y) = \sum_j c_j \exp\left[-(y - y_j)^2/2\sigma^2\right] \tag{2}$$

where the $y_j$'s are equally spaced. Since $\sigma$ is made small compared to any other features in the profile, it can be assumed as a first approximation that the coefficients are strictly proportional to $Y(y)$

$$c_i = \alpha Y(y_i). \tag{3}$$

By substituting this into (2) at $y = y_i$ to solve for $\alpha$, we get

$$c_i = \frac{Y^2(y_i)}{\sum_j Y(y_j) \exp\left[-(y_i - y_j)^2/2\sigma^2\right]} \tag{4}$$

which is the form used to calculate $c_i$ when the profile is read from a table. If the function $Y(y)$ is an analytic function, then $Y(y)$ may be moved inside the exponential and $\ln Y$ expanded about $y_i$ in a Taylor series

$$c_i = \frac{Y(y_i)}{\sum_j \exp\left[-(y_j - y_i)^2/2\sigma^2 + (y_j - y_i)\left.\frac{d \ln Y}{dy}\right|_{y=y_i} + \frac{1}{2}(y_j - y_i)^2 \left.\frac{d^2 \ln Y}{dy}\right|_{y=y_i}\right]}. \tag{5}$$

This fit is fast and is achieved without solving a set of matrix equations or allowing any negative coefficients, $c_i$.

The boundary condition used at the silicon interface ($y = 0$) is a generalization of the reflective boundary condition used in [3]

$$Y(y) = Y_d(y) + r[Y_d(-y) - Y_0(-y)] \tag{6}$$

where

$$Y_0(y) = \sum_i c_i \exp\left[-(y - y_i)^2/2\sigma^2\right] \tag{7a}$$

$$Y_d(y) = \frac{\sigma}{(\sigma^2 + 2Dt)^{1/2}} \cdot \sum_i c_i \exp\left[-(y - y_i)^2/(2\sigma^2 + 4Dt)\right] \tag{7b}$$

and $t$ is the diffusion time and $D$ is the uniform dopant diffusivity. For the case where the surface concentration after diffusion is much less than the peak concentration, setting $r$ to one accurately describes the reflective boundary condition. At the other extreme, if $Y_d(y)$ has its peak at the surface, then setting $r$ to zero also is good for modeling the reflective boundary condition. The coefficient $r$ is therefore bounded by 0 and 1 and is determined by the ratio of $Y_d(0)$ to $Y_d(y = \text{peak})$. Finally, for very long diffusion times, the term $Y_o(-y)$ in (6) can dominate. To prevent this without noticeable effect on results at shorter diffusion times, the Gaussians in this term are also given a fraction of the diffusive spreading found in the $Y_d$ terms. Fig. 2 shows results of a fit (solid line) to a Pearson IV

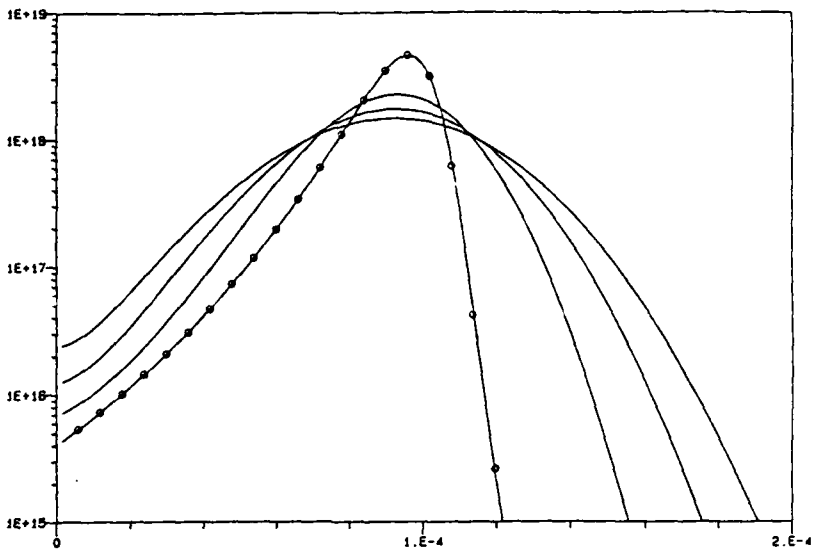


Fig. 2. Boron concentration (in atoms per cubic centimeter) versus distance (in micrometers) from the surface. Shown here is a fit (solid line) to measurements for boron implanted into polysilicon at 400 keV (circles). Also shown are the distributions after three diffusion steps, equally spaced in time.

function (circles) representing boron implanted into polysilicon at 400 keV [5]. Also shown here are the distributions after three diffusion steps, equally spaced in time.

If the beam is scanned along regions of varying oxide thickness, the problem again becomes two-dimensional. In this case, the concentration $C(x, y)$ at point $(x, y)$ is approximated as a superposition from ions implanted through the oxide thicknesses found within the lateral range of position $(x, y)$

$$C(x, y) \cong X(x) \int \exp\left[-(x' - x)^2/2\sigma_x^2\right] \cdot \{Y_d[y + st_{ox}(x')] + rY_d[-y + (2 - s)\, t_{ox}(x')] - rY_0[-y + (2 - s)\, t_{ox}(x')]\}\, dx' \Big/ \int \exp\left[-(x' - x)^2/2\sigma_x^2\right] dx' \qquad (8)$$

where $\sigma_x$ is the final lateral spread from a beam aimed at one spot, and $t_{ox}(x')$ is the oxide thickness at point $x'$. The variable $s$ is determined from the ratio of the stopping power of oxide to silicon and by the geometry of encroachment of oxide into the silicon. This simple translation of the vertical profile assumes that the shape of the vertical profile is not significantly affected by variations in the oxide thickness (see [6]). Computationally, the integral in (8) is converted to a sum. Thus, for each point $(x, y)$, the function $Y(y)$ (which has a sum of its own) must be within an additional summation sign. To alleviate much of this expense, $Y_o(y)$ and $Y_d(y)$ can be tabulated so that a simple interpolation (rather than a sum over Gaussians) is needed to evaluate them. Furthermore, at each value of $x$, the minimum number of points $(x')$ needed to accurately evaluate (8) is calculated. Since they do not depend on $Y(y)$, values of the lateral Gaussian weight functions in (8) are also stored at this time. Note that, since $X(x)$ is outside the summation [or integral sign in (8)] and since $Y_o(y)$ and $Y_d(y)$ are tabulated, the computation time is only slightly dependent on the number of Gaussian functions used to fit these functions. Typically, 10 to 100 terms are necessary to make the discretization error negligible although as many as 1000 would still have a small effect on the total computation time. Results near a strongly tapered oxide edge for boron implanted into crystalline silicon at 30 keV and with an initial lateral sigma of 0.1 $\mu$m are shown in Fig. 3(a) (before diffusion) and Fig. 3(b) (after diffusion). The initial vertical profiles used here are from [7].

In conclusion, a method is described that quickly and accurately describes two-dimensional profiles made with a focused ion-beam implanter. Advantage is taken of the availability in the literature (e.g., [4]) of accurate one-dimensional implantation profiles and of the nature of the ion beam which allows the dose to be easily described as a sum of Gaussian functions. Simulation of the subsequent diffusion steps is made easy by use of the Gaussian form although this also limits the simulation to cases in which the diffusivity can be assumed uniform. By starting with a one-dimensional simulation that has already modeled the diffusion steps, the above assumption can be relaxed to the assumption of uniform lateral diffusivity and of dose-independent vertical diffusivity. In this case, two-dimensional profiles including both variations in dose and oxide thickness can still be obtained by applying the methods described above. The only computational difference, in this case, is that the variance due to diffusion is not added to the vertical Gaussian basis function.

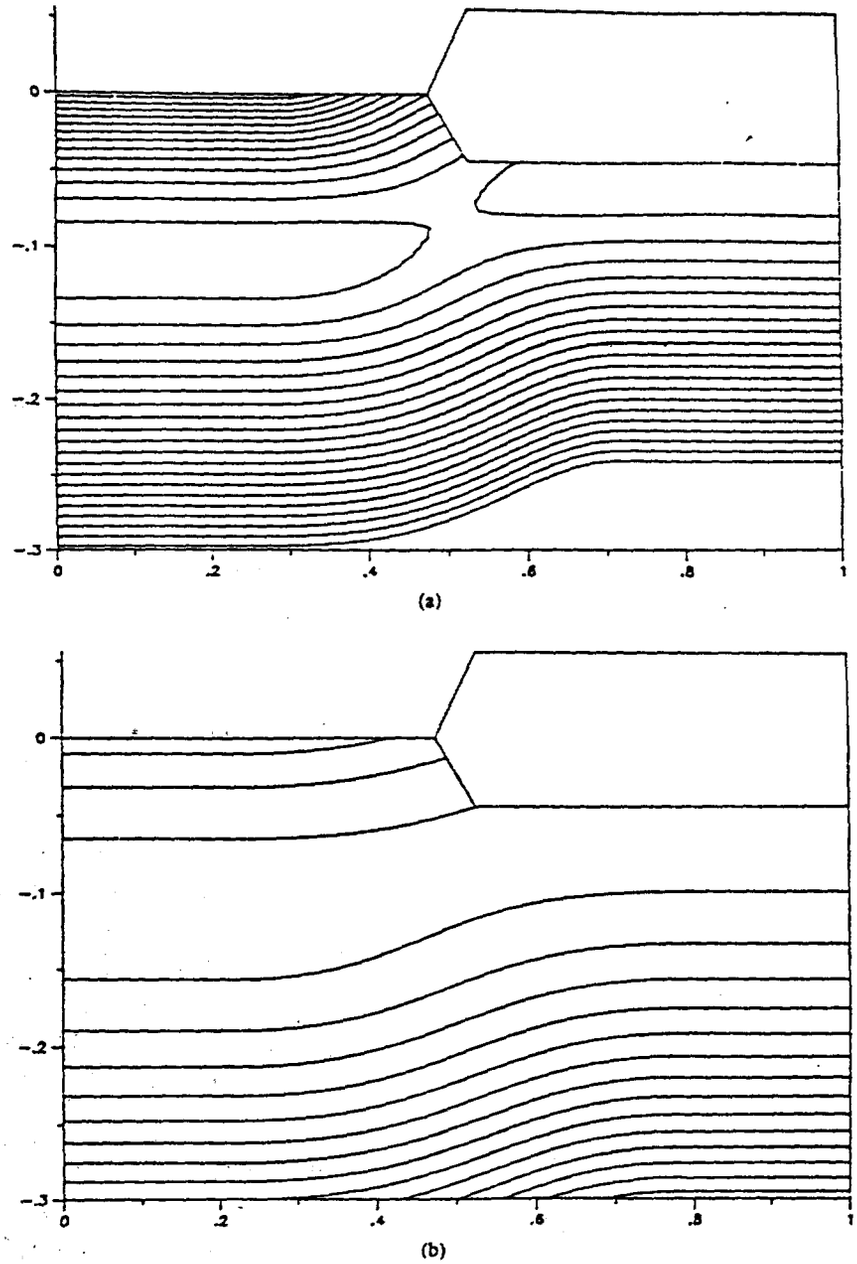


Fig. 3. Contours of log of concentration for boron implanted into silicon near a strongly tapered oxide edge before (a) and after (b) diffusion. The contour ranges are (a) 16.9–18.8 by 0.1 and (b) 17.3–18.6 by 0.1.

## REFERENCES

[1] R. L. Kubena, private communication.
[2] S. Furukawa, H. Matsumura, and H. Ishiwara, "Theoretical considerations on lateral spread of implanted ions," *Japan. J. Appl. Phys.*, vol. 11, pp. 134–142, 1972.
[3] S. K. Ghandhi, *VLSI Fabrication Principles*. New York: Wiley, pp. 345–346, 1983.
[4] J. F. Gibbons, W. S. Johnson, and S. Mylroie, *Projected Range Statistics*, 2nd ed. New York: Wiley, 1975.
[5] W. K. Hofker, D. P. Oosthoek, N. J. Koeman, and H. A. M. De-Grefte, "Concentration profiles of boron implantations in amorphous and polycrystalline silicon," *Radiation Effects*, vol. 24, pp. 223–231, 1975.
[6] H. Ryssel and K. Hoffman, "Ion implantation," in *Process and Device Simulation for MOS-VLSI Circuits*. Boston: Nijhoff, 1983, pp. 124–126.
[7] M. Simard-Normandin, "Empirical modeling of low-energy boron implants in silicon," *J. Electrochem. Soc.*, vol. 132, pp. 2218–2223, 1985.

**Rex E. Lowther** [redacted] He received the B.A. degree from Alfred University in 1974 where he won the Renner Prize in physics. He received the Ph.D. degree in physics from the University of Florida in 1980, where he worked on numerical methods of solving the Schrodinger equation for small systems of atoms.

Upon graduation, he joined Harris Semiconductor where he has been engaged in numerical process and device simulation. From September 1984 to September 1985, as a representative from Harris Semiconductor,

he served as Visiting Engineer to the Department of Computer Science and Electrical Engineering at M.I.T.

Jarvis B. Jacobs [redacted] He received the B.A. degree in physics from Xavier University, New Orleans, LA, and the B.E.E. degree from Georgia Institute of Technology, Atlanta, in 1983. He is currently working toward a Master's degree in electrical engineering at the Massachusetts Institute of Technology.

In 1985, he was awarded a summer fellowship to work at Bell Laboratories. His research interests are in the areas of MOS device modeling and integrated circuits.

Dimitri A. Antoniadis [redacted] He received the B.S. degree in physics from the National University of Athens in 1970, and the Ph.D. degree in electrical engineering in 1976 from Stanford University, CA.

From 1970 to 1978 he was a Research Associate and Instructor in the Department of Electrical Engineering at Stanford University. He joined the faculty at MIT, Cambridge, in 1978 where he is at present an Associate Professor of Electrical Engineering. He is also Director of the new MIT Microsystems Laboratory. From 1969 to 1976, he conducted research in the area of measurements, modeling, and numerical simulation of the earth's ionosphere and thermosphere. He has designed and developed various electronic instruments, currently used for the study of the ionosphere at several locations throughout the world. His present scientific activity lies in the area of semiconductor device and integrated circuit technology. Until 1978, he directed the development of SUPREM (Stanford University Process Engineering Models). His research is currently focused on three areas: fabrication and modeling of ultra-small geometry semiconductor devices; silicon process modeling, with emphasis on the physics of processes and on computer aids for process synthesis; and silicon films on amorphous substrates with ultimate goal-dimensional integrated devices. He is author or coauthor of over 50 technical articles in the above areas.

Dr. Antoniadis is a member of the Electrochemical Society and of the Materials Research Society.